NTNU
Norwegian University of
Science and Technology

Electrical Grid Study of Using Offshore Wind Power for Oil & Gas Offshore Installations

Jonas Frium Opedal

Master of Energy and Environmental Engineering
Submission date: June 2017
Supervisor: Elisabetta Tedeschi, IEL

Norwegian University of Science and Technology
Department of Electric Power Engineering

SUMMARY

The purpose of this thesis is to investigate the performance of a wind integrated oil & gas offshore installation. The motivation behind this is to reduce emissions of CO_2 and other greenhouse gases from offshore installations that utilize natural gas turbines. A model of the wind integrated oil & gas installation is built and implemented in Matlab/Simulink. Figure 1 shows a schematic of the model. The simulations are focused on investigating the performance of the system for transient contingency conditions.

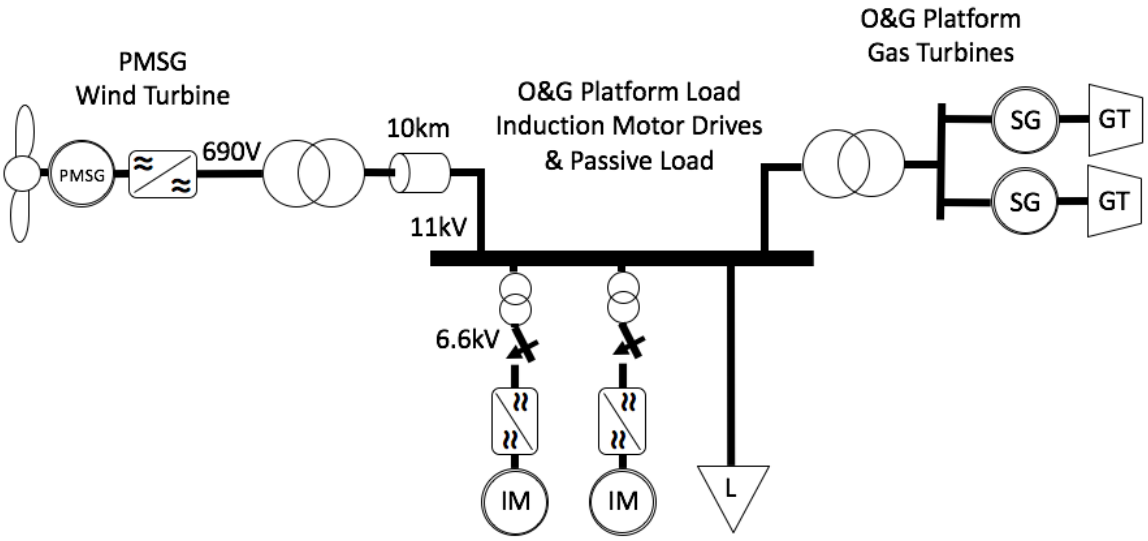

Figure 1. Wind Integrated Oil & Gas Offshore Installation

Two subsystems are investigated separately. The wind energy system is implemented as a $6MW$ direct-driven permanent magnet synchronous generator. The generator connects to the oil & gas installation by a 2-level back-to-back voltage source converter. An extensive control system allows for variable-speed operation to optimize power production. The configuration is found advantageous for use with oil & gas installations as the generator is decoupled from the platform transients by a DC-link. The oil & gas offshore installation is implemented as a $46MVA$ gas turbine synchronous generator, two $8MVA$ induction motor drives and a passive load of $16MW$. The gas turbine is shown to have a fast response in handling transients, and the induction motor drive is shown to have excellent speed and torque control.

The wind integrated oil & gas offshore installation combines the two subsystems through a transmission line. The complete system is simulated for both varying wind speed operation and selected contingency events. The loss of passive load is found to give the biggest voltage transient. The biggest frequency transient is seen for the loss of one of the two gas turbines. All results are compared with the transient limits found in the NORSOK/IEC standards, and found to be within the requirements. The wind turbine is allowed to produce at maximum

throughout the simulations, while the gas turbine is seen to balance the system to maintain the system frequency.

The conclusion of the thesis is that integration of a wind turbine with an oil & gas offshore installation is feasible within the NORSOK/IEC standards. This is true for all scenarios and contingencies tested in this thesis. The results are discussed further in the thesis, with challenges and suggested further work pointed out.

SAMMENDRAG

Formålet med denne masteroppgaven er å undersøke ytelsen til en vindintegrert offshore olje- & gassinstallasjon. Motivasjonen bak dette er å redusere utslipp av CO_2 og andre klimagasser fra kraftproduksjon på gassturbindrevne olje- & gassinstallasjoner. En modell av den vindintegrerte olje- & gassinstallasjonen er bygd og implementert i Matlab/Simulink. Figur 2 viser det komplette systemet. Fokuset i simuleringene er å undersøke systemets ytelse for transiente uforutsette hendelser.

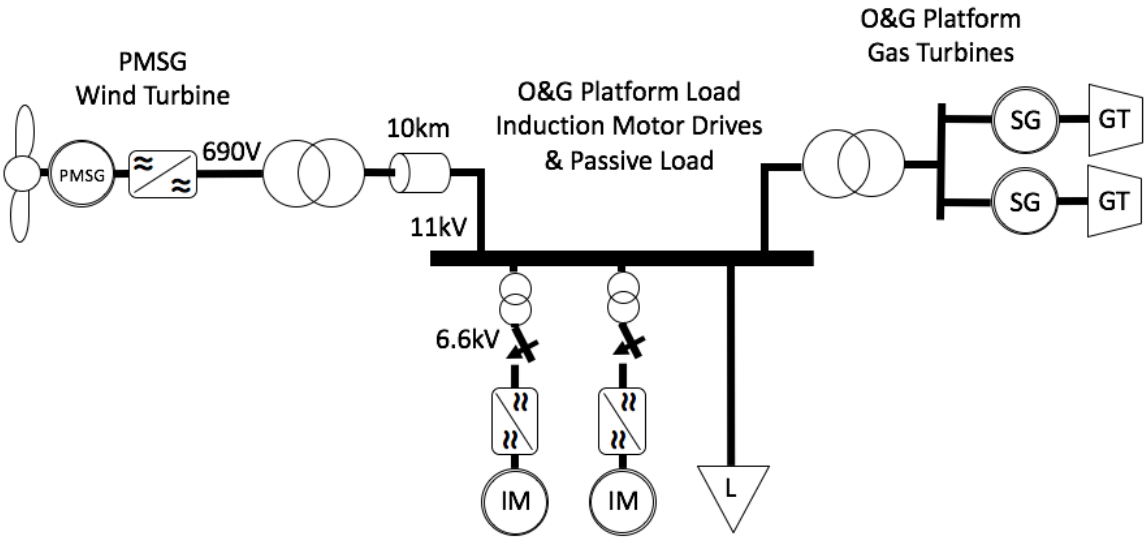

Figure 2. Vindintegrert Offshore Olje- & Gassinstallasjon

To undersystemer er undersøkt separat. Vindenergisystemet er implementert som en $6MW$ direkte-drevet permanentmagnet synkrongenerator. Generatoren er koblet til olje- og gassinstallasjonen gjennom en 2-nivå spenningskildeomformer. Systemet er kontrollert gjennom et omfattende kontrollsystem for turtallsstyring som optimaliserer generatorens kraftproduksjon. Oppsettet er funnet spesielt fordelaktig for bruk ved olje- & gassinstallasjoner ettersom DC-linken isolerer generatoren fra transienter på olje- & gassinstallasjonen. Olje- & gassinstallasjonen er implementert som en $46MVA$ gassturbin-synkrongenerator, to $8MVA$ induksjonsmotorer og en passiv last på $16MW$. Gassturbinen er vist å ha en rask respons i å takle transienter. Induksjonsmotorene har implementert direkte kontroll over fluks og dreiemoment som bidrar til bedre systemytelse.

Den *vindintegrerte* olje- & gassinstallasjonen kombinerer de to undersystemene gjennom en transmisjonslinje. Det komplette systemet er simulert både for varierende vindhastigheter og et utvalg transiente hendelser. Tap av passiv last er funnet å resultere i den største spenningstransienten, mens den største frekvenstransienten er observert for tap av en gassturbin. Alle resultatene er sammenlignet med de transiente grensene gitt i NORSOK/IEC standarden, og funnet å ligge innenfor kravene. Vindturbinen er observert å kunne produsere

maksimalt gjennom hele simuleringen, mens gassturbinen balanserer og opprettholder frekvensen i systemet.

Masteroppgavens konklusjon blir at integreringen av en vindturbin med en offshore olje- & gassinstallasjon er mulig innen de gitte kravene fra NORSOK/IEC. Dette gjelder for alle de testede scenarioene i denne masteroppgaven. Resultatene er diskutert videre gjennom masteroppgaven, og utfordringer og videre arbeid er poengtert underveis.

PROBLEM DESCRIPTION

Statoil is the world leader of offshore oil & gas production, and is also leading within offshore renewable energy technology. Statoil's floating Hywind technology has made a technology breakthrough of utilizing the excellent wind resources at deep water sites. Statoil is initiating a project utilizing offshore wind to supplement the electrical power to Stand-alone Electric Grid at O&G Offshore Installations. The joint NTNU and Statoil project aims at contributing to the electrical grid technology investigation for the first offshore O&G platform powered by Hywind. We are looking for student project candidates to participate in this challenging project.

The overall project goals are to quantitatively identify the grid dynamic performance of an integrated wind powered oil & gas installation under all contingency conditions. More specifically, the tasks are given below.

§ Simulate the microgrid performances under the transient contingency conditions.

§ Analyze the microgrid dynamic performances with regards to NORSOK and IEC related standards.

The project results should include a technical report, simulation programs, and a project presentation in English.

Project Start Date: Jan 23rd 2017

Supervisor: Professor Elisabetta Tedeschi, Department of Electric Power Engineering, NTNU

PREFACE

The master thesis concludes my fifth and final year as a master student with the Department of Electric Power Engineering at NTNU. The thesis documents the work performed for my final spring semester. The work has been found both interesting, comprehensive and challenging, and has prepared me for new challenges in my future work.

The topic of the master thesis has been found very interesting as it combines several of my main fields of interest. This includes both wind power production, motor drive technology and power electronics. I have also appreciated learning more about the oil & gas industry, and to learn more of operation on offshore platforms. I am also grateful for the opportunity provided by Statoil in contributing to the implementation of the world's first integrated oil & gas offshore installation.

I wish to especially thank my supervisor throughout this project, Professor Elisabetta Tedeschi at the Department of Electric Power Engineering at NTNU. She has provided valuable support and help for the work of the thesis. I also wish to thank Post Doctor Santiago Sanchez Acevedo at the Department of Electric Power Engineering at NTNU for assistance with the Matlab/Simulink simulation software, and help on problems encountered while working on the thesis.

Trondheim, 06.06.2017

Jonas Frium Opedal

TABLE OF CONTENTS

LIST OF FIGURES

LIST OF TABLES

ABBREVIATIONS

AC	Alternating Current
DC	Direct Current
DTC	Direct Torque Control
GSC	Generator Side Converter
HVDC	High Voltage Direct Current
IMD	Induction Motor Drive
O&G	Oil & Gas
PMSG	Permanent Magnet Synchronous Generator
SSC	System Side Converter
VSC	Voltage Source Converter
WECS	Wind Energy Conversion System

1. INTRODUCTION

1.1. PROBLEM BACKGROUND AND MOTIVATION

The oil & gas sector is considered Norway's most important industry, and has a huge impact on both GDP and employment. In total, the sector has contributed more than 13,000 billion NOK to the Norwegian GDP, and stands for about 40% of total exports and 20% of the state's annual income [1]. In 2013, the sector employed more than 230,000 people [2]. Recent declines in petroleum prices have also affected employment, lowering this to 185,000, still being a substantial amount.

The last decades have seen an emerging awareness of the damaging effect that CO_2 and other greenhouse gases have on the environment. This has resulted in the emergence of continuously more ambitious climate agreements with the goal of reducing emissions worldwide. The Paris agreement from 2015 is the newest agreement this far [3]. Although taxes on carbon and emissions have existed since the early 1990's, the costs are expected to increase at a much faster rate the coming years. Early adaption to lower emission technology could therefore give an important competitive advantage in the coming years.

The total energy usage on oil & gas offshore installations in Norway accounted for 143TWh in 2015. This is an increase of 62.5% from the year 2000 [4]. The energy is mostly produced locally on the offshore installations, and the production units are mainly natural gas powered gas turbines. These turbines have associated emissions from the burning of fossil fuels. In Norway, these emissions in 2007 accounted for 27% of the total Norwegian emissions [5]. The industry has therefore started to look for alternative ways to power offshore oil & gas installations. Both onshore grid connection and offshore wind power production have been suggested as viable means to achieve this.

Onshore grid connection can be a good alternative for many offshore installations. It is today implemented five places [6]. This is alone estimated to reduce emissions by 1.2 million tons of CO_2 per year, demonstrating the huge potential for emission savings offshore. For installations further from shore, the costs of cables could mean other measures would be preferred. For such platforms, offshore wind power is viewed as most promising. The last years have seen vast improvements in technology for deep-water wind production. Statoil is leading the development with planned implementation of the first deep-water wind park outside Scotland this year [7]. In addition, turbine sizes are getting bigger each year, giving more power and cheaper prices. This all points to offshore wind power being a viable alternative for power production on offshore oil & gas installations. A state of the art for offshore wind technology and studies on the integration of wind power with isolated offshore oil & gas installations can be found in [8].

1.2. METHODOLOGY

The motivation for this thesis is to reduce emissions from offshore oil & gas installations by integrating offshore wind power production. This thesis will seek to investigate the effect this has on the oil & gas installation's electric grid. Specifically, the overall goal of the thesis is to investigate the effects of transient contingency conditions on a wind integrated offshore oil & gas installation.

The work includes a comprehensive description of common components found on oil & gas offshore installation. The focus is on applications for modelling purposes. An extensive model is developed, modelled and simulated within the Matlab/Simulink software. Matlab is used mainly for controlling the variables of the system, while Simulink is used as a framework for complex power system simulations. The different components are divided into subsystems and tested thoroughly to verify the correct working and modelling before implementation in a full wind integrated oil & gas offshore installation. The complete system is simulated and tested for several transient contingency events.

Figure 1.1 shows the complete system modelled for simulation purposes. The two subsystems are as seen in the figure. The PMSG wind energy system is referred to as system 1, while the oil & gas platform microgrid is referred to as system 2. The complete system is denoted system 3, and provides the simulation basis for the main results of this thesis.

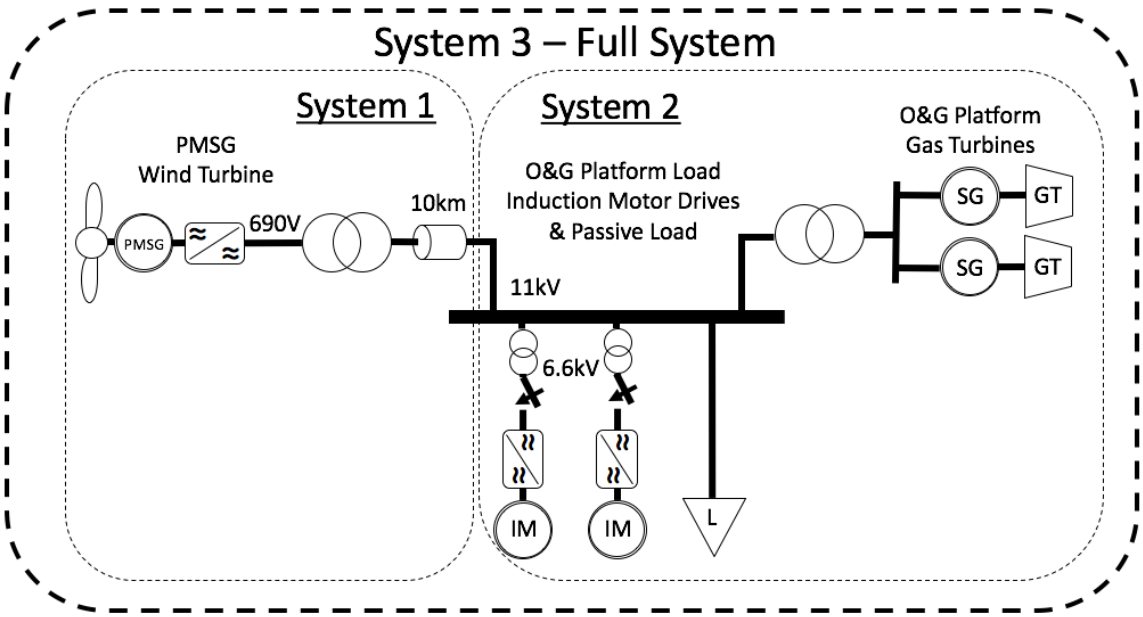

Figure 1.1. Schematic of Wind Integrated Oil & Gas Offshore Installation

1.3. Relation to Specialization Project

The master thesis is the final part of a two-part study investigating the integration of wind power production to oil & gas offshore installations. A specialization project was written in the fall semester of 2016, titled "Feasibility of Wind Power Integration with Oil & Gas Offshore Installations" [8]. The specialization project included a comprehensive state of the art on offshore wind power technology and studies performed on the integration of wind power to offshore oil & gas installations. In addition, a PMSG wind energy system was described and began modelled for simulation purposes.

Some material and figures are similar to the content developed for the specialization project. This includes chapter 2 on the PMSG wind energy system, sections 4.2, 4.3 and 4.5 on the gas turbine, synchronous generator and induction motor, and appendices A and B on PI-controller tuning. It is important to notice that everything is revised and rewritten, and much of the content is greatly improved on.

In relation to the specialization project, the master thesis will focus more on simulations and analysis, as well as validation of correct modelling and building of the different system components.

1.4. Outline of Thesis

The master thesis consists of three main parts; the PMSG wind energy system, the oil & gas offshore installation, and the complete wind integrated oil & gas offshore installation. The parts are referred to as system 1, 2 and 3 respectively. The following explains the outline of the thesis.

Chapter 2 is a description of the PMSG wind energy system with the associated control scheme. The focus is on the equations and relations important in modelling the system. The chapter begins by describing the wind turbine aerodynamics, followed by the PMSG, with special focus on the control system.

Chapter 3 presents the results of the simulations on system 1. The parameters and applied wind profile are presented before the test scenarios are described. This is followed by the simulation results. A discussion summarizes the results with focus on challenges and suggestions for further work.

Chapter 4 is a description of the oil & gas offshore installation. The focus is on a thorough introduction to both production and load units usually found on an oil & gas installation. The chapter describes the gas turbine, the synchronous generator,the induction motor and the direct torque control method.

Chapter 5 presents the results of the simulations on system 2. The parameters and the NORSOK/IEC standard are presented before the test scenarios are described. This is followed

by the simulation results. A discussion summarizes the results with focus on challenges and suggestions for further work.

Chapter 6 presents the results of the simulations on the full integrated system, system 3. The chapter starts with a table summarizing the results of the simulations. This is followed by the theoretic basis and parameters of the transmission line connecting the wind turbine to the platform. The test scenarios are then described, followed by the simulation results. A discussion summarizes the results with focus on challenges and suggestions for further work.

2. SYSTEM 1: PMSG WIND ENERGY SYSTEM

Multiple technologies exist for wind power production today. This thesis is chosen based on the technology used by Statoil for their first deep-water offshore wind power plant [7]. The chosen wind turbine is of type variable speed direct-driven permanent magnet synchronous generator. This chapter will focus on the description of structure, operation and control of the PMSG wind power production system. The focus will be on presenting equations and relations that are relevant for modelling the system. Other important aspects affecting simulation of the components will also be addressed.

Section 2.1 describes the wind turbine aerodynamics and the associated blade pitch control. Section 2.2 describes the permanent magnet synchronous generator. Sections 2.3 and 2.4 describe the voltage source converter technology with basic control principles. Finally, sections 2.5 and 2.6 describe the control of the PMSG wind energy system, separated in generator side control and system side control respectively.

2.1. WIND TURBINE AERODYNAMICS

The wind turbine model used in this thesis is based on the Siemens SWT-6.0-154 [9]. This is in accordance with Statoil's choice of turbine for Hywind Scotland, the world's first deep-water wind park [10]. The turbine is direct driven, and of type permanent magnet synchronous generator (PMSG). It features a 6MW output with a rotor diameter of 154m.

The wind turbine converts wind energy to mechanical energy. As the force of the wind turns the turbine blades a mechanical torque is created in the rotating direction. This can be utilized by an electric generator for electric power production.

The mechanical power output P of the wind turbine varies with the wind speed U as [11]:

$$P = \frac{1}{2}\rho A c_p(\lambda, \beta) U^3 \ (W) \tag{1}$$

where the air density ρ, the turbine swept area A and the turbine's coefficient of performance c_p are constant for a specific wind turbine model.

The Betz limit of c_p = 0.593 sets the theoretical upper limit of power extraction from the wind. The actual value will be lower and vary with turbine type. The coefficient c_p is determined empirically as a relation between the tip speed ratio λ and the pitch angle β as [12]:

$$c_p(\lambda, \beta) = c_1 \left(\frac{c_2}{\lambda_i} - c_3\beta - c_4 \right) e^{-\frac{c_5}{\lambda_i}} + c_6\lambda \tag{2}$$

with λ_i given as:

$$\frac{1}{\lambda_i} = \frac{1}{\lambda + 0.08\beta} - \frac{0.035}{\beta^3 + 1} \tag{3}$$

The coefficients c_1 to c_6 are based on the Matlab/Simulink implemented wind turbine model, but modified by the author to match the rating of the turbine used in this thesis. The resulting values are: c_1 = 0.371, c_2 = 103.6, c_3 = 0.334, c_4 = 5.7, c_5 = 19.81, c_6 = 0.0089. This results in $c_{p,max}$ = 0.3044, for a pitch angle β = 0 and tip speed ratio λ_{opt} = 7.357.

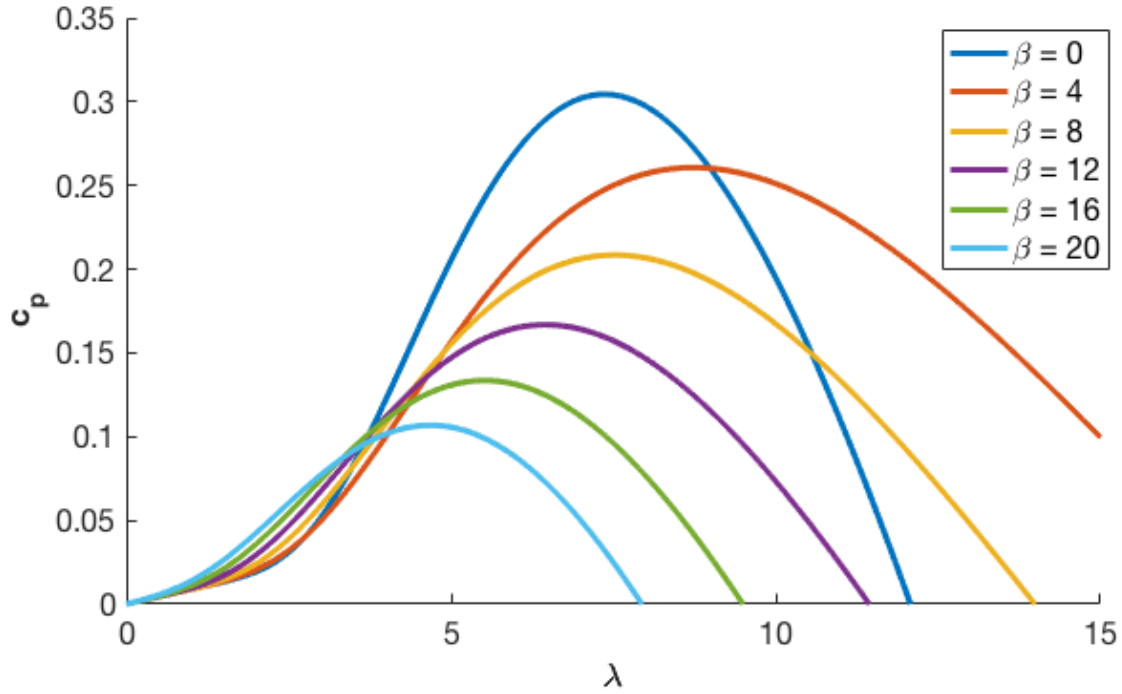

Figure 2.1. Cp vs λ for different values of the pitch angle β

Figure 2.1 plots c_p vs λ for different values of the pitch angle β. Each β corresponds to an optimal λ for maximizing c_p. Thus, keeping an optimal tip speed ratio ensures maximum power extraction for different wind speeds. The tip speed ratio is therefore often used to control the optimal turbine rotational speed.

The mechanical rotational speed ω_m of the wind turbine is given as [11]:

$$\omega_m = \frac{U\lambda}{R} \tag{4}$$

As the wind speed varies, the turbine rotational speed will adjust to maintain the optimal tip speed ratio. The alternative, a change in tip speed ratio away from optimal, gives lower efficiency and is not wanted. This demonstrates the advantage of a variable speed turbine.

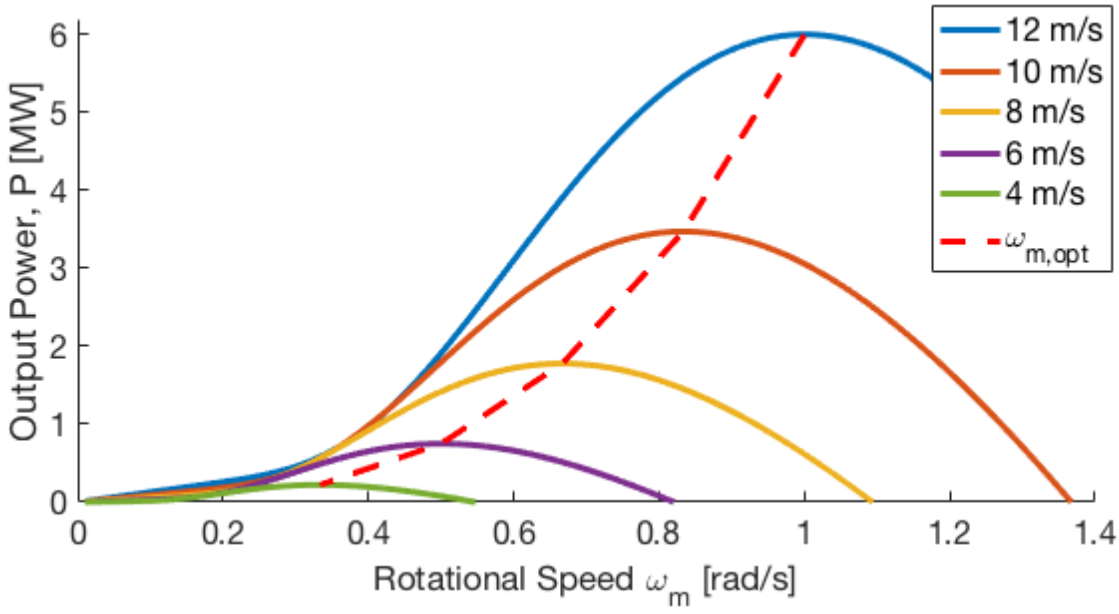

Figure 2.2. Wind Turbine Power Curves

Figure 2.2 shows the power curves of the turbine for a selection of different wind speeds. For each wind speed there is an optimal rotational speed that maximizes the power output by keeping the tip speed ratio optimal. This is discussed more in detail in subsection 2.5.1

2.1.1. Blade Pitch Control

The purpose of the pitch angle controller is to limit the mechanical torque of the wind turbine for wind speeds above rated speed. This is achieved through axial rotation of the turbine blades that reduces the aerial force on the blades. For wind speeds below rated, the pitch angle is set to zero to optimize the power output of the turbine. For higher wind speeds the pitch angle increases, and adjusts to maintain output at rated power.

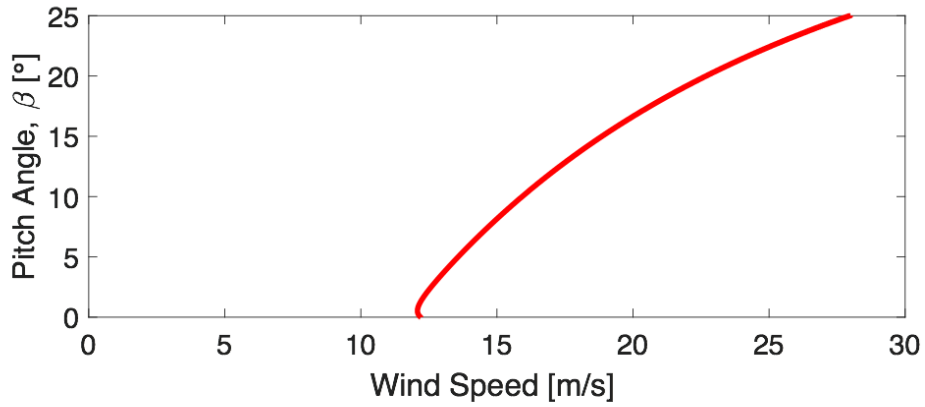

Figure 2.3. Pitch Angle vs Wind Speed for Limiting Power Output of 6MW Turbine

Figure 2.3 gives how the pitch angle relates to the wind speed for the $6MW$ turbine. For wind speeds below rated speed, the pitch angle is zero. When the system exceeds rated speed, the pitch angle gradually rises to atone for the higher power output.

Multiple methods have been suggested by literature for implementing pitch angle control [13, 14]. The strategies mainly revolve around the use of one of three input variables to properly determine the pitch angle. These are the wind speed, the generator rotor speed or the generator output power. This thesis will utilize generator power as controller input and implement a PI-controller based system. Figure 2.4 gives the block diagram of the proposed pitch angle controller.

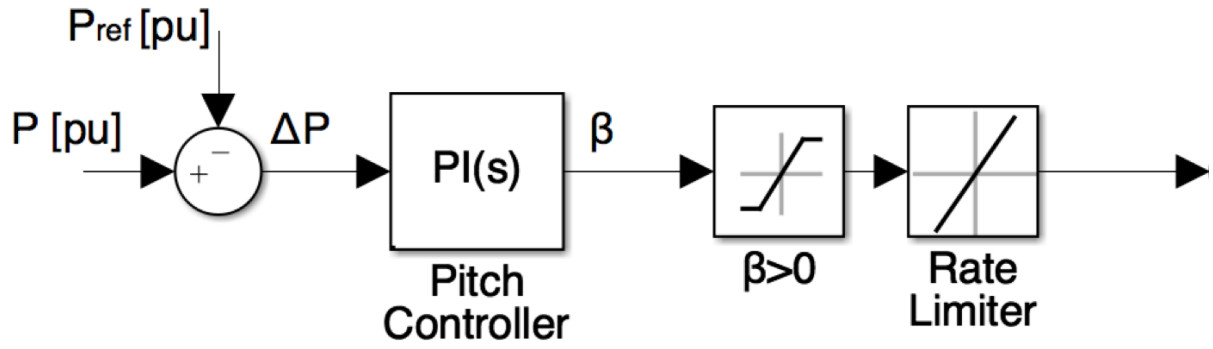

Figure 2.4. Block Diagram of Pitch Angle Controller

The controller compares the per unit generator power output *P* with a reference power of 1pu. The error signal is sent through a PI-controller resulting in the optimal pitch angle β. The saturator is included to ensure the pitch angle is always zero or larger. This also prevents the pitch controller from being active for power outputs below rated power as that would give a negative signal. A rate limiter is included to reflect the physical limitation of how fast the blades can rotate. The limit is set to $\pm 4°$ per second in this thesis.

The aerodynamic properties of the wind have nonlinear components as seen in equations (2) and (3). This makes a linear system as the PI-controller not the optimal choice. Another option would be to include gain scheduling and switching as seen from [15], or implement a fuzzy logic scheme as proposed by [14]. The PI-controller scheme is however found simpler, and adequate for the simulations of this thesis.

2.2. PERMANENT MAGNET SYNCHRONOUS GENERATOR

The permanent magnet synchronous generator (PMSG) is described as a three-phase sinusoidal electrical system in the dq rotor reference frame by the following equations [16, 17]:

$$\frac{d}{dt}i_d = \frac{1}{L_d}v_d - \frac{R}{L_d}i_d + \frac{L_q}{L_d}\omega_e i_q \tag{5}$$

$$\frac{d}{dt}i_q = \frac{1}{L_q}v_q - \frac{R}{L_q}i_q - \frac{L_d}{L_q}\omega_e i_d - \frac{\lambda_f \omega_e}{L_q} \tag{6}$$

where R refers to the stator windings resistance, L_d and L_q to the stator d and q axis inductances, and i_d, i_q, v_d and v_q to the d and q axis currents and voltages. The λ_f is the flux linkage induced in the stator windings by the permanent magnets of the rotor, and ω_e is the electrical rotational speed of the machine. The electrical speed is synchronized with the *abc* three-phase system by a phase-locked-loop (PLL). The mechanical speed ω_m is related to the electrical speed through $\omega_e = \omega_m n_p$, with n_p being the number of pole pairs in the machine.

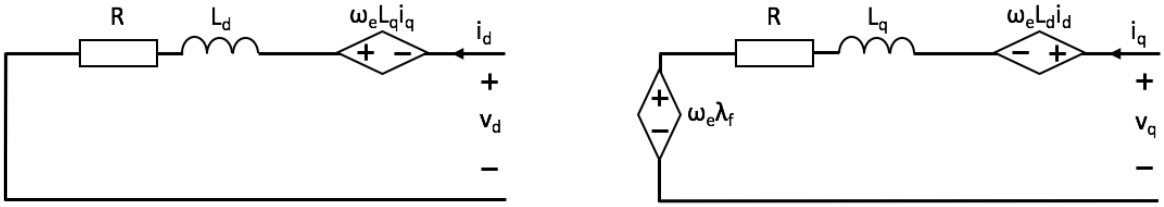

Figure 2.5. PMSG Equivalent Circuit in the dq-frame

Figure 2.5 shows the equivalent circuit for the permanent magnet synchronous generator in the dq-frame.

The electromagnetic torque T_e of the permanent magnet synchronous machine can be expressed by the same parameters as:

$$T_e = 1.5 n_p \left[\lambda_f i_q + \left(L_d - L_q\right) i_d i_q\right] \tag{7}$$

The current i_d is often set to zero to minimize the total currents and resistive losses. Also, for a non-salient machine the inductances $L_d = L_q$, which reduces equation (7) to:

$$T_e = 1.5 n_p \lambda_f i_q \tag{8}$$

Equation (8) demonstrates how only i_q is needed to control the electromagnetic torque of the machine.

The current state of equations (5) and (6) includes cross-coupling terms corresponding to control scheme disturbances. As the control strategy utilizes two degrees of freedom, it requires independent control of the two currents. The disturbances are therefore secluded to

separate feed-forward terms, $v_{dq,ff}$. The modified equations become $v_{dq} = v'_{dq} + v_{dq,ff}$, with $v_{q,ff} = \omega_e L_d i_d + \omega_e \lambda_f$ and $v_{d,ff} = -\omega_e L_q i_q$, and the independently controllable v_{dq}' becomes:

$$\frac{d}{dt} i_d = \frac{1}{L_d} v_d{}' - \frac{R}{L_d} i_d \tag{9}$$

$$\frac{d}{dt} i_q = \frac{1}{L_q} v_q{}' - \frac{R}{L_q} i_q \tag{10}$$

The mechanical drive train can be included to combine the mechanical and electrical parts of the machine. The following equation describes the acceleration $\frac{d\omega_m}{dt}$ as the difference between the electromagnetic torque T_e and the load torque T_m acting on the combined inertia J as:

$$\frac{d\omega_m}{dt} = \frac{T_e - T_m}{J} \tag{11}$$

2.3. VOLTAGE SOURCE CONVERTERS (VSC)

Figure 2.6 gives the single line diagram of a two-level voltage source converter (VSC). The converter has six power switches of type IGBT/diode connected in a bridge configuration.

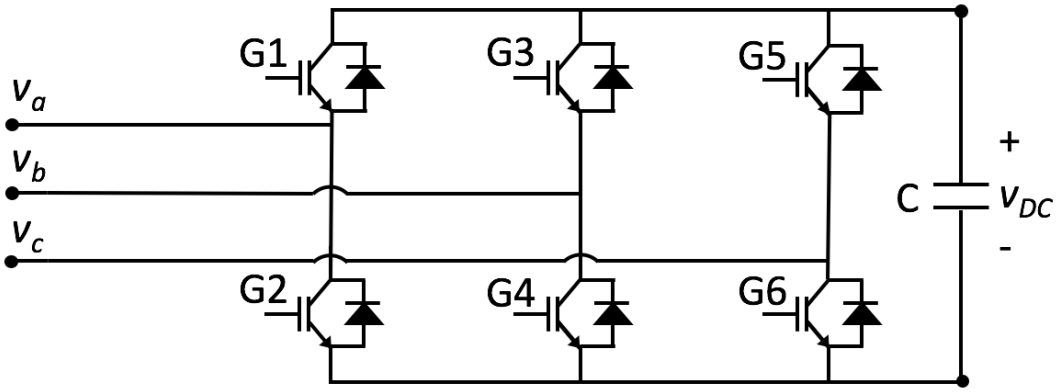

Figure 2.6. Single Line Diagram of Two-Level Voltage Source Converter

The voltages v_{abc} represent the different phases of the AC voltage, while v_{DC} represents the DC-voltage applied to the bridge converter. *G1* to *G6* represent the controllable IGBT/diode switches and *C* represents the capacitor that smooths the DC-voltage.

The principle behind the two-level converter lies in continuously switching the AC-voltage output between two discrete levels [18, 19]. The levels correspond to the semiconductor's saturated region and its cut-off region, meaning either an "on" or "off" position. Operation in

the active region is unwanted as it would lead to high power losses with both voltage and current across the device. The corresponding voltages will be either the positive or the negative potential of the DC-terminal, giving v_{DC} or zero as the voltage output. The switches G1, G3 or G5 in position "on" gives the output $+v_{DC}$ while the switches G2, G4 or G6 in position "on" gives 0. The resulting voltage output will be a square wave alternating between v_{DC} and 0.

The square waveform will lead to unacceptable levels of harmonic distortions, making a sinusoidal wave preferred. By having a switching frequency much higher than the AC frequency, a sinusoidal waveform can be approximated. Applying pulse width modulation will even further improve this. For a detailed account on pulse width modulation, see [8, 18].

2.4. Control Principles of Voltage Source Converters

The PMSG control scheme is based on vector control principles implemented in the dq-reference frame. Figure 2.7 shows the complete PMSG system. The control system consists of two independently controlled voltage source converters denoted generator side converter (GSC) and system side converter (SSC). The description of the specific converters is found in sections 2.5 and 2.6. The following will be a general description of control of voltage source converters.

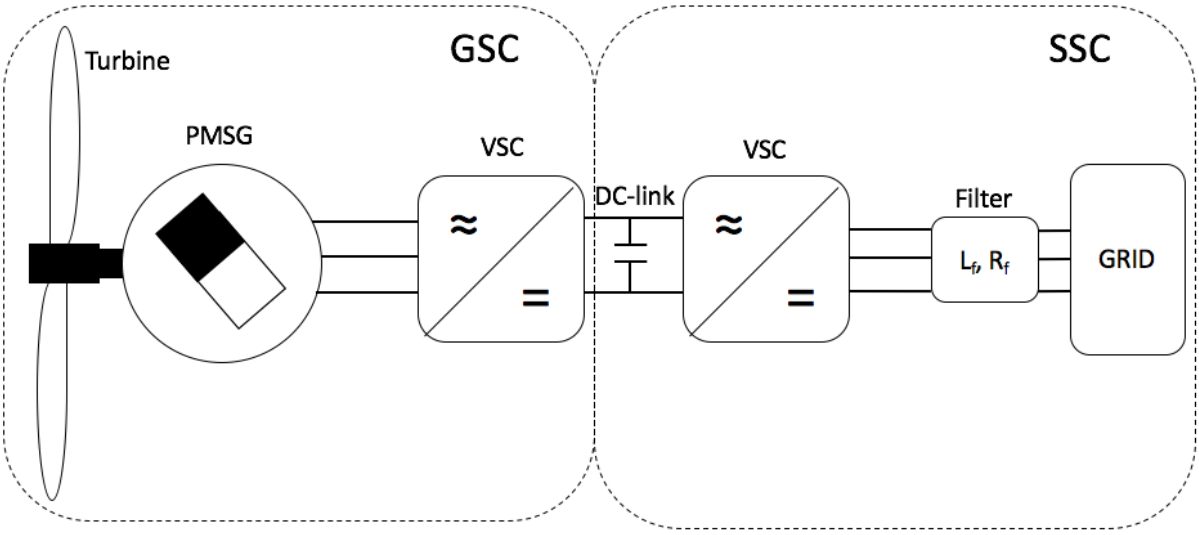

Figure 2.7. PMSG Wind Energy System

The operating characteristics of the voltage source converter are determined by the associated control system. For a two-level converter the system operates with two degrees of freedom that controls two independent variables, usually the active and reactive power. This section serves as a framework for control systems later in the thesis.

The control scheme will be based on vector control principles in the dq-reference frame [20]. The dq-reference frame is explained in more detail in [21]. The PWM control signal is aiming at regulating the AC-voltage to maintain power balance between the DC and AC-side. The balanced voltage equations for the VSC are given as [22]:

$$L\frac{di_d}{dt} = -R_f i_d + \omega L_f i_q - V_{d,conv} + V_d \tag{12}$$

$$L\frac{di_q}{dt} = -R_f i_q - \omega L_f i_d - V_{q,conv} + V_q \tag{13}$$

where V_{dq}, i_{dq}, and $V_{dq,conv}$ are the voltages, currents and converter input voltages in the dq-reference frame, R is the filter resistance, and L the filter inductance. The filter is placed on the AC-side of the converter. The equations in this form contain cross-coupling terms that are usually separated from the equations to obtain a simple first order system. The terms are used as a feed forward to the system to improve on disturbances, here given as:

$$V_{d,ff} = V_d - \omega L_f i_q \tag{14}$$

$$V_{q,ff} = V_q + \omega L_f i_d \tag{15}$$

The power balance of the converter is given as:

$$P = \frac{3}{2}\left(v_d i_d + v_q i_q\right) = V_{DC} I_{DC} \tag{16}$$

where V_{DC} is the DC voltage, and i_{DC} is the DC current. The d-axis is chosen to be aligned to the a-axis vector, which gives $v_q = 0$. The active and reactive power are therefore reduced to:

$$P = \frac{3}{2} v_d i_d \tag{17}$$

$$Q = \frac{3}{2} v_d i_q \tag{18}$$

The control of the VSC is therefore limited to controlling the currents i_{dq}. The optimal values of the currents are determined based on the objective of maintaining a constant DC-voltage and limit the reactive power. The controlled currents are later transformed to voltage signals that are utilized by the pulse width modulation to provide the switching signals to the converter. The control system is largely based on PI-controllers, and require appropriate tuning to function properly. This is given in appendix A.

2.5. CONTROL OF GENERATOR SIDE CONVERTER

Figure 2.8 demonstrates the block diagram for the control of the converter on the generator side of the PMSG system. The strategy involves controlling the dq-currents of the machine to control the electric torque and the power output.

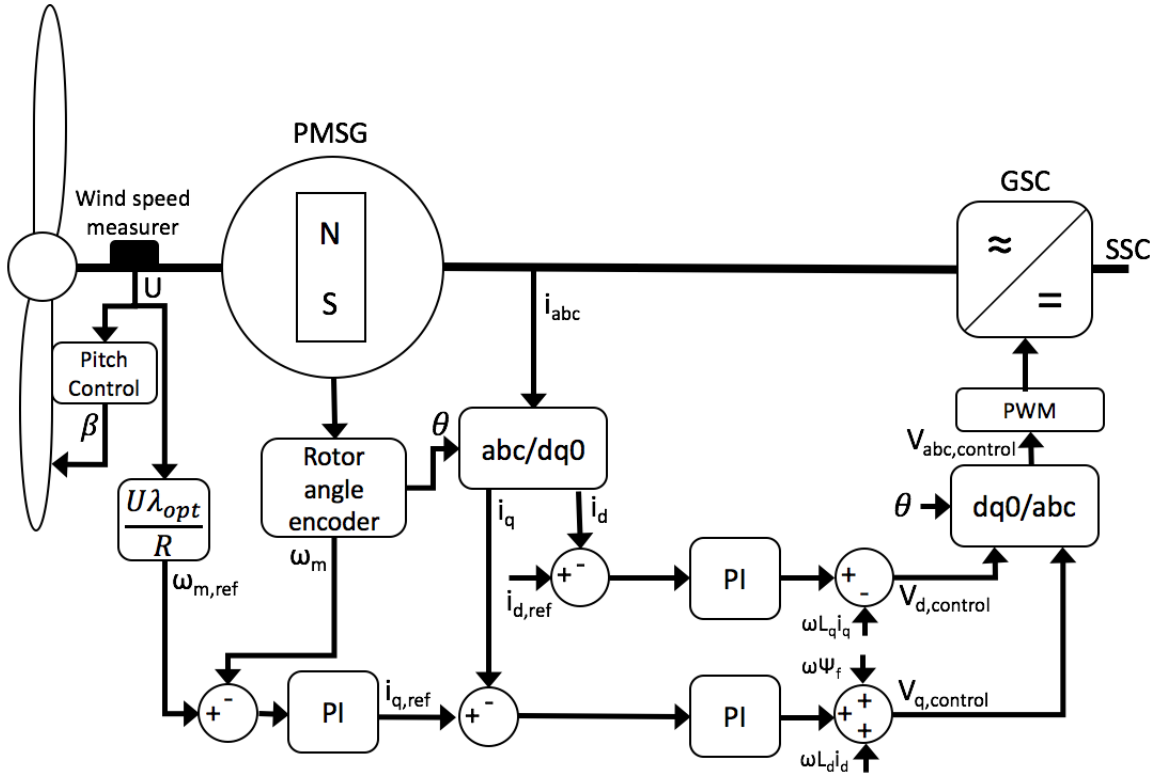

Figure 2.8. Block Diagram of PMSG Generator Side Converter

2.5.1. SPEED CONTROL

The speed controller is part of the outer control loop of the generator side converter (GSC). Its purpose is to regulate the mechanical speed of the rotor by comparing it to a reference speed. The error is then processed and fed to an inner current control loop. Implemented correctly, the controller will assure the optimal rotor speed and optimize power output for all wind speeds. The described method, also utilized in this master thesis, is based on PI vector control [17, 23]. Other approaches found in literature include direct torque control and maximum power point tracking (MPPT) [24, 25].

Equation (1) in chapter 2.1 gave the power equation for wind power. At any specific wind speed, the parameter *U* can be considered a constant. The maximum power P_{max} then becomes:

$$P_{max} = k * c_{p,opt}(\lambda_{opt}, \beta) \qquad \left(k = \frac{1}{2}\rho A U^3\right) \qquad (19)$$

where ρ is the air density, A is the turbine swept area, λ_{opt} is the optimal tip speed ratio, β is the the pitch angle, and $c_{p,opt}$ is the optimal turbine coefficient of performance. Maximum power output is seen to only be dependent on c_p, and require its optimal value.

Equations (2) and (3) give that, for each value of pitch angle β, there exists an optimal tip speed ratio λ_{opt} that maximizes c_p. Figure 2.1 demonstrates this. The control objective therefore results in optimizing the tip speed ratio.

By rewriting equation (4), an expression for the tip speed ratio as a function of mechanical speed can be achieved:

$$\lambda(\omega_m) = \frac{R}{U}\omega_m \tag{20}$$

Keeping the wind speed and radius constant, the tip speed ratio only varies with the mechanical speed, giving the optimal rotational speed as:

$$\omega_{m,opt} = \frac{U\lambda_{opt}}{R} = \omega_{m,ref} \tag{21}$$

This is used as reference speed for the outer control loop. Figure 2.9 shows the complete block diagram of the speed controller.

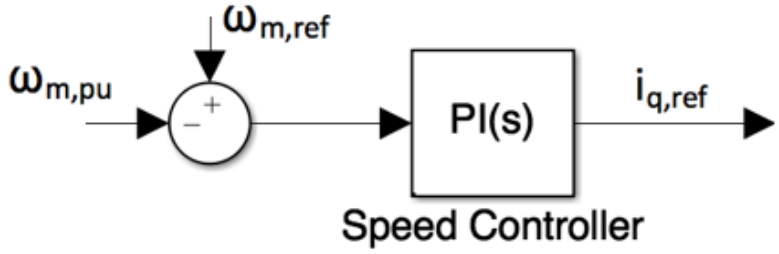

Figure 2.9. Block Diagram of Speed Controller

The reference speed is compared to the actual rotational speed in per unit. The error signal is processed by a PI controller. The output of the controller is the reference current $i_{q,ref}$, which is used as a control variable for the inner current control loop. To reduce currents and minimize resistive losses, the other reference current, $i_{d,ref}$, is set to zero.

2.5.2. Inner Current Control

The machine currents along with the rotor angle θ are measured, and the currents are transformed to the dq-reference frame synchronized by the rotor angle. The error of the current signals is sent through PI-controllers where the feed forward disturbance terms $v_{dq,ff}$

are added. This gives the control signals $v_{dq,control}$. The signals are then transformed back to the abc-frame and fed to a pulse-width modulator (PWM). The PWM switching signals are used to control the switching ports of the voltage source converter (VSC) and thereby control the torque and speed of the generator.

Equation (8) shows how the currents directly control the machine's electrical torque and machine speed ($n_p = {\omega_e}/{\omega_m}$). For example, a decrease in electrical torque will result in the machine decelerating, while an increasing electrical torque accelerates the machine.

2.6. CONTROL OF SYSTEM SIDE CONVERTER

Figure 2.10 demonstrates the block diagram of the system side converter (SSC) control system. The SSC is connected to the generator side converter through a DC-link in a back-to-back configuration. A capacitor is included to smooth and limit voltage transients. The control strategy is based on using the currents on the system side to independently control the DC-link voltage and the reactive power.

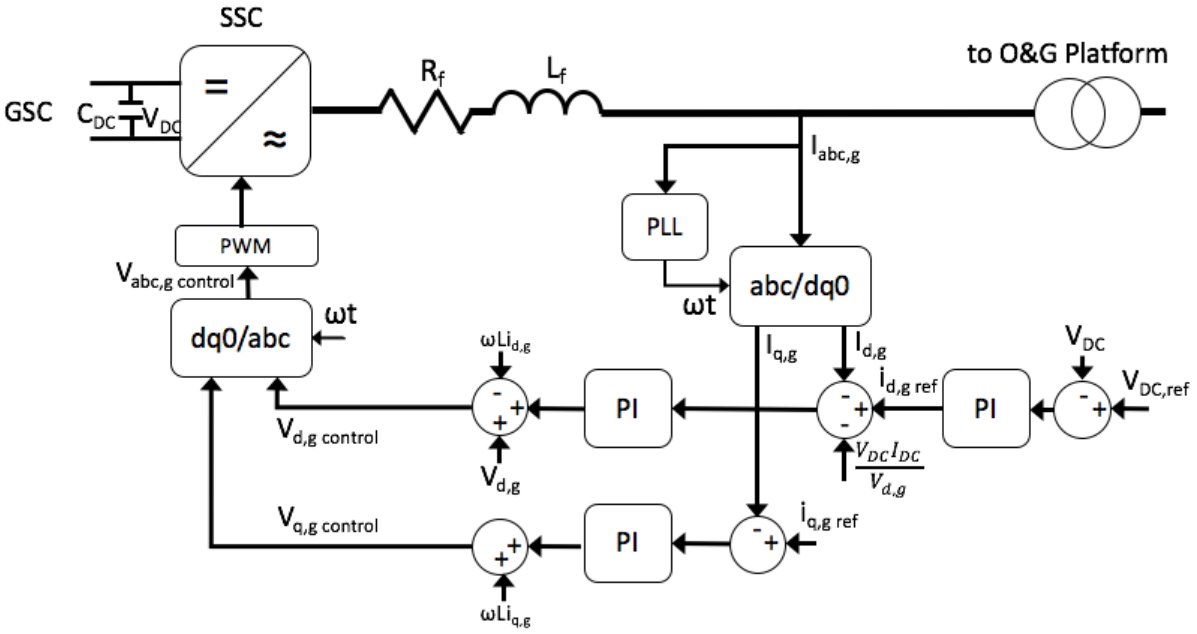

Figure 2.10. Block Diagram of PMSG System Side Converter

The outer control loop consists of a DC-voltage controller and a reactive power controller. The DC-voltage controller measures the voltage across the capacitor and compares it to a reference of 1pu. The resulting error is processed by a PI controller to produce the $i_{dg,ref}$ signal for the inner control loop. The other reference current, $i_{qg,ref}$, gives reactive power control of

the system. As no reactive power production is wanted in this thesis, the reference is set to zero. This gives $i_{qg,ref}$ also equal to zero.

The three-phase currents on the system side are measured and transformed to the dq-reference frame. A phase-locked-loop (PLL) provides the synchronizing angle to uphold synchronization with the grid. A feed-forward term, $\frac{V_{DC,pu}I_{DC,pu}}{V_{dg,pu}}$, is added to the *d*-current signal to improve the response time of the system. This reduces both the load variations and the required gain of the PI-controller. The current signals are then compared to the references provided by the outer loop, and fed to the PI-controllers. The output is added to feed-forward disturbance terms similar to on the generator side, and the resulting $v_{dq,control}$ signals are transformed back to the abc-frame and fed to a pulse-width modulator (PWM). This produces the switching pulses used by the converter to uphold control of the DC-voltage and the reactive power.

3. System 1: Simulations on PMSG Wind Energy System

The following chapter will focus on simulations of the PMSG wind energy system, referred to as system 1. The goal of the chapter is to verify the correct modeling and functioning of the system. This provides a basis for use in further simulations of the bigger wind integrated oil & gas platform system given in chapter 6. Figure 3.1 shows a simple schematic of the simulated system.

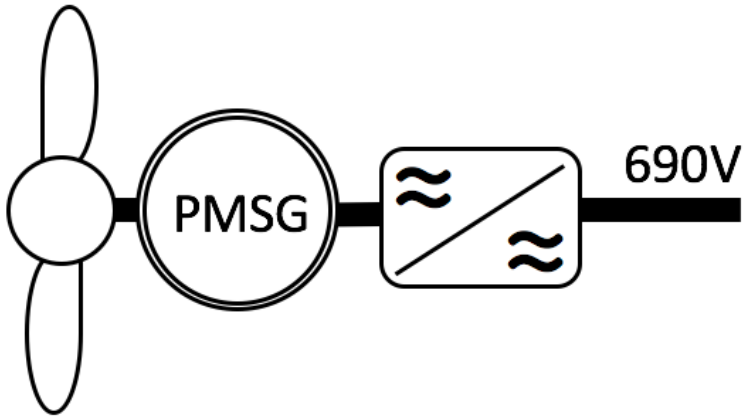

Figure 3.1. PMSG Wind Energy System

The chapter is organized in six subsections. Section 3.1 presents the chosen wind profile of this thesis. Section 3.2 gives the numerical parameters used for the simulations. Section 3.3 describes the modelling in Matlab/Simulink, the simulation software of the thesis. Two test cases are chosen for simulation. In section 3.4, the system is verified at normal operation for the applied wind speed profile of the thesis. In section 3.5, the system is verified for operation within the offshore wind generation grid code limits on voltage and frequency. Section 3.6 discusses the results of the simulations.

3.1. Wind Speed Profile

The wind speed profile applied for the system simulations is based on measured wind data provided by Statoil at wind turbine height [26]. The profile has a duration of 50 seconds and is chosen to demonstrate the system's behavior at different wind speeds. The different periods of the wind profile are discussed in more detail below. Figure 3.2 shows the complete wind profile.

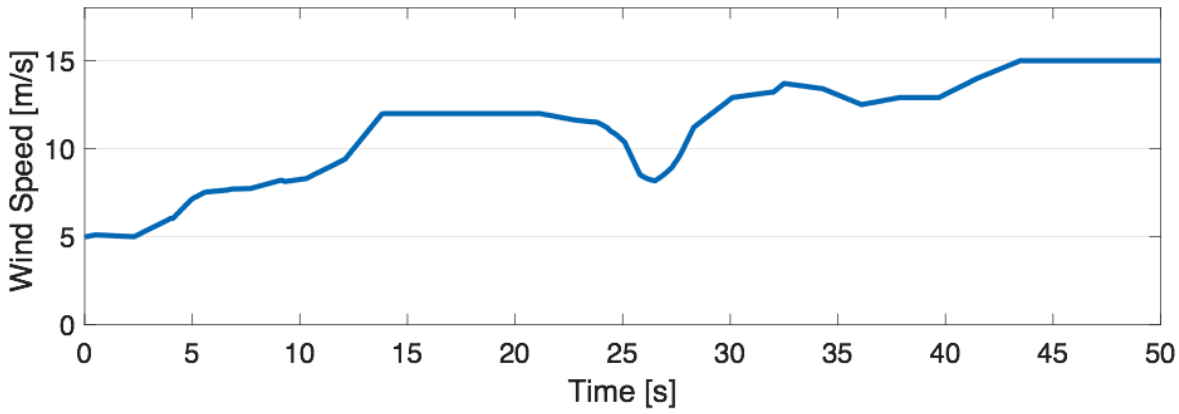

Figure 3.2. Wind Speed Profile for simulations

The simulation starts at $t = 0$, at wind speed $5m/s$ which is the cut-in speed of the turbine. For lower wind speeds, the turbine is kept inactive.

From $0 < t < 14$ seconds, the turbine operates at wind speeds below the rated speed of $12m/s$. This is considered normal operation conditions that all wind turbines should handle. At these speeds, the control system should continuously adjust the system currents to achieve optimal power output.

From $14 < t < 22$ seconds, the turbine operates at rated speed. Although operation at steady rated speed would be unusual, it is included as it allows for testing of the tuning of the system parameters. At rated speed, all parameters should be at their rated values. This also allows for testing at steady state conditions to differentiate the effect varying wind speeds have on operation.

From $22 < t < 29$ seconds, the turbine operates at what is known as a gust. A gust is a short rise or fall in the wind of relatively large magnitude compared to the wind speed average [27]. Gusts often appear as continuous events during longer duration turbulence.

From $29 < t < 50$ seconds, the turbine operates at wind speeds above rated speed. This allows for testing the system's ability to maintain rated power output at continuous operation. At this point the blade pitch controller should work to limit the power output.

3.2. Numerical Parameters

The parameters of the system are given in Table 3.1, Table 3.2 and Table 3.3. The values are set according to available information on existing Hywind projects, selected sources and based on derivations from the system model.

Table 3.1 gives the parameters of the wind turbine. The values are based on the Hywind Scotland Project, using the turbine Siemens SWT-6.0-154 [9][1]. The inertia is taken from [28][2], and the mechanical speed is calculated based on the system base values[3]. The base values are the rated power and voltage of the PMSG.

Table 3.1. Parameters of Wind Turbine

Parameter	*Value*
Rated wind speed *(U)*[1]	12m/s
Rotor radius *(r)*[1]	77m
Air Density *(ρ)*	1.025kg/m^3
Rated mechanical speed *(ω_m)*[3]	1.15rad/s
Inertia *(J)*[2]	534116kg.m^2

Table 3.2 gives the parameters of the PMSG. The values are based on the Siemens SWT-6.0-154 [9][1] and taken from [29][2]. Some are also calculated based on the system base values[3]. The base values are the rated power and voltage of the PMSG.

Table 3.2. Parameters of PMSG

Parameter	*Value*
Rated Power *(P)*[1]	6MW
Rated Voltage *(V)*[1]	690V
AC frequency *(f)*[1]	50Hz
Stator resistance *(R_s)*[2]	0.1pu
Stator axis inductance *(L_d)*[2]	0.8pu
Stator axis inductance *(L_q)*[2]	0.7pu
Permanent magnet flux *(ψ_f)*[2]	1.4pu
Pole pairs *(np)*[3]	274

Table 3.3 gives the parameters of the VSC. The values are found in [30], and directly implemented. The base values are the rated power and voltage of the PMSG.

Table 3.3. Parameters of VSC

Parameter	*Value*
DC-link Capacitor *(C_{DC})*	0.88pu
Grid-side Filter *(L_F)*	0.15pu
Grid-side Filter *(R_F)*	0.01pu
Switching Frequency *(f_{sw})*	10kHz

3.3. Model Implementation in Simulink

The PMSG wind energy system is modelled and implemented in Matlab/Simulink. The wind turbine model is implemented by the author in the per unit system based on the equations of section 2.1. The permanent magnet synchronous machine is implemented as a built-in block in Simscape Power Systems. This is based on the equations given in section 2.2. The back-to-back voltage source converters, with the associated control system, are implemented based on the schemes of sections 2.5 - 2.6. The system is connected to a three-phase voltage source working as a stiff grid.

The two power converters are the built-in two-level converter blocks. They are modeled as switching devices with IGBT/diode pairs, providing higher accuracy than the average model. They do however yield a slower simulation time. The complete Matlab/Simulink model is shown in appendix C.

3.4. System Response of Wind Profile

The wind speed profile of section 3.1 is applied to the PMSG wind energy system modelled in Matlab/Simulink. The numerical parameters of the system are found in section 3.2.

Figure 3.3 shows the wind system's response to varying wind speed operation. The rotor mechanical speed and its reference is given in b). The rotational speed follows the reference with high accuracy. The fast response of the speed controller demonstrates the ability of the wind turbine to handle rapid variations in wind speed. The reference speed is seen to follow the shape of the wind speed in a), and to be limited to $1pu$ for the period where wind speeds are above rated speed. Some overshoots are observed, caused by the limitation in the change

rate of the pitch angle controller. If the wind speed changes faster than the pitch angle, overshoots such as the observed would be seen.

The active power output of the PMSG is shown in per unit for both generator and system side in c). The power is seen to closely follow the rotor speed in b). Above rated speed, the power is limited to $1pu$. The observed overshoots are caused by the wind speed increasing faster than the allowed change rate of the pitch angle controller. The machine inertia causes power fluctuations of $\pm 8\%$, for rapid speed changes. The system is seen to stabilize as the speed stabilizes. The higher fluctuations observed in the SSC power are due to the switching devices in the model. A lower sampling time would reduce the fluctuations, but also increase the simulation time. The reactive power output of the system is observed to follow the reference value of zero. The fluctuations lie around $\pm 15\%$. This can be observed in d).

The DC-link voltage is given in e). The control goal is to maintain a DC-voltage of 1pu. This is seen accomplished. The ripple is small, in the area of $\pm$2%. The rms voltage is kept steady at $690V$, while the current is changing to optimize the power output as seen in f).

Figure 3.3 g) gives the pitch angle and tip speed ratio of the turbine. Both are kept steady at their optimal values for wind speeds below rated speed. For higher wind speeds, the pitch angle is seen to increase with the wind speed. The pitch angle is seen to increase at maximum rate multiple periods. This happens if the wind speed changes faster than the allowed pitch angle change rate. For these periods, overshoots and undershoots in active power is observed as the pitch angle catches up. Similarly, the tip speed ratio is adjusting inverse to the wind speed to limit the speed controller output.

The dq-currents are given in h) and i) for generator and machine side respectively. The currents are used to control the power converters and are seen to follow their references correctly.

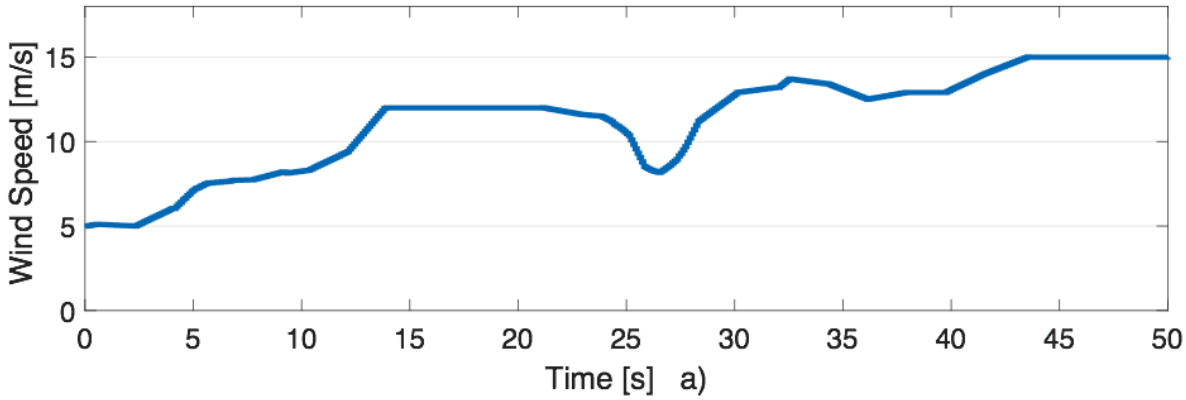
Wind Speed [m/s]
Time [s] a)

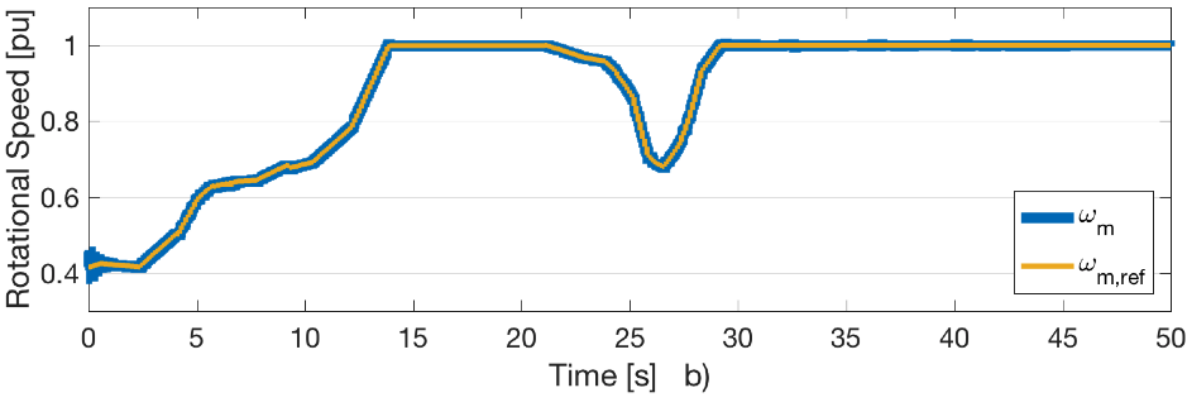
Rotational Speed [pu]
ω_m
$\omega_{m,ref}$
Time [s] b)

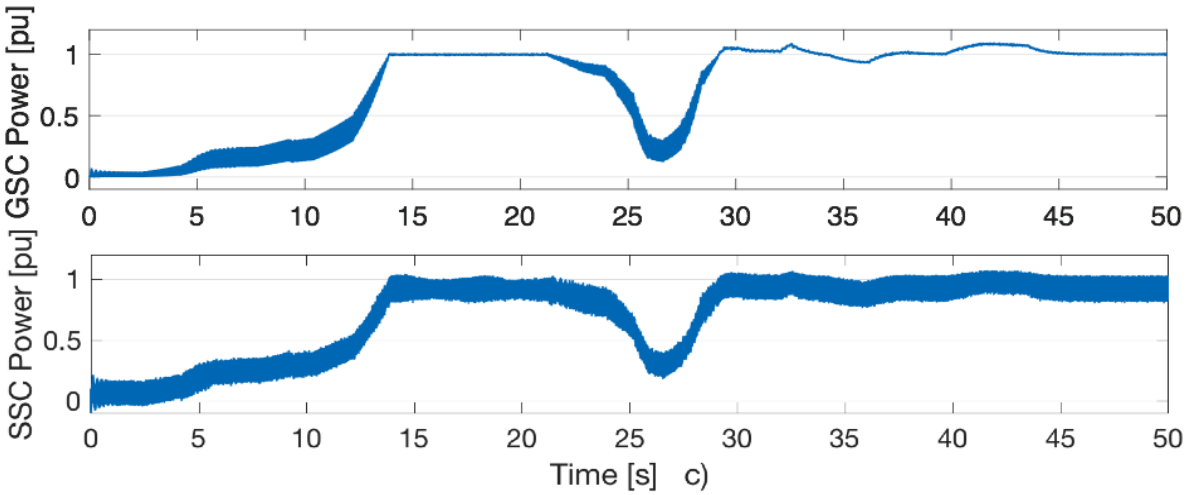
GSC Power [pu]
SSC Power [pu]
Time [s] c)

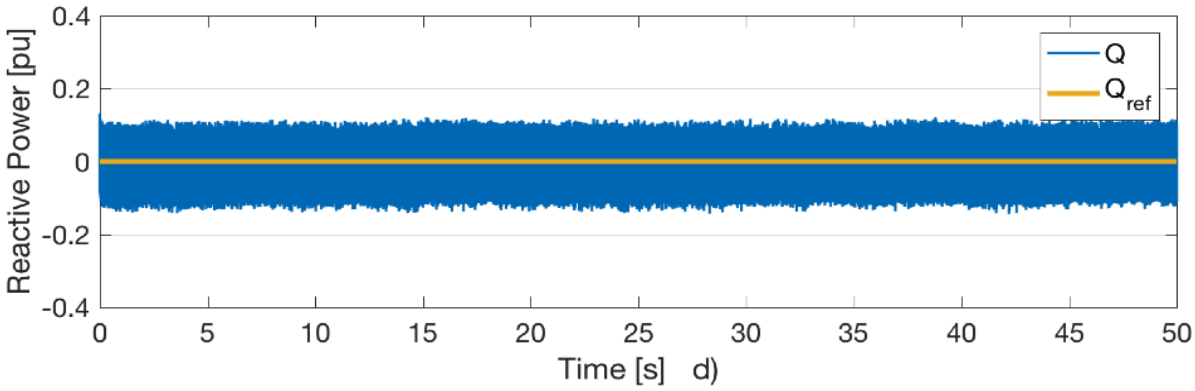
Reactive Power [pu]
Q
Q_{ref}
Time [s] d)

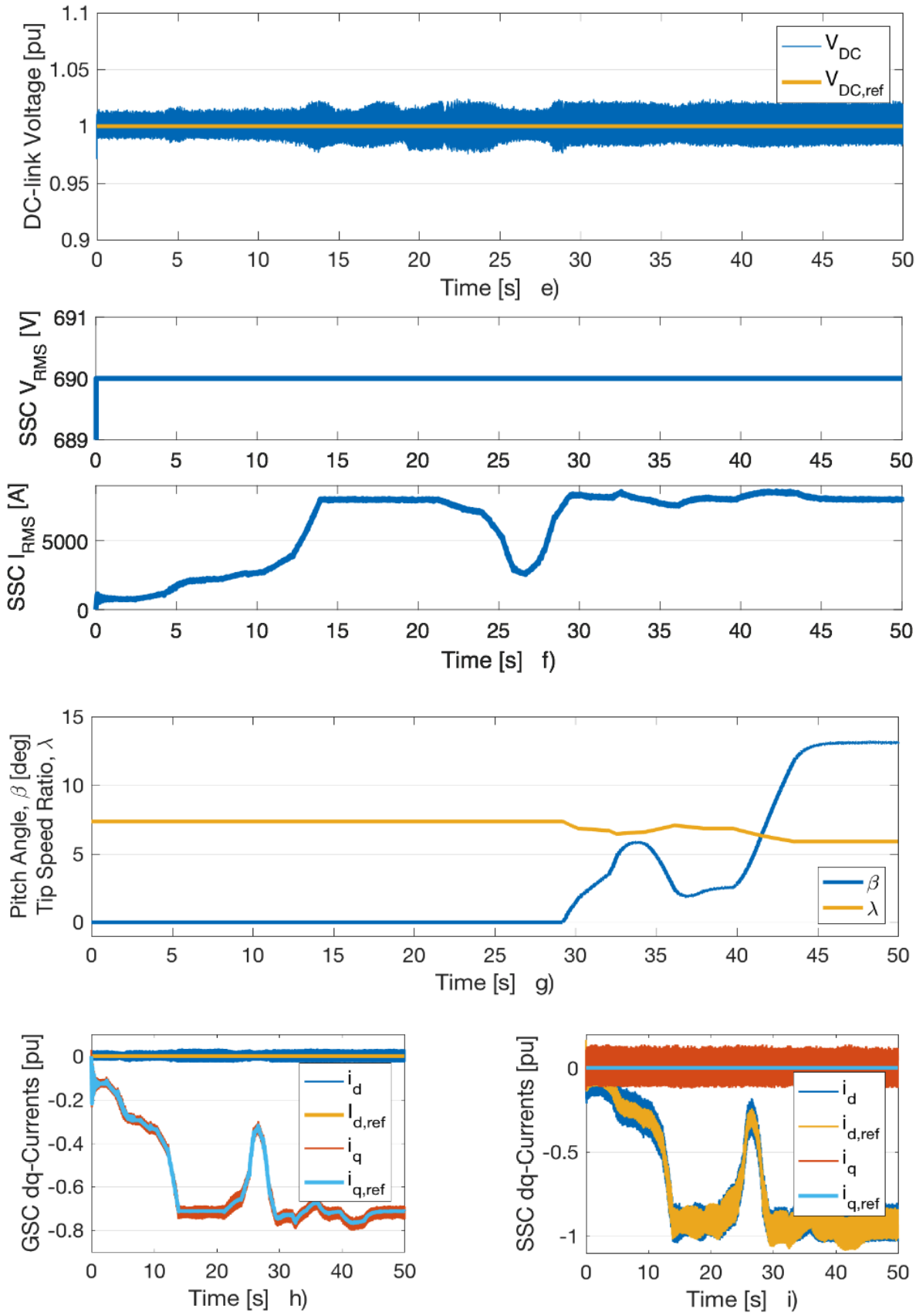

Figure 3.3. Simulation on Wind Energy System; Wind Speed, Rotor Speed, Active Power, Reactive Power, DC-link Voltage, V_{RMS}, I_{RMS}, Pitch angle, Tip speed ratio and dq-Currents.

3.5. OPERATIONAL GRID REQUIREMENTS

The transmission system operator (TSO) usually has a set of written requirements for all units that wish to connect to the power grid. These are called grid codes, and specifies voltage and frequency limits for continuous operation in addition to fault capabilities. No international standard is yet implemented, and the requirements vary somewhat between countries. A summary of European grid requirements for offshore wind power production is presented in [31].

In Norway, the grid codes are specified by Statnett, and found in [32]. The Norwegian requirements are given in table 3.4. Other European countries have stricter requirements. To generalize the results, the strictest codes will be used for the case study of this simulation. As the Norwegian requirements are within these limits, the simulations also ensure operational capability within Norway. The simulation criteria are given in table 3.5. The limits for both frequency and voltage are found to be in the German grid codes.

Table 3.4. Operational Requirements for Wind Power Production, Norway

Frequency (Hz)	Voltage (pu)	Duration
47.5 – 49.0	0.90 – 1.05	> 30 minutes
49.0 – 52.0	0.90 – 1.05	Continuous

Table 3.5. Operational Requirements for Wind Power Production, Europe

Frequency (Hz)	Voltage (pu)	Duration
46.5 – 53.5	0.873 – 1.118	> 10 seconds

The wind energy system is simulated for the operational requirements of table 3.5. The duration of the simulation is set to 12 seconds. The simulation starts at rated wind speed and a voltage of $690V$ at time $t = 0$. At time $t = 4$, the voltage drops to $0.873pu$, before rising again at $t = 8$ to $1.118pu$. This is done for a system frequency of both $46.5Hz$ and $53.5Hz$, corresponding to the operational limits of table 3.5.

Figure 3.4 shows the system's response to the variations in voltage and frequency on the grid side. The plot in a) demonstrates the rms voltages, and b) demonstrates the frequencies. Neither change appear to have any effect on the generator side voltage or frequency, and the frequency remains steady at $50Hz$. This is expected as a DC-link separates the two sides. The

amplitude of the system side voltage is also unaffected by the frequency variations, seen in c). However, as expected, slower oscillations are observed as the frequency increases.

The active power output is observed to be largely unaffected at $1pu$ for the variations in voltage and frequency. The system side output has somewhat larger oscillations for higher voltage, and the frequency alter the oscillations slightly as seen in the DC-link voltage plot in e). The DC-link voltage is also steady at $1pu$ during the whole simulation.

The simulations find the system to operate well within the operational requirements of table 3.5.

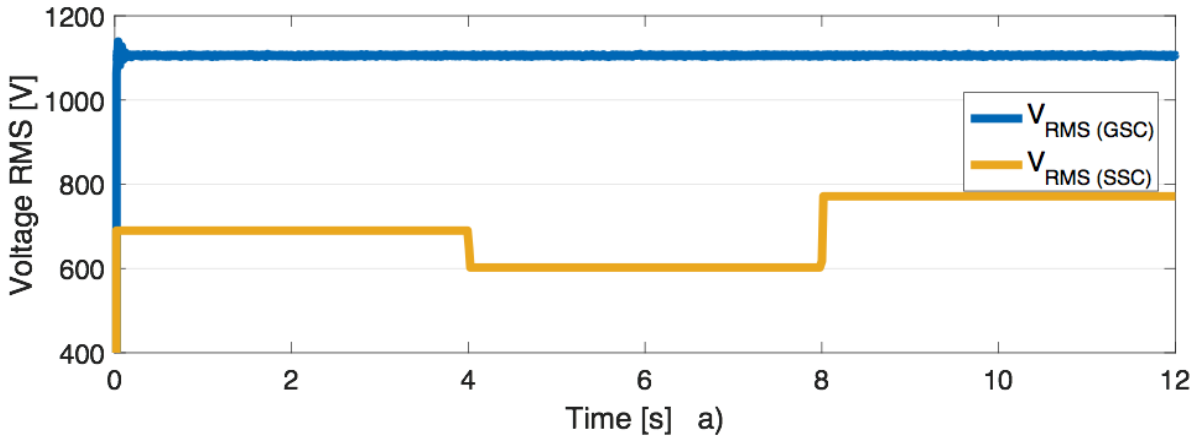

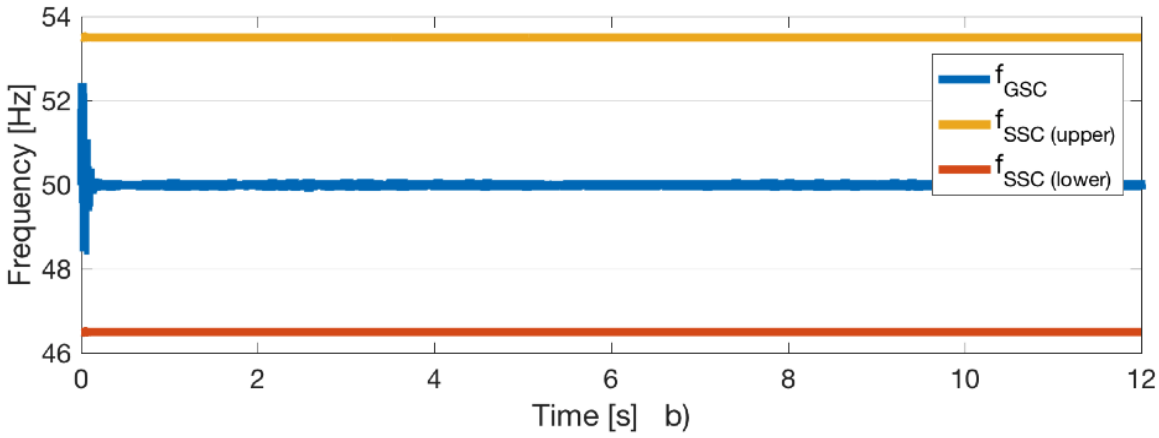

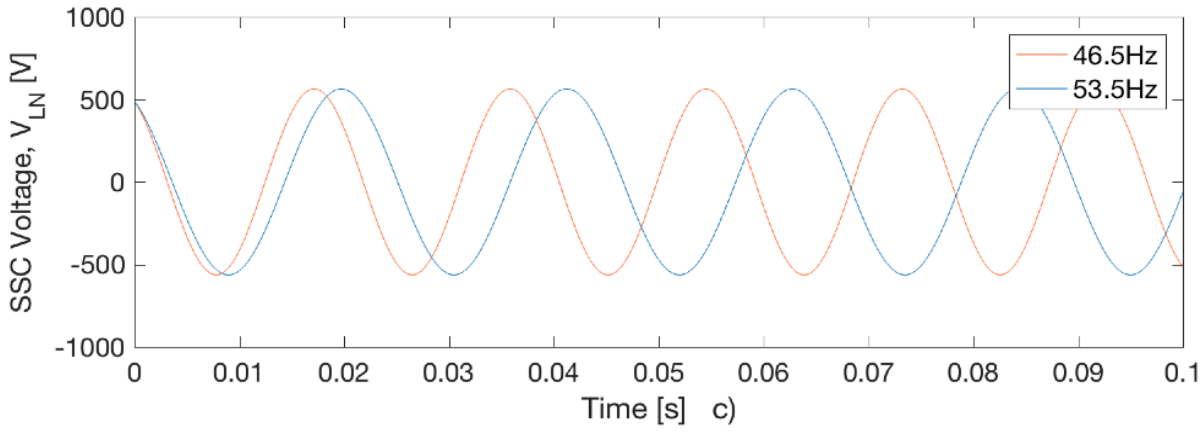

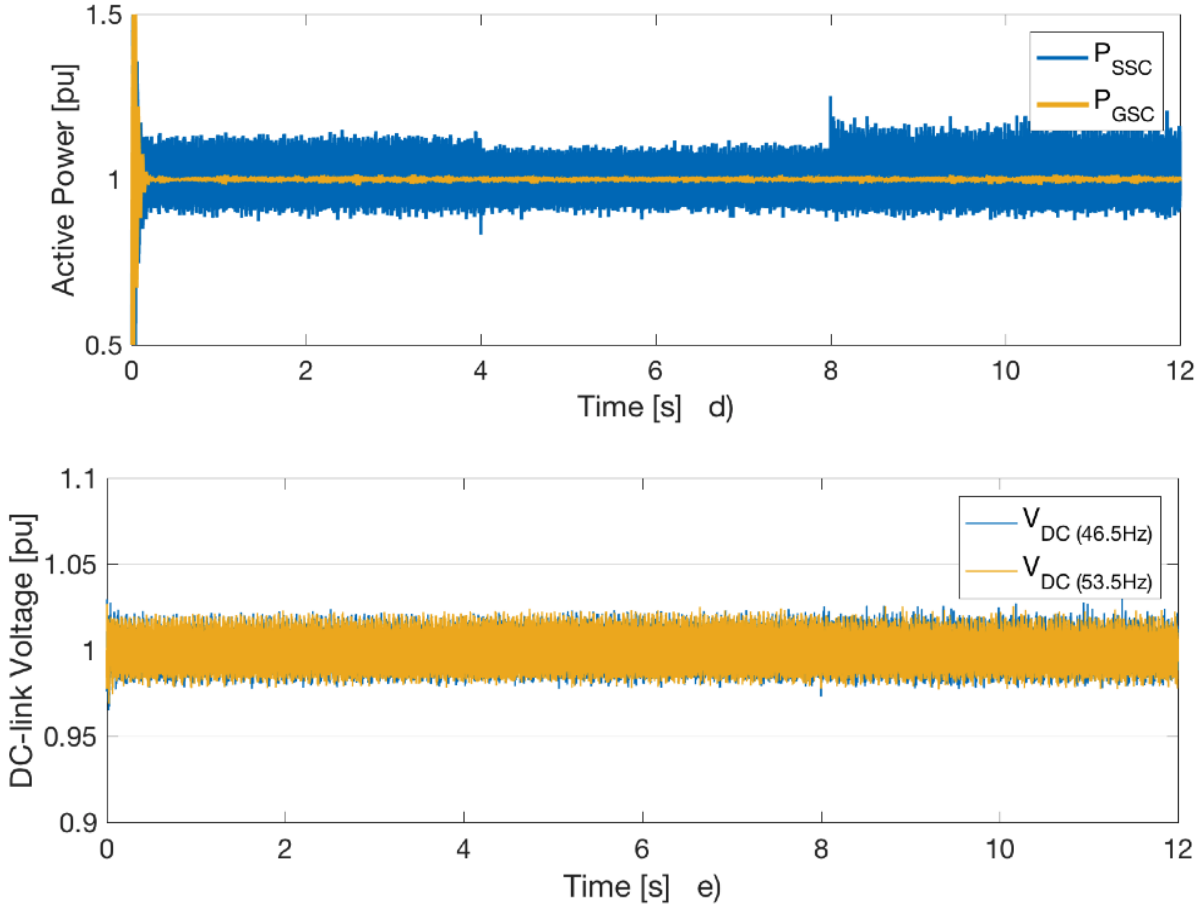

Figure 3.4. System Response to Grid Requirements in Voltage and Frequency Variations

3.6. DISCUSSION

A direct-driven variable speed PMSG wind energy system has been implemented in Matlab/Simulink and simulated for two test case scenarios. The model includes an extensive control system based on indirect control of currents through voltage source converters. The scenarios have been designed to test the correct behavior of the system by applying varying wind speeds and operating under different grid conditions. This section will look more into the results obtained from the simulations in sections 3.4 and 3.5, as well as the control tuning of appendix B. Extra focus will be on challenges encountered in the simulations and possible improvements of the model.

The control system is tuned and implemented in appendix B. By studying the bode plots of the controllers, it is concluded the controllers are stable. In addition, the tuning is tested by simulating the step response of the controllers for a large sudden wind change. By comparing the references to the actual values, the controllers are found to work both fast and accurate. At the point of step change, substantial overshoots can be observed in the currents and DC-voltage. These are caused by the generator inertia. It is here important to notice that a large

sudden wind drop would be a rare event, and similar spikes are not seen at normal operation. They are not seen for the variable speed operation of section 3.4 either.

Oscillations in DC-voltage are seen to be $\pm 2\%$ for normal operation. This must be considered acceptable. A larger capacitor or higher switching frequency could reduce the oscillations, but would have negative effects on costs and life-time of the converters. The oscillations on the system side of the wind system are seen to be bigger on than the generator side. This is due to the converters. A way to reduce these oscillations could be to model the power converters as average models. This would however, reduce the accuracy of the model and was not chosen for this thesis. Also, the sample time could be increased, at the cost of slowing the simulations. The sample time is therefore set weighing the two considerations.

The test case of section 3.4 is designed to test the implemented model's behavior in accordance with the theory presented in chapter 2. A wind profile covering a large specter of operating wind speeds is developed based on actual wind data, and applied to the wind energy system. The simulation results show that the system handles operating at different wind speeds well, and all subsystems work as intended. The first period of the simulation demonstrates operation below rated wind speeds, where the speed controller has the main task of optimizing the power output. The speed controller is both fast and accurate, and works well. For periods of fast changing winds, the oscillations are seen to increase. This demonstrates the inertial response of the system. At rated speed operation (steady state), the oscillations are as good as non-existent. The system side values are also seen to have larger oscillations than the generator side values, discussed further up. The DC-controller is seen to work well, with increasing oscillations as the power output increases. The oscillations are still considered small, and reducing them further could have negative effects as described above. For operation above rated wind speed, the pitch controller is seen to limit the power output. Both overshoots and undershoots are observed for periods of very rapid wind change as the rate limiter of the pitch angle controller does not allow for a fast-changing pitch angle. A faster rate could be implemented, but would add additional wear on the system. Also, the rapid wind changes would be rare in real life, and the rate is therefore found adequate.

The test case of section 3.5 is designed to test if, and how, the system performs at the grid voltage and frequency limits of offshore wind power production. The strictest limits given by the German grid codes are chosen to ensure adequate operation also outside of Norway. The simulations show the system maintains an excellent performance as the voltage and frequency are varied within the grid code limitations. Both the voltage and frequency on the generator side are unaffected by the variations. This is as expected as the two sides are separated by a DC-link, and not synchronized. The system is proven to work well within the grid requirements.

4. SYSTEM 2: ELECTRICAL OIL & GAS OFFSHORE INSTALLATION

Electric oil & gas offshore installations are usually isolated systems. Some onshore grid connected platforms exist, but the majority are self-powered. The most important electric components of the oil & gas platform can be summarized as either production units or load units. The load can further be divided in two major groups; passive loads and motor loads. This chapter will focus on the description of the main components of the oil and gas offshore installation. The focus will be on presenting equations and relations that are relevant for modelling applications of the given units. Other important aspects affecting the simulation of components will also be addressed.

The production units are discussed in detail in sections 4.1-4.3. Section 4.1 is a general description of oil & gas production units with focus on size and dimensioning. Sections 4.2 and 4.3 describe the gas turbine and the synchronous generator, respectively. The platform load is described in sections 4.4-4.6. Section 4.4 is a general description of oil & gas load units with focus on types and dimensioning. Sections 4.5 and 4.6 describe the induction motor and the direct torque control method, respectively.

4.1. OIL & GAS PLATFORM PRODUCTION

The production units on offshore oil & gas installations are usually thermal powered gas turbines connected to synchronous generators [33]. For units below $1MW$, diesel engines are preferred, but these are usually only kept for emergencies. A few installations have also been connected to the mainland grid, but most still rely on isolated operation.

The power supply capacity is determined based on the estimated load of the installation, slightly overdimensioned to allow for future expansions. The generator capacity should be chosen to achieve a load factor of 70-85% at normal operation, with no planned operation exceeding 80 to 85% of the generator's continuous rating. Overshoots should be limited to 125% of rated capacity. The number of gas turbine units will vary depending on the load size and the acceptance for overshoots. Usually, no less than three generators are installed. The usual setup is to have one generator installed as backup for unexpected faults and planned maintenance. For a three turbine system, the units should be dimensioned so that two units alone can handle all loads at any time. This is an important security feature for isolated systems where reserve power must be self-supplied.

Normal gas turbine capacity for oil & gas applications range from $2.5MW$ to $40MW$ per turbine. Commonly used voltages in the oil & gas industry include both $6.6kV$ and $11kV$ [33, 34]. Studies on oil & gas installations on the Norwegian continental shelf agree on using a

setup with three gas turbines, two running at any time. The turbine sizes are set between 20-25MW, aggregated to twice that for simulation purposes [35-38].

4.2. GAS TURBINE

The gas turbine is the main power supply for conventional offshore oil & gas installations. The burning of natural gas rotates a turbine and creates mechanical torque used to power an electrical generator. The generator is usually of type synchronous machine, described in section 4.3. Different approaches have been suggested for modelling gas turbines, including Physical Models, the Rowen Model, the IEEE Model and more, see [39]. This thesis utilizes the Rowen model, which gives a simplified mathematical model of a heavy-duty gas turbine.

In general, a turbine consists of a compressor, a combustion chamber and a turbine. Figure 4.1 shows this. Air is fed to a compressor, mixed with gas fuel, compressed, and burned in a combustor. The mixture will then expand through the turbine, creating mechanical torque. This process is referred to as the Brayton Cycle.

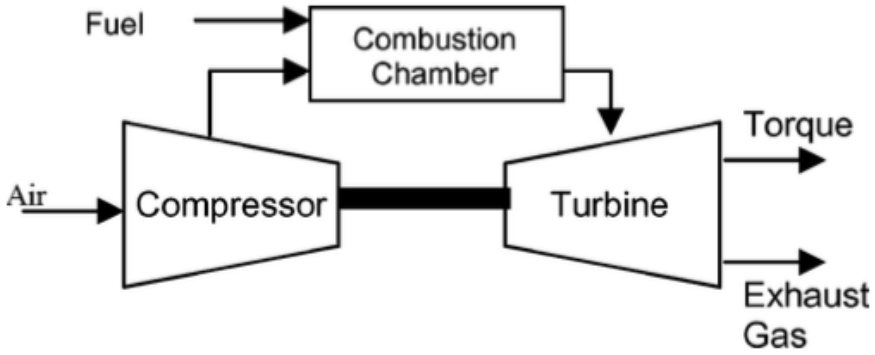

Figure 4.1. Gas Turbine Basic Model [39]

The Rowen model is a simplified mathematical model of a heavy-duty gas turbine. It was developed by General Electric for use in dynamic power system studies [40] and has been validated against actual operational data to be adequate for real life implementation. Figure 4.2 gives a block diagram of the Rowen model.

A digital set point controller controls the output torque by adjusting the speed reference. The speed governor processes the error from the rotor speed through a PI-regulator, and compares it to maximum and minimum limits. The maximum limit represents temperature control, while the lower limit should be chosen to maintain adequate fuel flow in the system. The signal is multiplied with the rotor speed to maintain synchronization with the turbine's fuel pumps. Special for gas turbines is that a minimum fraction of 0.23 fuel flow is needed to support self-sustaining no-load operation. The signal from the governor is therefore adjusted

to account for having only a 0.77 fuel fraction available for speed adjustments. Time delays for adjusting the valve positions from zero to maximum and fuel process delays connected to the combustion chamber are added. For gas turbines, the fuel feedback is zero. The fuel flow signal is then fed to a function representing the turbine, with mechanical torque as output.

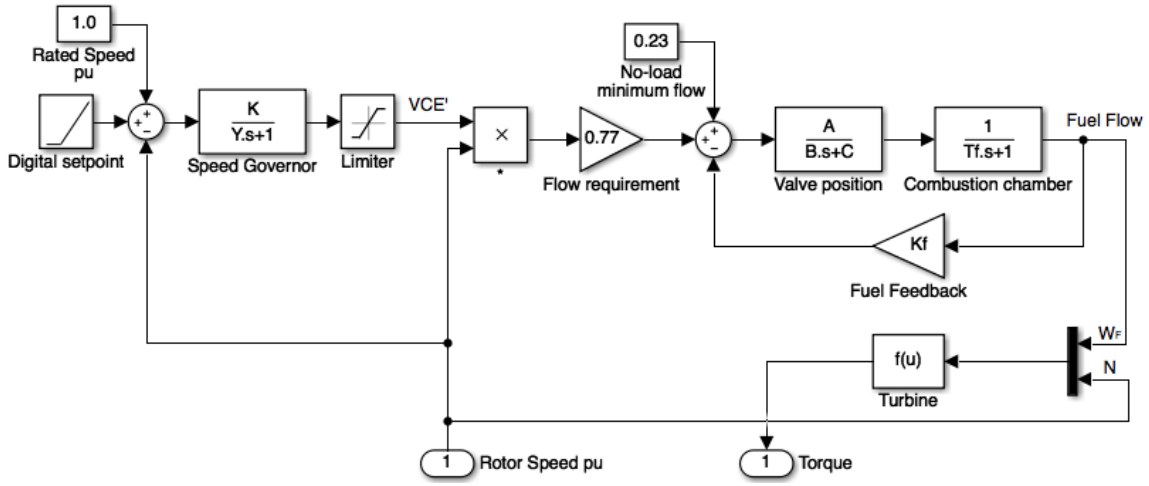

Figure 4.2. Block Diagram Representation of Rowen Model

The parameters of the process is found in [40], with *f(u)* given as:

$$f(u) = T_m = 1.3(W_F - 0.23) + 0.5(1 - N) \tag{22}$$

The model parameters are given as: $K = 30, Y = 0.05, VCE_{max} = 1.0pu, VCE_{min} = -0.1pu, A = 1, B = 0.05, C = 1, T_f = 0.4$ and $K_f = 0$.

4.2.1. Speed Control of Gas Turbine

Isolated systems and microgrids have the system frequency decided by the rotational speed of the generator, where speed is controlled by the applied turbine torque. The goal of the speed controller would be to uphold the rotor rated speed, and thereby achieve nominal frequency. The Rowen model utilizes a digital set point controller to achieve this, where the implementation could vary. One possibility would be to utilize a PI-regulator to achieve an optimal speed reference. This has proven difficult to implement as the speed reference would lie higher than the desired speed of $1pu$. In fact, the reference would vary based on the loading of the generator, where bigger loads would yield a higher reference. The PI-regulator is based on achieving zero error between the reference and the input, and is therefore deemed not to be the optimal choice. Another option would be a rule based controller, similar to the suggested controller of [14]. A simplified version has been implemented for this thesis.

The controller takes the rotational speed as input and comperes it to the rated speed of the turbine. The resulting error is considered against a rule-based table, where sign and size determines the controller output. The idea is that a bigger error gives a bigger response in

speed reference. To counter inertial effects, the step-size is reduced for smaller errors to avoid the controller working faster than the oscillations of the generator. This would destabilize the system and allow for a highly oscillating frequency. The output is set to adjust every time step, and the various step-sizes has been set through trial and failure. The resulting step-sizes ended in the range from $\frac{1}{30}T_{sample}$ to $\frac{1}{1500}T_{sample}$, where T_{sample} is the simulation sample time.

4.3. SYNCHRONOUS GENERATOR

The synchronous generator is used to convert mechanical power produced by the turbine prime-mover to *AC* electric power. A DC current is applied to the rotor windings to create an electromagnetic field. As the prime mover rotates the rotor, the rotating magnetic field induces a three-phase voltage in the stator windings. The electrical model of the machine is given in the dq-reference frame by the following equations [11, 19]:

$$v_d = -R_s i_d - \frac{d}{dt}\phi_d - \omega_m \phi_q \qquad \left(\phi_d = L_d i_d + L_{md}(i'_{fd} + i'_{kd})\right) \tag{23}$$

$$v_q = -R_s i_q - \frac{d}{dt}\phi_q + \omega_m \phi_d \qquad \left(\phi_q = L_q i_q + L_{mq} i'_{kq1}\right) \tag{24}$$

for the stator, and for the rotor:

$$v_{fd} = R'_{fd} i'_{fd} + \frac{d}{dt}\phi'_{fd} \qquad \left(\phi_d = L'_{fd} i'_{fd} + L_{md}(i_d + i'_{kd})\right) \tag{25}$$

$$v_{kd} = R'_{kd} i'_{kd} + \frac{d}{dt}\phi'_{kd} \qquad \left(\phi_{kd} = L'_{kd} i'_{kd} + L_{md}(i_d + i'_{fd})\right) \tag{26}$$

$$v_{kq1} = R'_{kq1} i'_{kq1} + \frac{d}{dt}\phi'_{kq1} \qquad \left(\phi_{kq1} = L'_{kq1} i'_{kq1} + L_{mq} i_q\right) \tag{27}$$

$$v_{kq2} = R'_{kq2} i'_{kq2} + \frac{d}{dt}\phi'_{kq2} \qquad \left(\phi_{kq2} = L'_{kq2} i'_{kq2} + L_{mq} i_q\right) \tag{28}$$

where v_{dq} and i_{dq} represents the induced voltages and currents, R represents the resistances and ϕ_{dq} represents the flux. All the rotor parameters and quantities are viewed from the stator, marked as an apostrophe. The subscript *f* represents the rotor field winding, while *k* represents the rotor damper windings with *kd* on the same axis as the *fd* field winding. The $\frac{d}{dt}\phi_{dq}$ term represents the rate of change of flux due to changes in the axis currents. It is referred to as the transformer emf. Also, an important observation is how the d- and q-axis voltages get induced by the q- and d-axis fluxes respectively. Figure 4.4 gives the equivalent circuit of the synchronous machine based on the above equations [41].

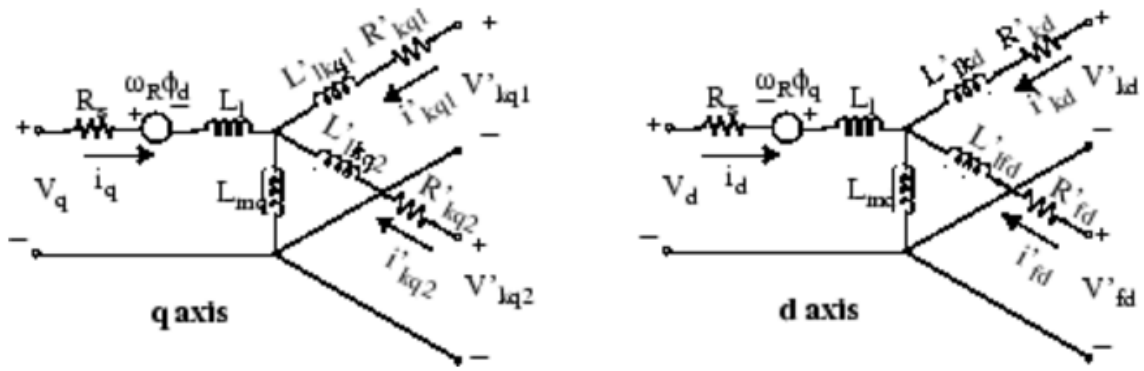

Figure 4.3. Equivalent Circuit of Synchronous Generator in dq-frame [41]

The impedances are usually specified in three different states; steady state (*X*), transient state (*X'*) and subtransient state (*X''*). This is due to the impedances' effective value not staying constant when the current changes. In the subtransient state, directly after the change of current, the flux path is almost entirely through air to keep the linkage flux constant. After a while some flux will again enter the rotor windings in what is the transient state. The flux will thereby return also to the field windings to resume steady state operation. For the different states, the magnitude of the impedances follows $X'' > X' > X$.

The active and reactive power produced by a round-rotor synchronous generator are:

$$P = \frac{E_A V_\phi}{X_S} \sin \delta \tag{29}$$

$$Q = \frac{E_A V_\phi}{X_S} \cos \delta - \frac{{V_\phi}^2}{X_S} \tag{30}$$

where E_A is the internal generated voltage, V_ϕ the terminal voltage, X_S the stator reactance and δ the torque angle of the machine. Power systems usually have loads consisting of induction motors which need reactive power for consumption. Synchronous generators therefore often run in overexcited mode, with a high E_A and high field current for positive delivery of reactive power.

For operation in an isolated system the voltages cannot be treated as if connected to an infinite grid. The voltages will instead fluctuate at sudden changes in load or production. As the internal generated voltage, E_A has time delays associated with the excitation process, the terminal voltage V_ϕ and the torque angle δ must adjust to maintain power balance. A loss of production will then lead to an increasing angle δ, while a loss of load similarly will decrease δ. This might also affect the reactive power production which might go above rated value. The system will stabilize as the internal voltage E_A adjusts after the excitation time delay, and will adjust the terminal voltage to an acceptable value.

4.4. OIL & GAS PLATFORM LOAD

The load units on offshore oil & gas installations are usually made of three groups; variable speed drives (VSD), direct online AC motors and passive loads [33]. The VSD AC motors represent big motors without direct online start capability. These are used for drilling, pumps, fans, etc. The direct online AC motors work at constant speed, and can be used for water injection pumps, cooling purposes and compressors. The passive loads are mostly for heating and utility purposes and can be modelled purely resistive.

The total load size of oil & gas installations could range from around ten to several hundred megawatts. Studies on oil & gas installations on the Norwegian continental shelf estimates the platform load to be in the range of either $20MW$ to $35MW$ [35, 36, 42], or $40MW$ to $70MW$ [37, 38, 43]. The individual motor sizes are in the range of $5MVA$ to $8MVA$, or aggregated to about twice that [37, 38, 44]. Commonly used voltages in the oil & gas industry include both $6.6kV$ and $11kV$ [33].

The motor load input is modeled as a mechanical torque profile. This can be done in several ways, one being applying a constant value torque at some level between zero and nominal. This can be used for appliances such as a compressor. Another possibility is to model the load torque as a function of the rotational speed, used for fans, pumps and drilling with varying speed operation. The resulting torque T_L can then be expressed as the quadric function of the rotational speed ω_m, given as [45]:

$$T_L = k * \omega_m^2 \tag{31}$$

The constant k is then determined by the nominal torque T_n and the base mechanical rotational speed ω_{mb} as follows:

$$k = \frac{T_n}{\omega_{mb}^2} \tag{32}$$

4.5. INDUCTION MOTOR

The induction motor operates by inducing voltages and currents in the machine rotor. This is achieved by applying a three-phase set of currents to the stator windings, which creates a rotating magnetic field of synchronous speed, ω_{sync}. The amplitude is determined by the electric frequency of the currents and the number of poles in the machine. This rotating magnetic field induces an alternating voltage in the rotor bars, rotating the rotor. The electrical rotor speed ω_{em} increases as a result of the relative speed difference with the stator magnetic field. The rotor speed is always lower than the synchronous speed, as $\omega_{em} = \omega_{sync}$ would give no relative velocity and therefore no induced voltage. The difference in relative motion is referred to as the slip, and is given as the per unit size [46]:

$$s = \frac{\omega_{sync} - \omega_{em}}{\omega_{sync}} \tag{33}$$

The complete electrical model of the machine is given in the dq-reference frame by following equations [16]:

$$v_{qs} = R_s i_{qs} + \frac{d}{dt}\varphi_{qs} + \omega\varphi_{ds} \qquad \left(\phi_{qs} = L_s i_{qs} + L_m i'_{dr}\right) \tag{34}$$

$$v_{ds} = R_s i_{ds} + \frac{d}{dt}\varphi_{ds} - \omega\varphi_{qs} \qquad \left(\phi_{ds} = L_s i_{ds} + L_m i'_{qr}\right) \tag{35}$$

$$v'_{qr} = R'_r i'_{qr} + \frac{d}{dt}\varphi'_{qr} + \omega_r \varphi'_{dr} \qquad \left(\phi'_{qr} = L'_r i'_{qr} + L_m i_{qs}\right) \tag{36}$$

$$v'_{dr} = R'_r i'_{dr} + \frac{d}{dt}\varphi'_{dr} - \omega_r \varphi'_{qr} \qquad \left(\phi'_{dr} = L'_r i'_{dr} + L_m i_{ds}\right) \tag{37}$$

where v_{dqs} and i_{dqs} represent the stator voltages and currents, v_{dqr} and i_{dqr} represent the induced voltages and currents in the rotor, *R* and *L* represent the machine resistance and inductance, and ϕ_{dq} represents the fluxes of the machine windings. All rotor quantities are viewed from the stator, marked by an apostrophe.

The angular velocity ω represents the instantaneous speed of the reference frame axes compared to the stator's a-axis. It is defined as the time derivate $\frac{d}{dt}\theta_{d,a}$, where $\theta_{d,a}$ is the angle between the a-axis and the reference frame d-axis. The angle between the a-axis and q-axis θ_e, can then be given as:

$$\theta_e = \sin^{-1}\frac{\phi_{qs}}{\hat{\phi}_s} \tag{38}$$

$$\hat{\phi}_s = \sqrt{\phi_{ds}^2 + \phi_{qs}^2} \tag{39}$$

Similarly, $\omega_r = \frac{d}{dt}\theta_{d,a'}$ gives the electrical instantaneous speed of the d-axis relative to the a'-axis of the rotor. The velocities relate to the actual electrical speed of the rotor as:

$$\omega_{em} = \omega - \omega_r \tag{40}$$

The value of ω is usually set to ω_{sync}, which gives $\omega_r = \omega_{slip}$. This has the advantage of having all the voltage, current and flux quantities as DC-values, simplifying the control scheme and the PI-controller implementation.

Figure 4.5 gives the equivalent circuit of the induction motor based on the equations presented above [47]. The inductances in the figure are related to the inductances of the above equations as $L_s = L_{ls} + L_m$ and $L'_r = L'_{lr} + L_m$.

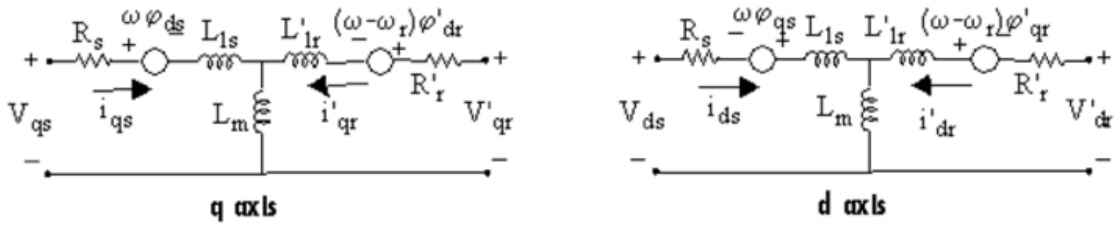

Figure 4.4. Equivalent Circuit of Induction Machine in dq-Reference Frame [47]

The electric torque T_e of the machine is given as:

$$T_e = 1.5p\left(\varphi_{ds} i_{qs} - \varphi_{qs} i_{ds}\right) \tag{41}$$

where *p* is the number of pole pairs in the machine. The mechanical drive train can be included to combine the mechanical and electrical parts of the machine, as for the PMSG. The following equation describes the acceleration $\frac{d\omega_m}{dt}$ as the difference between the electromagnetic torque T_e and the load torque T_m acting on the combined inertia *J* as:

$$\frac{d\omega_m}{dt} = \frac{T_e - T_m}{J} \tag{42}$$

Some reactive power consumption is necessary for the motor to work properly. Reactive power supports the system voltage, and are for motors required to convert the power to useful work [48].

The induction motor requires substantially larger currents at start-up than for normal operation. For big motors the start-up currents are often found to be $\backsim 5$ times the nominal current. This may result in unwanted voltage dips. It is therefore often a priority to reduce these currents as will be discussed more in section 4.6.

4.6. Direct Torque Control of Induction Motor Drive

Variable speed drives (VSD) are equipment that provide torque and speed control of electric machines. Several methods of implementation exist, such as slip-power control, scalar control, field-oriented control and direct torque control, see [34]. In this thesis, the direct torque control (DTC) method is utilized for control of the induction motors. The method provides several advantages compared to other AC drives, such as more accurate control at low speeds, better matching of the load requirement, smooth motor operation at rated torque for zero speed reversal, and faster response compared to the indirect current control of the field-oriented method [49].

The idea behind direct torque control is to directly control the torque and flux of the machine through a speed reference. The actual control is achieved through hysteresis controllers, creating a switching signal for the three-phase inverter [34, 50]. Figure 4.6 shows the DTC control scheme [34].

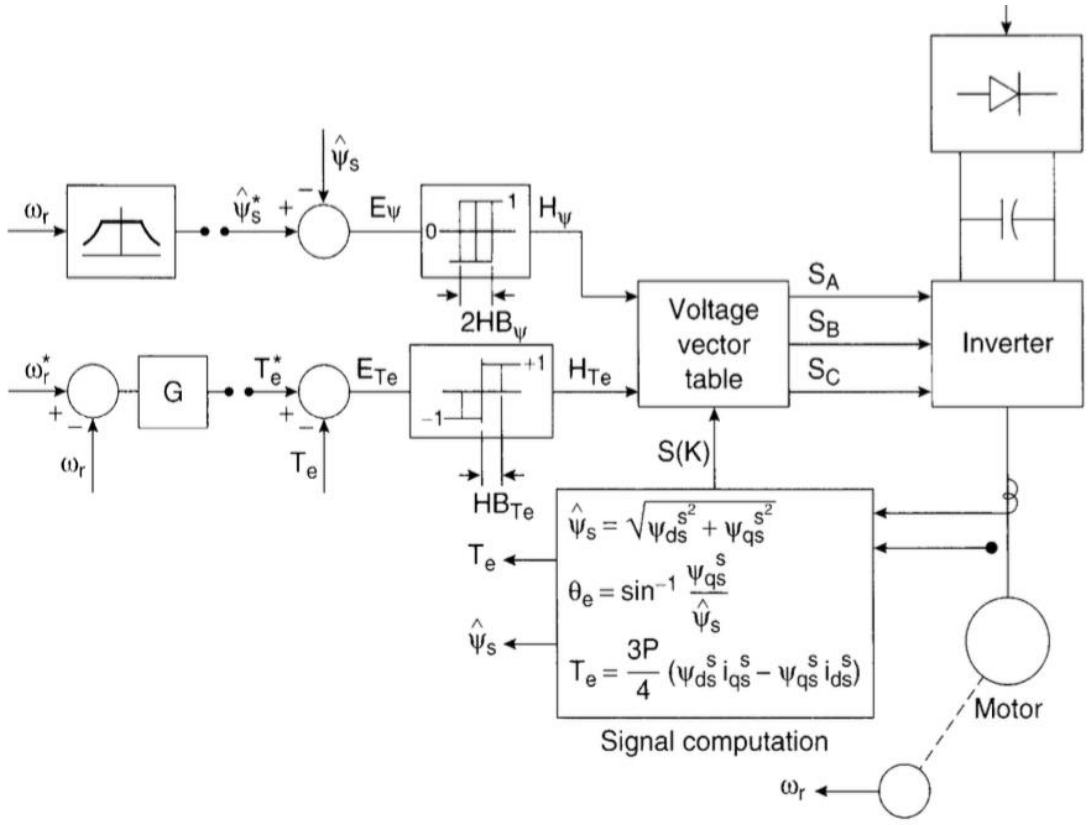

Figure 4.5. Block Diagram of Direct Flux and Torque Control [34]

The induction motor three-phase voltages and currents are measured along with the rotor mechanical speed. The rotor speed ω_m is compared to a reference signal $\omega_{m,ref}$, and processed by a PI-controller to provide the torque reference signal. See figure 4.7. The measured speed is also used to provide the flux reference signal. The flux signal is given as:

$$\phi_{ref} = \frac{\omega_{m,base}}{\omega_m}\phi_{base} \tag{43}$$

where $\omega_{m,base}$ is the rated mechanical rotor speed of the induction motor, and ϕ_{base} is the base flux value at rated conditions in the machine. The value of $\frac{\omega_{m,base}}{\omega_m}$ is set to always be ≤ 1, being equal to 1 as long as ω_m is below rated speed. The flux reference is therefore equal to ϕ_{base} inside the rated region, and only drops for speeds higher than rated value.

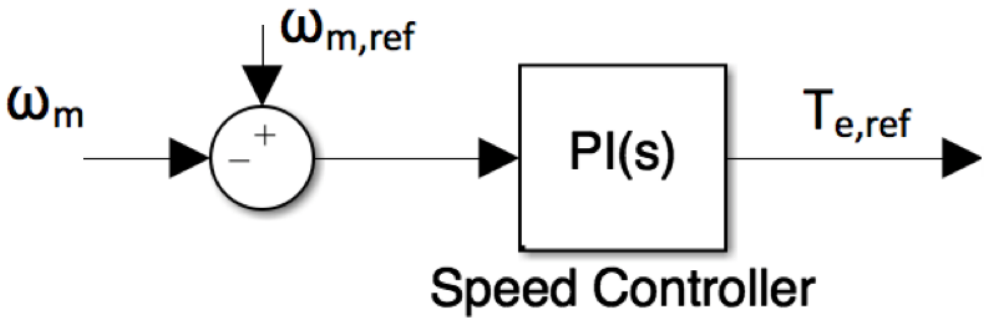

Figure 4.6. Block Diagram of DTC Speed Controller

The measured three-phase voltages and currents are transformed to the dq-reference frame, and fed to a flux and torque estimator. The estimator utilizes the relations given by equations (38), (39) and (41) in section 4.5, to estimate the values of electric torque $T_{e,est}$, flux ϕ_{est} and electric angle $\theta_{e,est}$. The estimated torque and flux are fed to hysteresis controllers together with their computed reference signals. The hysteresis controller works similar to a switch, switching state every time the error crosses outside of the hysteresis-band limits. The switching states are given as:

$$H_\phi = +1 \qquad , error_\phi > HB_\phi \tag{44}$$

$$H_\phi = -1 \qquad , error_\phi < -HB_\phi \tag{45}$$

$$H_{Te} = +1 \qquad , error_{Te} > HB_{Te} \tag{46}$$

$$H_{Te} = \ 0 \qquad , -HB_{Te} < error_{Te} < HB_{Te} \tag{47}$$

$$H_{Te} = -1 \qquad , error_{Te} < -HB_{Te} \tag{48}$$

where *H* is the hysteresis output, and *HB* is the band-limit of a band of size 2*HB*.

By neglecting resistance, the stator flux ϕ can be expressed as a function of the stator voltage V_s as:

$$V_s = \frac{d}{dt}\phi \tag{49}$$

This means the stator flux can be controlled by applying the stator voltage over a small time period. The controllability of the stator flux is therefore dependent on determining the correct sector of the stator flux, which is given by the angle $\theta_{e,est}$, placing the signal in one of six sectors of width $\pi/3$. Each sector has a set of voltage vectors that are utilized for controlling the inverter gates. The hysteresis controller outputs are used to determine what vector voltage is used at a specific time, by utilizing a lookup-table. Table 4.1 gives the associated switching signals of each combination of hysteresis controller output for each flux sector, *S* [51].

Table 4.1. Switching Signal of Inverter Voltage Vectors

H_ϕ	H_{Te}	S_1	S_2	S_3	S_4	S_5	S_6
1	1	100101	101001	011001	011010	010110	100110
	0	010101	101010	010101	101010	010101	101010
	-1	010110	100110	100101	101001	011001	011010
-1	1	101001	011001	011010	010110	100110	100101
	0	101010	010101	101010	010101	101010	010101
	-1	011010	010110	100110	100101	101001	011001

The DC-side of the inverter consists of a braking chopper in parallel with a capacitor. The capacitor is included to smooth oscillations in the DC-voltage, while the braking chopper limits the DC-voltage. The braking chopper is modeled as a resistor in series with a diode and a switch. The switch is controlled by a gate signal activated as the voltage exceeds the DC-voltage. The actual switching pattern is determined by a hysteresis band. The switching transfers excess power to the resistor which converts the energy to heat. The system side of the DTC is connected through a diode rectifier. This removes the need for switching signals grid side, simplifying the motor control. The choice of diodes means that electric power can only go from grid to motor, and not opposite way. This is found acceptable for motor drive operation.

The direct torque controller works by directly controlling the machine torque and flux. This gives excellent control of the currents for transient operations as loading and unloading of the machine, but has been found insufficient for the motor starting [50]. The starting often results in a high current spike as the machine is excited. A combination of both DTC and soft starting has been found necessary to reduce the starting current to an acceptable level. Different methods for soft starting exist, see [46, 52]. Given the limited time of this thesis, a simpler method of adding a varying resistance in series with the DTC has been implemented with some luck, reducing the starting current to about 1.25 times the loading current.

5. SYSTEM 2: SIMULATIONS ON ELECTRICAL OIL & GAS OFFSHORE INSTALLATION

The following chapter will focus on simulations of the oil & gas platform microgrid, referred to as system 2. The goal of the chapter is to verify the correct modeling and functioning of the system. This provides a basis for use in further simulations of the bigger wind integrated oil & gas offshore installation given in chapter 6. Figure 5.1 shows a simple schematic of the simulated system.

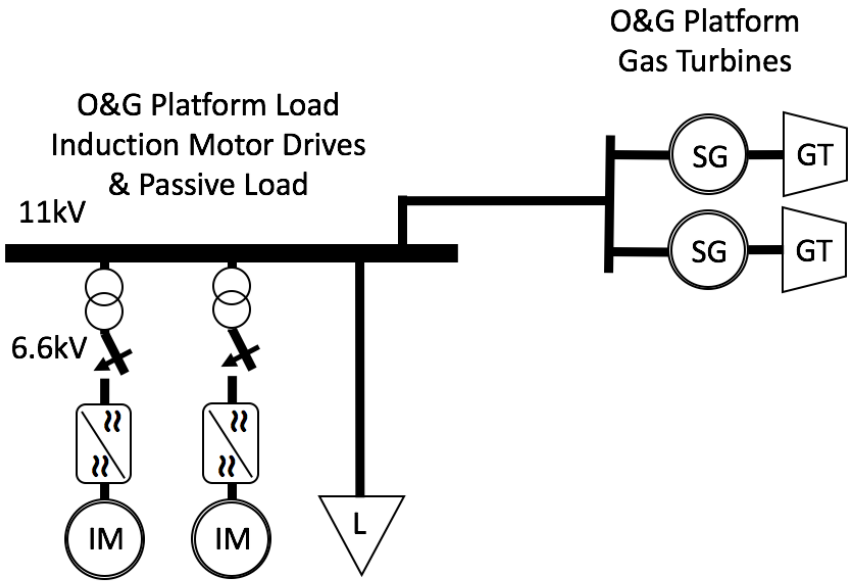

Figure 5.1. Oil & Gas Platform Microgrid

The chapter is organized in seven subsections. Section 5.1 presents the numerical parameters used for the simulations. Section 5.2 presents the operational requirements for offshore AC distribution systems as specified by NORSOK E-001. Section 5.3 describes the model implementation in Matlab/Simulink. Separate testing of the gas turbine system and the induction motor drive are found in sections 5.4 and 5.5 respectively. Section 5.6 gives the complete microgrid, simulated for two test cases. The test cases are the start of an induction motor drive, and the loss of load. Section 5.7 discusses the results of the simulations.

5.1. NUMERICAL PARAMETERS

Table 5.1 gives the parameters of the oil & gas offshore installation. The values are based on parameters found in similar studies on oil & gas installations, see section 4.1. The base values are the rated power and voltage of the gas turbine.

Table 5.1. Parameters of Oil & Gas Platform

Parameter	*Value*
Generator Rating *(P)*	46MVA
Maximum Load *(P)*	35MW
Nominal Voltage *(V)*	11kV
Platform Frequency *(f)*	50Hz
Generator Inertia *(H)*	3s

Table 5.2 gives the parameters of the Synchronous Generator. The values are found in [11]. The base values are the rated power and voltage of the gas turbine.

Table 5.2. Parameters of Synchronous Generator

Parameter	*Value*
Stator resistance *(R_s)*	0.003pu
Synchronous d-axis Reactance *(X_d)*	0.91pu
Synchronous q-axis Reactance *(X_q)*	0.66pu
Transient d-axis Reactance *(X_d')*	0.3pu
Subtransient d-axis Reactance *(X_d'')*	0.24pu
Subtransient q-axis Reactance *(X_q'')*	0.15pu
Transient d-axis Time Constant *(T_d')*	1.1
Subtransient d-axis Time Constant *(T_d'')*	0.05
Subtransient q-axis Time Constant *(T_q'')*	0.06
Pole pairs *(p)*	2

Table 5.3 gives the parameters of the Induction Motor Drive. The values are found in [33][1], or based on similar studies on oil & gas installations, see section 4.4[2]. The braking chopper parameters are calculated based on equations given in [53][3]. The base values are the rated power and voltage of the induction motor drive.

Table 5.3. Parameters of Induction Motor Drive

Parameter	*Value*
Nominal Power *(P)*[2]	8MVA
Nominal Voltage *(V)*[1]	6.6kV
Frequency *(f)*[2]	50Hz
Breaker Resistance *(R_{DC})*[3]	11Ω
DC-link Capacitor *(C_{DC})*[3]	14.3mF

Table 5.4 gives the parameters of the Induction Motor. The values are found in [33]. The base values are the rated power and voltage of the induction motor drive.

Table 5.4. Parameters of Induction Motor

Parameter	*Value*
Stator Resistance *(R_s)*	0.0039pu
Rotor Resistance *(R_r)*	0.0055pu
Stator Reactance *(X_{ls})*	0.1550pu
Stator Reactance *(X_{lr})*	0.1186pu
Mutual Reactance *(X_m)*	4.2170pu
Pole pairs *(p)*	1
Inertia Constant *(H)*	0.82s

5.2. NORSOK LIMITS FOR OFFSHORE AC DISTRIBUTION SYSTEMS

The NORSOK standard sets operational requirements for offshore AC distribution systems. The requirements are in line with the IEC's standards (International Electrotechnical Commission), and specified in [54]. Table 5.5 gives a summary of the relevant requirements for voltage and frequency for offshore AC networks.

Table 5.5. NORSOK Limits for Offshore AC Distribution Systems

	Voltage (pu)	**Frequency (pu)**
Stationary Limits	0.90 – 1.06	0.95 – 1.05
Transient Limits	0.80 – 1.20	0.90 – 1.10

5.3. MODEL IMPLEMENTATION OF OIL & GAS PLATFORM MICROGRID

The oil & gas platform microgrid is modelled and implemented in Matlab/Simulink. The gas turbine model is implemented in the per unit system by the author, based on the block diagram developed in section 4.2. The synchronous generator is a built-in block in the Simscape Power Systems package, and based on the equations of section 4.3. The machine is excited by another built-in block, excitation system 1.

The induction motor drive is developed by the author based on the relations given in section 4.6. The induction machine used is the built-in asynchronous machine block, based on the equations of section 4.5, and [53]. The power converters are the built-in universal bridge blocks, where the IGBT/diode converter is implemented as a switching device for higher accuracy. The braking chopper is developed by the author. The passive load is a built-in three-phase load block, modeled purely resistive.

The complete microgrid is put together by the author, consisting of the units described above. A built-in transformer block is included to connect the lower voltage induction motor drives to the platform. The complete Simulink schematics can be seen in appendix C.

5.4. GAS TURBINE W/ SYNCHRONOUS GENERATOR: OPERATION FOR LOAD VARIATIONS

The gas turbine system is simulated to verify to correct build and tuning of the model constructed in Matlab/Simulink. The gas turbine unit is coupled with a synchronous generator, with parameters as specified in section 5.1. The generator is connected to a passive resistive load, and the system response is observed for the two cases of adding load and losing load. The duration of the simulation is set to 50 seconds.

Figure 5.2 demonstrates the load profile applied to the generator unit. The initial load is set to $0.7pu$ of rated generator power. At time $t = 20s$, an additional 42% load is added to the system for a total load of $0.85pu$. This corresponds to the upper recommended load limit of $80 - 85\%$. At time $t = 35s$, the system experiences a sudden loss of 60% load, giving a new loading of $0.34pu$.

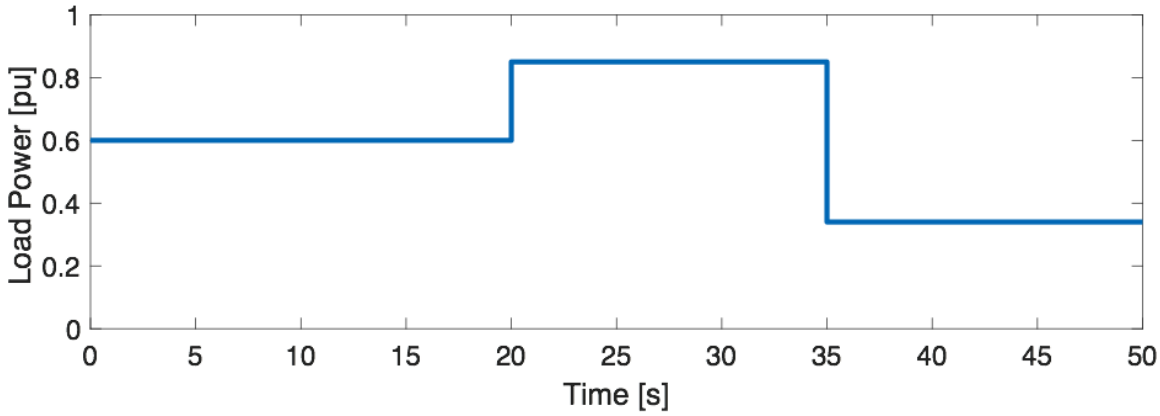

Figure 5.2. Load Power Profile with Varying Resistive Load

Figure 5.3 demonstrates the response of the system to the variations in resistive load. The rotor speed is shown in a), and shows the rotational speed compared to the reference. The speed controller is seen to maintain the speed of 1pu for varying loads, which corresponds to upholding a frequency of 50Hz. The inertia of the system is seen to affect the system for the starting of the system, and for sudden changes in load, but the system stabilizes after just over 5 seconds. The largest frequency drop is seen to be at start-up, corresponding to just over 5%. This is well within the transient limits of the NORSOK requirements. Adding 42% additional load, and losing 60% load are seen to give a frequency drop and overshoot of 2% and 3.5% respectively. Also well within the NORSOK limits. The speed is seen to lie slightly below the reference speed, the distance decided by the loading of the machine. This is because the electric machine power P_e of the generator is slightly larger than the resulting output power P_{eo}, affected by the load as seen in b). The generator power is otherwise seen to nicely follow the load power, with a fast response.

The rms voltage and current of the machine are shown in c) and d) respectively. The terminal voltage is observed to maintain a rated value of 11kV for the duration of the simulation, with the inertia giving some oscillations at the time of the load variations. Starting the machine at 60% load is seen to give an overshoot of 15% due to inertia, which is within the transient limits of the NORSOK limits. The increasing of load with 42% is seen to give a voltage drop of $\sim 2.5\%$, while losing 60% load is seen to give an overshoot of $\sim 12.5\%$, which is also within the transient NORSOK limits. The stator rms current demonstrates how the current is adjusting for the changing output power. The shape of the current is seen to match both the machine output power and the load power profile applied to the generator.

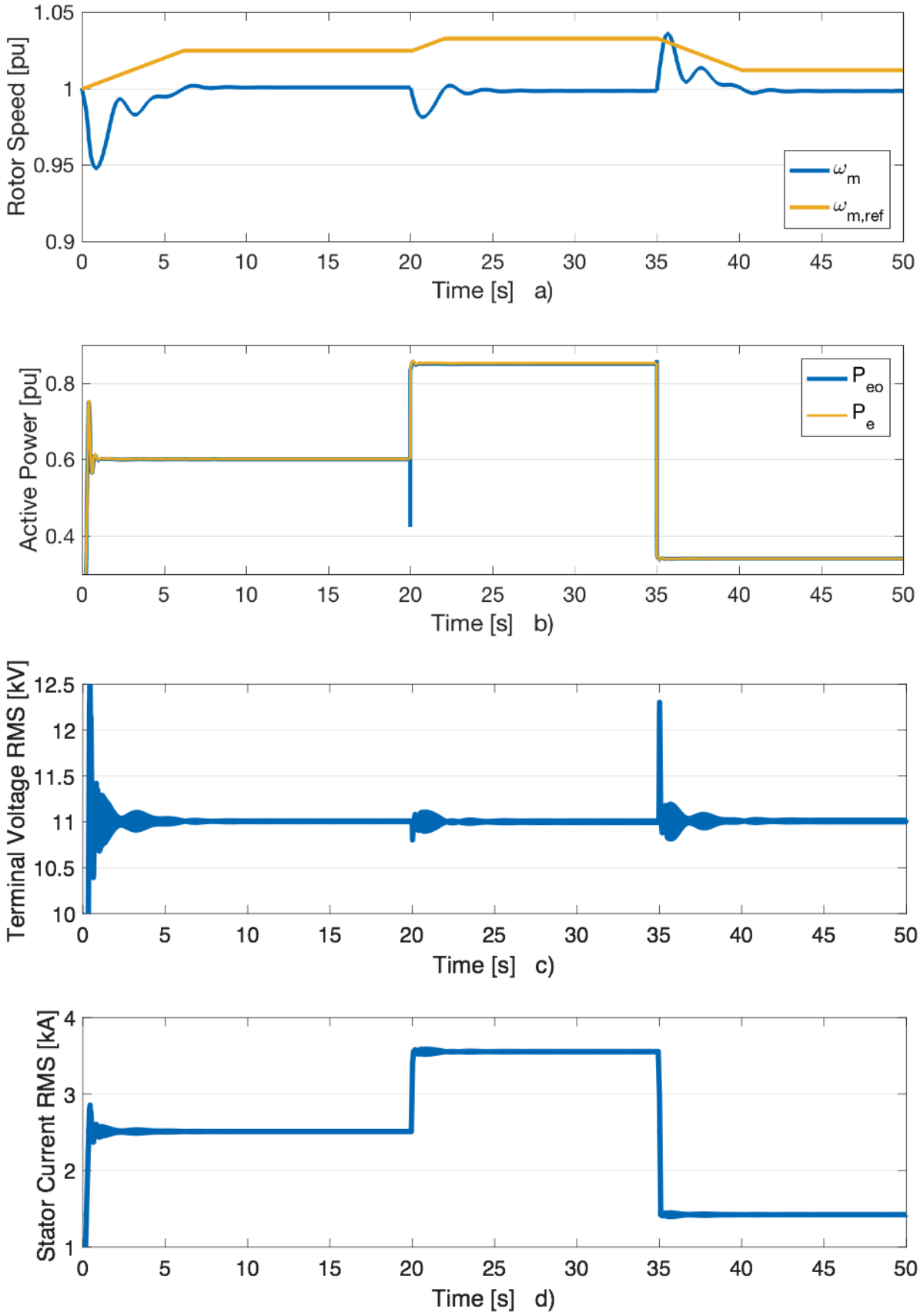

Figure 5.3. Simulation of Gas Turbine w/ Synchronous Generator at Varying Loads

5.5. Induction Motor Drive: Variable Speed and Torque Operation

The Induction motor drive is simulated to verify the correct build and working of the model. The model is built in Matlab/Simulink with parameters as specified in section 5.1. The drive is of type direct torque control as described in section 4.6. The motor drive is connected to an ideal grid, and tested by varying the speed and torque input parameters of the drive. The simulation has a duration of 20 seconds. Figure 5.4 demonstrates the response of the induction motor drive to variations in the applied speed reference and load torque.

The machine starts accelerating at time $t = 0$, and reaches nominal speed after $3.33s$. From a) it is seen how the machine speed matches the reference with high accuracy. The inertia affects the system only noteworthy after the system reach negative rated speed, with an overshoot of about 10%. The starting current of the machine is seen to reach 117% of the rated current of $1212A$ in d). As described in section 4.6, the DTC does not control start-up current directly, requiring a soft-starter device. A simple varying resistance has been added at start-up to limit the starting currents. Without the resistance, the start-up current was found to be $3600A$, significantly higher than with the varying resistance.

At time $t = 3s$, the nominal load torque is applied to the system while still under acceleration. This forces the electromagnetic torque to increase to an upper decided limit of 1.5 nominal torque, as seen in b). The limit is set to avoid overshoots, and limits the machine current. This lasts until the speed reaches nominal speed, and the electromagnetic torque stabilizes at nominal torque equal to the load torque. The torque is seen to have high oscillations throughout the simulations due to the fast rotor speed of the motor. An increase in stator current is observed for the applying of load torque, before settling as the speed reaches nominal value. At this point the system operates at rated conditions, as seen by the active power plotted in e).

At time $t = 7s$, the nominal torque is suddenly inverted. This is not a likely thing to happen in real life, but is included to demonstrate the speed and capability of the direct torque control method. The electromagnetic torque is seen to inverse similarly without any noteworthy delay. The inversion corresponds to the nominal generation torque of the machine, as seen from the active power. The diode bridge prohibits generation and the grid side power is therefore zero. The machine then operates at negative rated power. The generator operation demonstrates the excellent performance of the direct torque control as the speed reverses through zero. An overshoot in the DC-link voltage is observed in c) as the braking switch adds the resistor consuming the excess power.

At time $t = 12s$, the speed reference changes to negative rated speed, and the machine is seen to start deaccelerating. The electromagnetic torque is again forced to decrease to a decided torque limit for the deceleration period. As the speed reaches zero, the system is seen to draw active power from the grid. The machine then stabilizes at negative

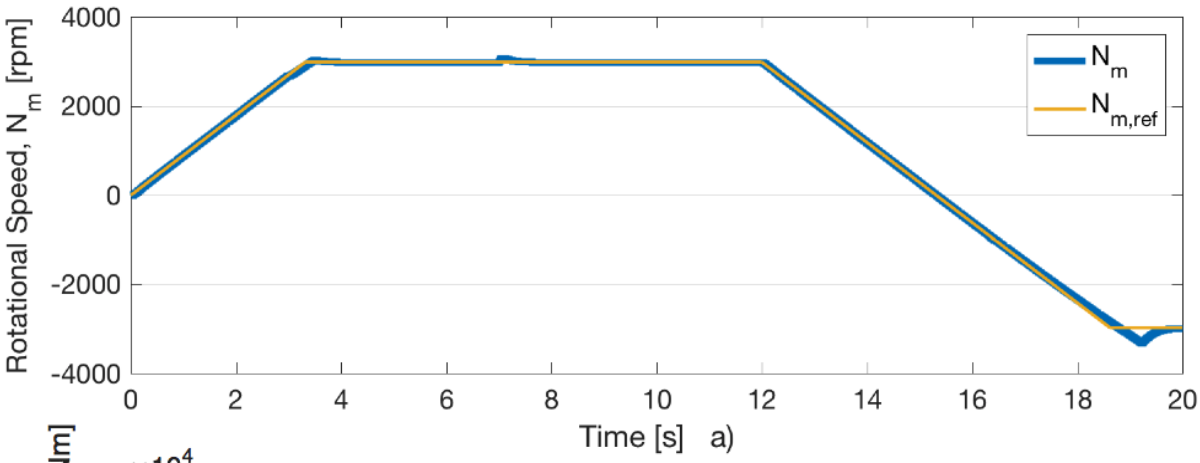
Rotational Speed, N_m [rpm]
4000
2000
0
-2000
-4000
0
2
4
6
8
10
12
14
16
18
20
Time [s] a)
N_m
$N_{m,ref}$

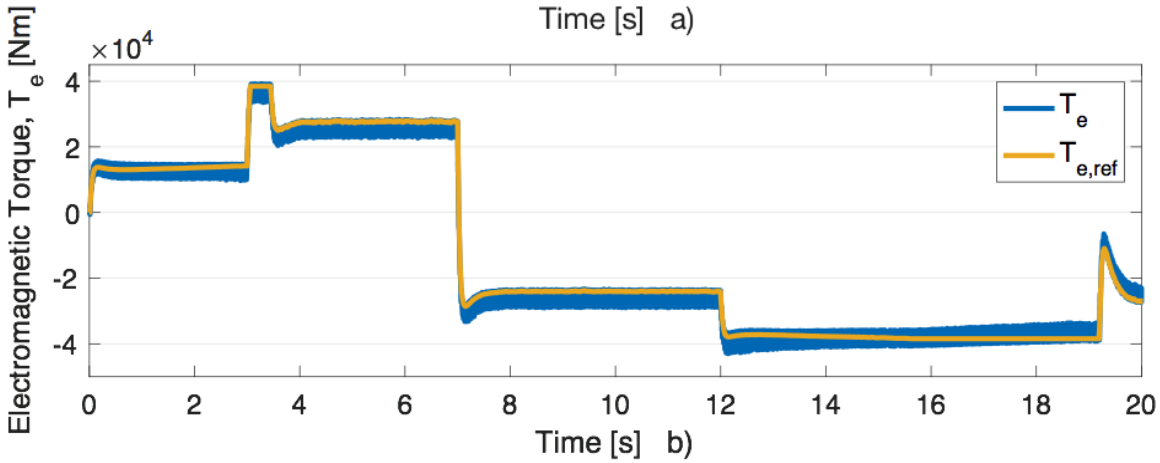
Electromagnetic Torque, T_e [Nm]
$\times 10^4$
4
2
0
-2
-4
0
2
4
6
8
10
12
14
16
18
20
Time [s] b)
T_e
$T_{e,ref}$

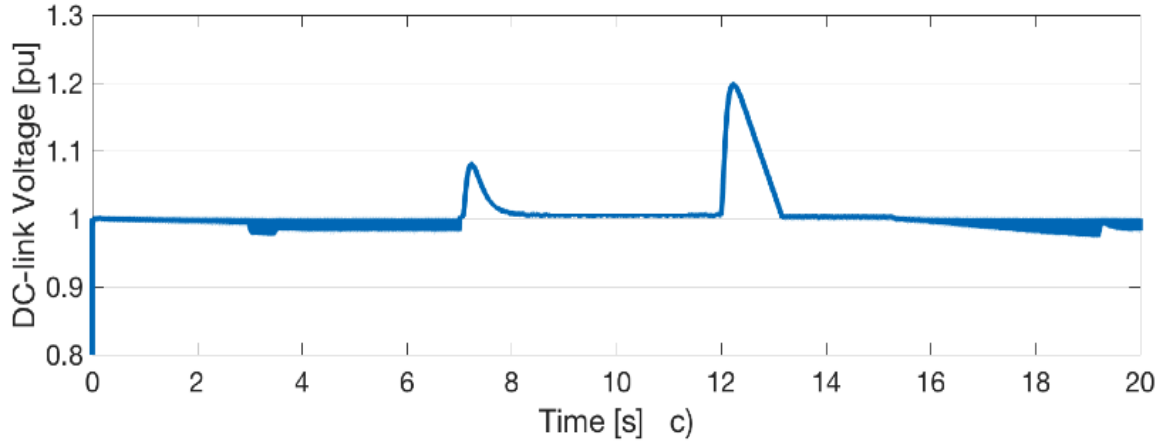
DC-link Voltage [pu]
1.3
1.2
1.1
1
0.9
0.8
0
2
4
6
8
10
12
14
16
18
20
Time [s] c)

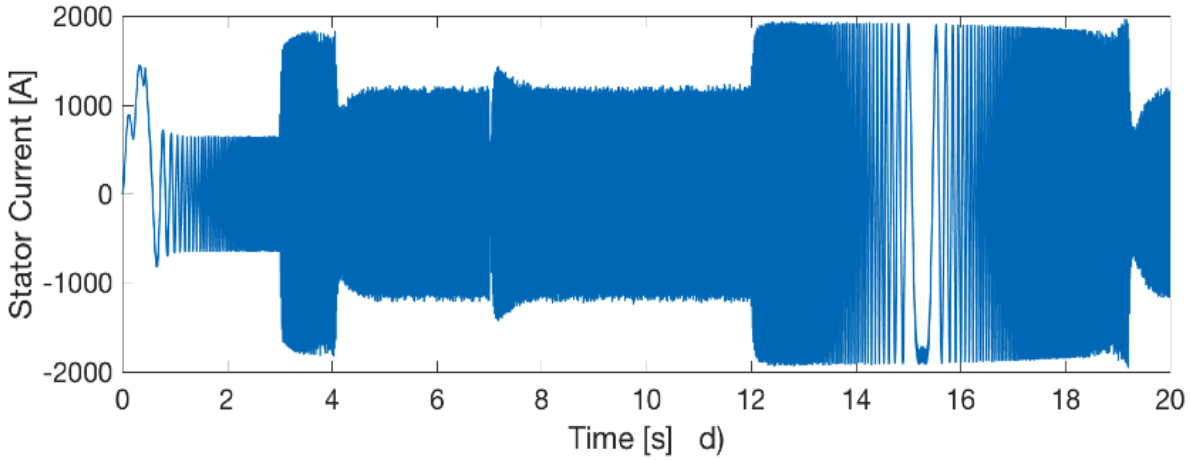
Stator Current [A]
2000
1000
0
-1000
-2000
0
2
4
6
8
10
12
14
16
18
20
Time [s] d)

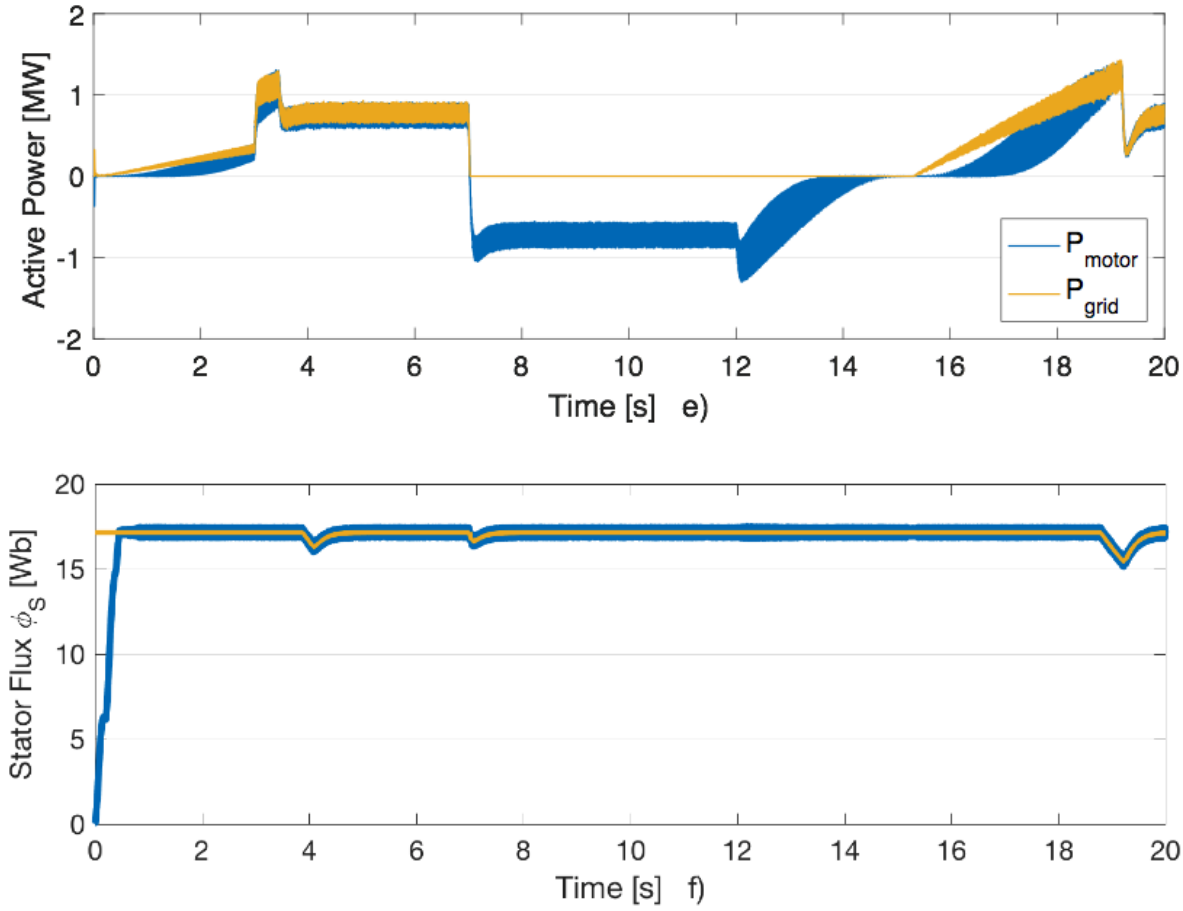

Figure 5.4. Simulations on Induction Motor Drive

nominal speed at time $t = 18.6s$, operating at rated power output with inverse torque and speed. Lastly, the stator flux is plotted in f). The flux is seen to stay stable at rated output throughout the simulations, with some overshoots for the times where the rotational speed goes above rated.

5.6. Offshore Oil & Gas Installation Microgrid Simulations

The offshore oil & gas installation microgrid as described in chapter 4 is modelled in Matlab/Simulink. The microgrid consists of a gas turbine coupled with a synchronous generator, an induction motor drive, and a passive resistive load. The parameters are specified in section 5.1, apart from platform load which are specified for each test case. Figure 5.1 in the chapter introduction shows the complete microgrid.

The microgrid is simulated for two test cases. The first is the system response to starting an induction motor drive. The second gives the response of losing load, both in form of passive load and motor load.

5.6.1. START OF INDUCTION MOTOR DRIVE

The start of an induction motor drive is simulated to test the response of the microgrid to a large change in motor load. The production unit is an aggregated gas turbine rated at $46MVA$, connected also to a passive load of $16MW$. One induction motor drive is included, rated at $8MVA$. Both production and passive load are connected at platform voltage of $11kV$, while the induction motor drive is transformed up from $6.6kV$. The duration of the simulation is set to 20 seconds, and the induction motor drive is introduced after $10s$.

Figure 5.5 shows the platform response to starting an induction motor drive. At time $t = 0$, the gas turbine is started and the system is observed to reach steady state after approximately 5 seconds. The system frequency stabilizes at $50Hz$. An initial frequency drop of $\sim 2.5\%$ is observed, well within the NORSOK limits. This can be seen in c). For this period, the active power production is seen to match the passive load perfectly, with only small oscillations. The reactive power is zero, and the platform voltage is seen to stabilize at rated value of $11kV$, after an initial overshoot of $\sim 12\%$.

At time $t = 10s$, the induction motor drive is connected to the microgrid, resulting in an immediate current and power spike as the machine reacts to the applied voltages and currents. The spike is limited by a varying resistor at the connection point for the first half second. As the motor drive accelerates, the power output is seen to increase, before stabilizing near $7MW$ as the motor reach rated speed. The output is seen to have huge oscillations. This is partly because of the high rotor speed, and partly because of a higher than ideal sampling time. Importantly, the generator is seen to immediately adapt to the added load and match the power consumption of both passive load and motor load. The system also starts producing reactive power to match the consumption of the motor drive seen in b).

The frequency again drops as load is added, and the gas turbine ups production. The drop is never more than 1%. The speed controller is seen to nicely balance the system after about 6 seconds. The platform voltage, seen in d), is largely unaffected by the added load, and stable at $11kV$. The reason for this is the gradual introduction of the load over the acceleration period. The motor drive voltage is seen to be fast to stabilize at the rated value of $6.6kV$.

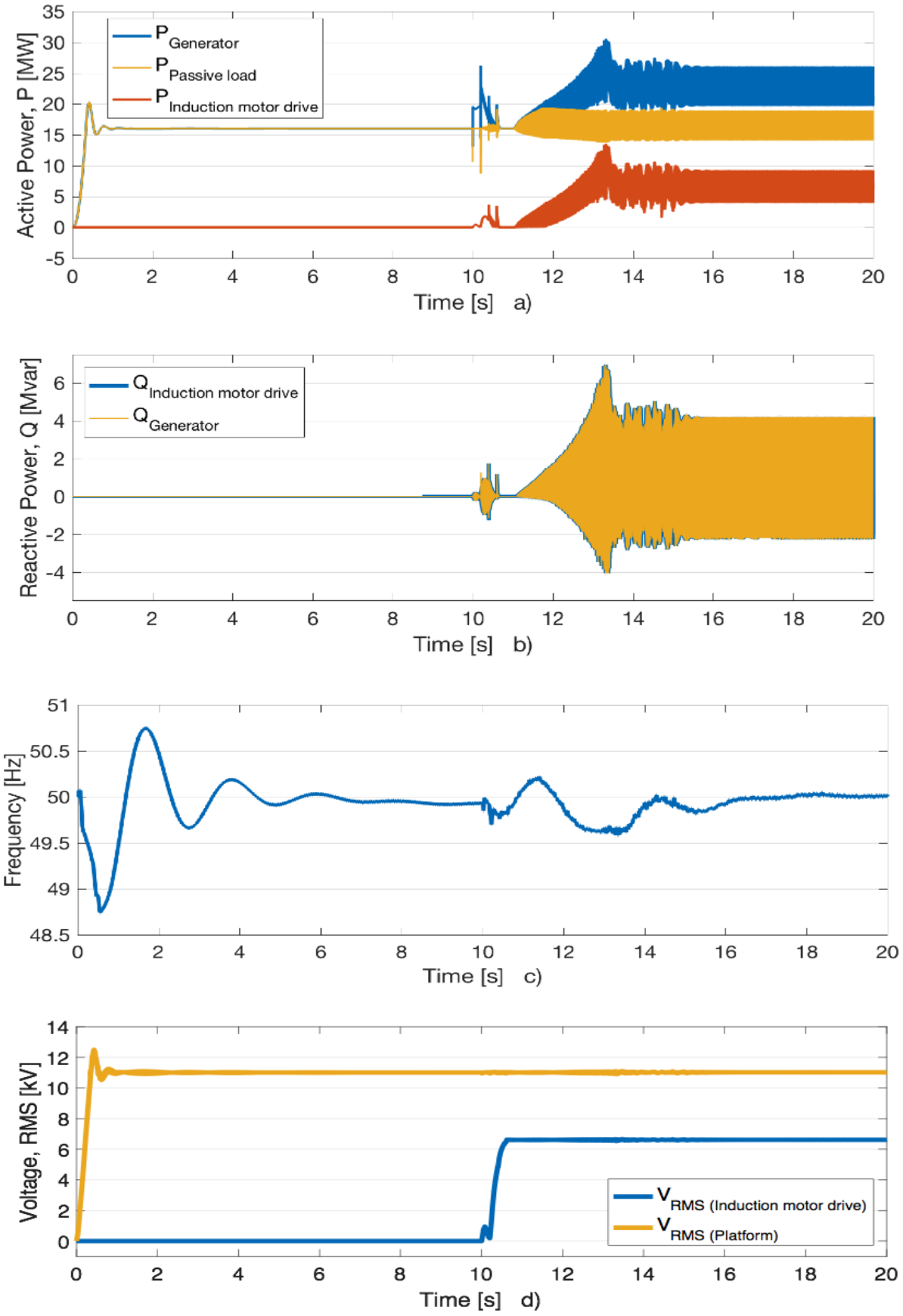

Figure 5.5. Simulation of Induction Motor Drive Start for Oil & Gas Offshore Installation; Platform Response

Figure 5.6 shows the induction motor drive's response at start-up. At time $t = 10$ seconds, the motor drive is connected to the grid. A spike in the stator current can be observed from a) to be only slightly above operating current due to the varying resistor included at start up. The rotational speed in b) is seen to nicely follow its reference.

The applied torque profile is shown in c), and is implemented according to equation (31) given in section 4.4. The electromagnetic torque is seen to follow the mechanical torque. As the machine accelerates, the electromagnetic torque is forced higher than the mechanical torque. The flux follows the reference, and stabilizes quickly at rated value. The DC-link voltage is observed in e) to rise to $1pu$, before stabilizing at $0.94pu$. The breaker here works to limit the voltage to below rated value.

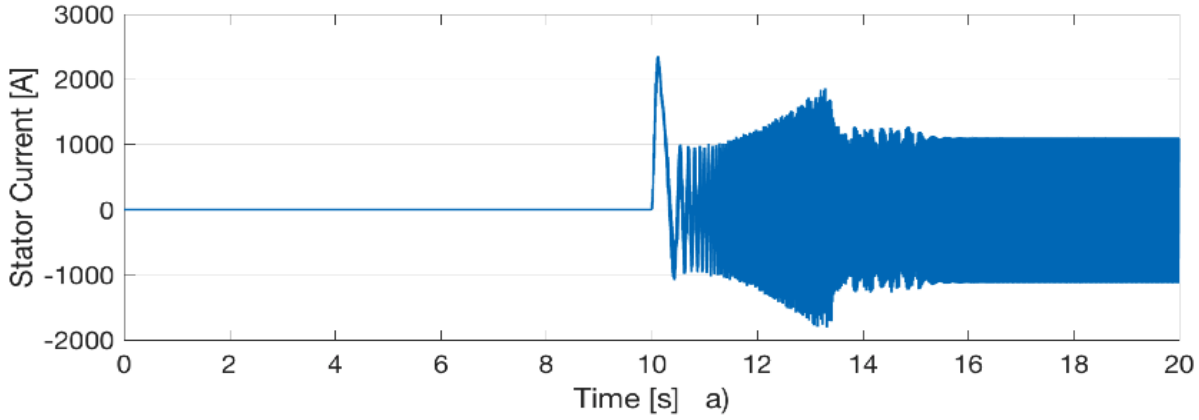

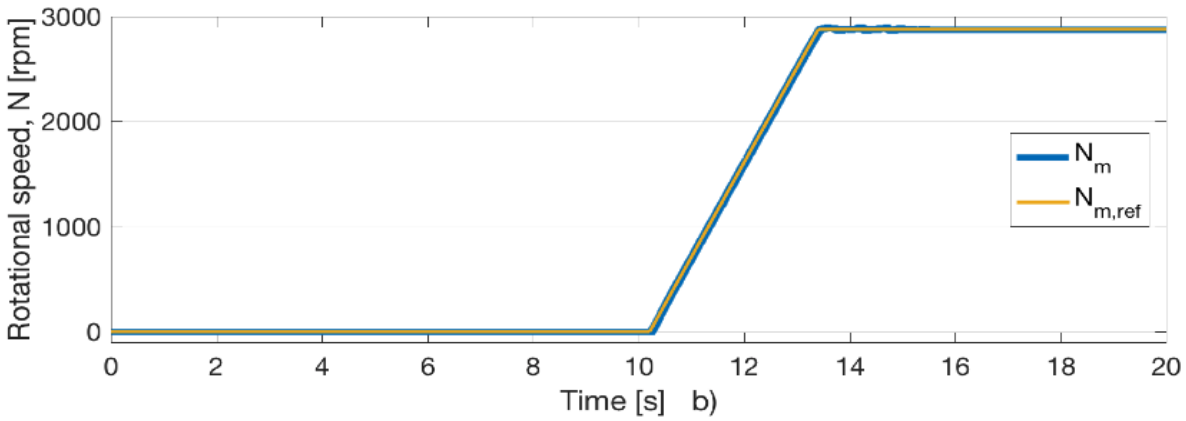

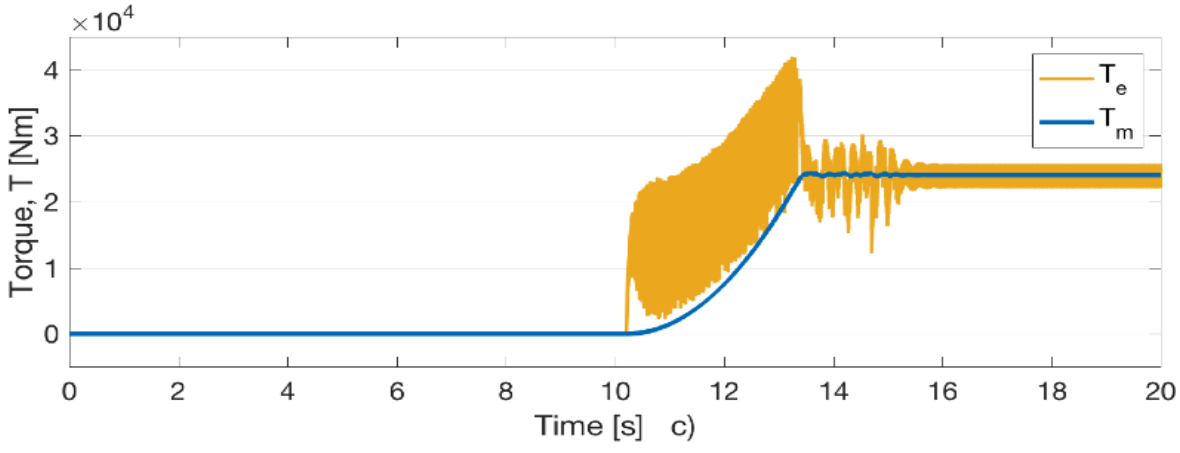

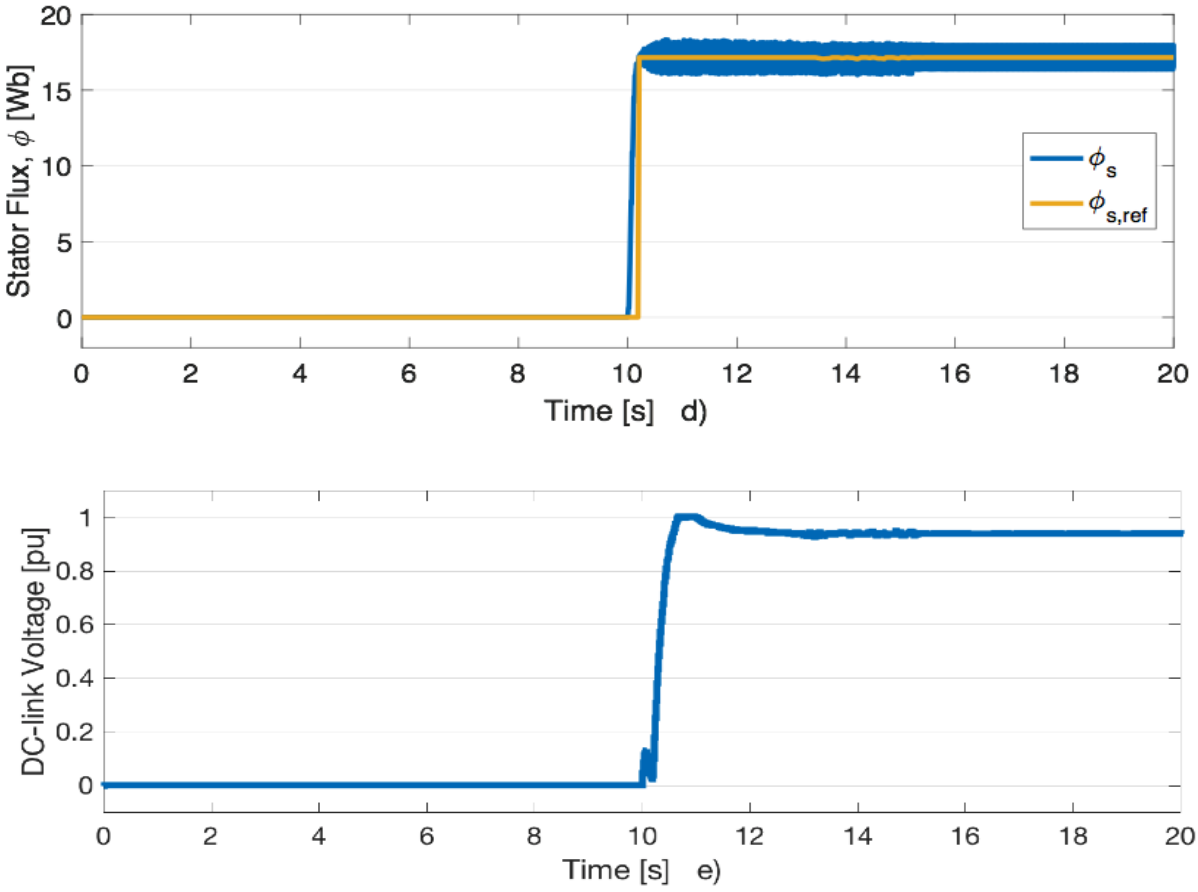

Figure 5.6. Simulation of Induction Motor Drive Start for Oil & Gas Offshore Installation; Motor Drive Response

5.6.2. Loss of Load

A simulation of a sudden load loss is simulated with focus on system response. The production unit is still an aggregated gas turbine rated at $46MVA$ connected to a passive load of $16MW$. For this case, two induction motor drives are included with an aggregated rating of $16MVA$. Both production and passive load are connected at the platform voltage of $11kV$, while the induction motor drives are transformed up from $6.6kV$. The duration of the simulation is set to 24 seconds. At time $t = 8s$, a passive load of $10MW$ is lost. At time $t = 16s$, additional load of one induction motor drive at $8MVA$ is also lost.

Figure 5.7 shows the platform response to sudden loss of loads. At time $t = 0$, the platform system is started with all units online. A sudden overshoot is observed in the active power, strongest for the generator unit. As the induction motor drives accelerate, the active power output increases, and the generator increases power production correspondingly. The oscillations also increase, and remain large. These high oscillations are partly caused by a high sampling time, and partly from the fast speed of the rotor. The reactive power is also seen to increase from b), and stabilize at $\sim 2Mvar$ with high oscillations. The speed controller of the

gas turbine is seen to stabilize the frequency near $50Hz$ after the initial inertial response to the system start-up with a drop of $\sim 3\%$. The voltages are also seen to stabilize at their rated rms-values in d) after the platform voltage initially experiences an upward spike $\sim 14\%$.

At time $t = 8s$, the platform experiences a loss of $10MW$ of passive load which corresponds to near a third of the total load. The system response is immediate, and the generator adapts fast to the new power output. The power consumption of the induction motor drives is seen to be unaffected by the change in passive load. The system frequency experiences an upward spike of $\sim 1.7\%$ as the power production suddenly exceeds the power consumption, before stabilizing after an inertial response 5 seconds later. The platform voltages are seen to have an overshoot of $\sim 8\%$ at the time of the loss, before stabilizing. This is all within the NORSOK limits.

At time $t = 16s$, the platform experiences an additional loss of one of the two $8MVA$ motor drives. This corresponds to just above one third of the remaining load. Again, the generator power is seen to quickly adapt to the new consumption. The oscillations are also seen to decrease somewhat, suggesting a reinforcing effect between the two motors. The reactive power generation is seen to be halved, as are the oscillations. The frequency again experiences an upward spike $\sim 1.1\%$, and again settles at rated value. The platform voltage is seen to overshoot $\sim 2\%$.

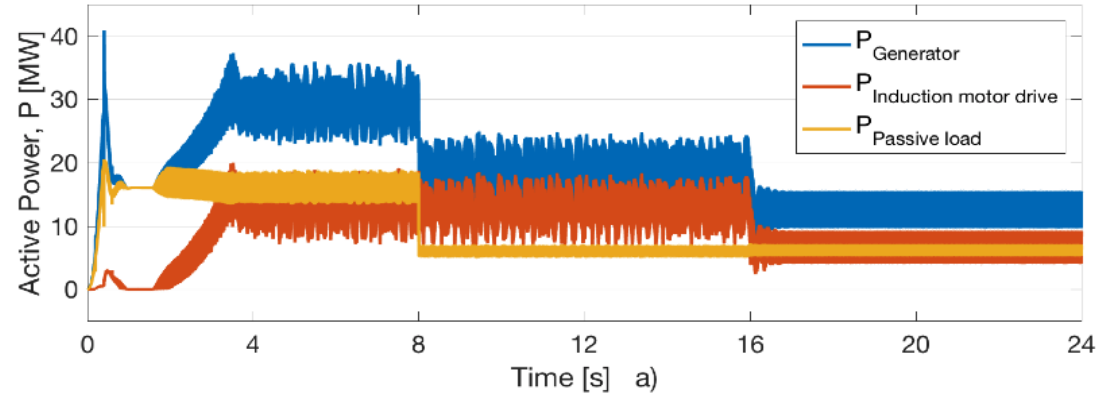

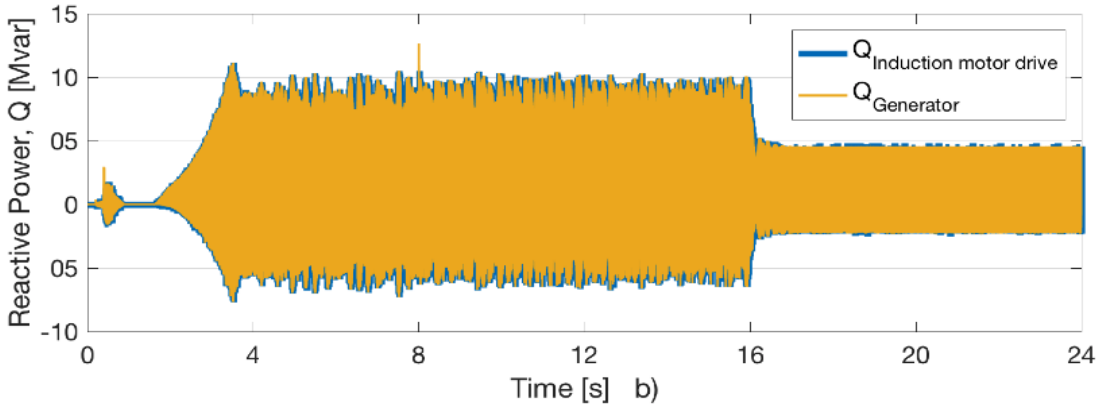

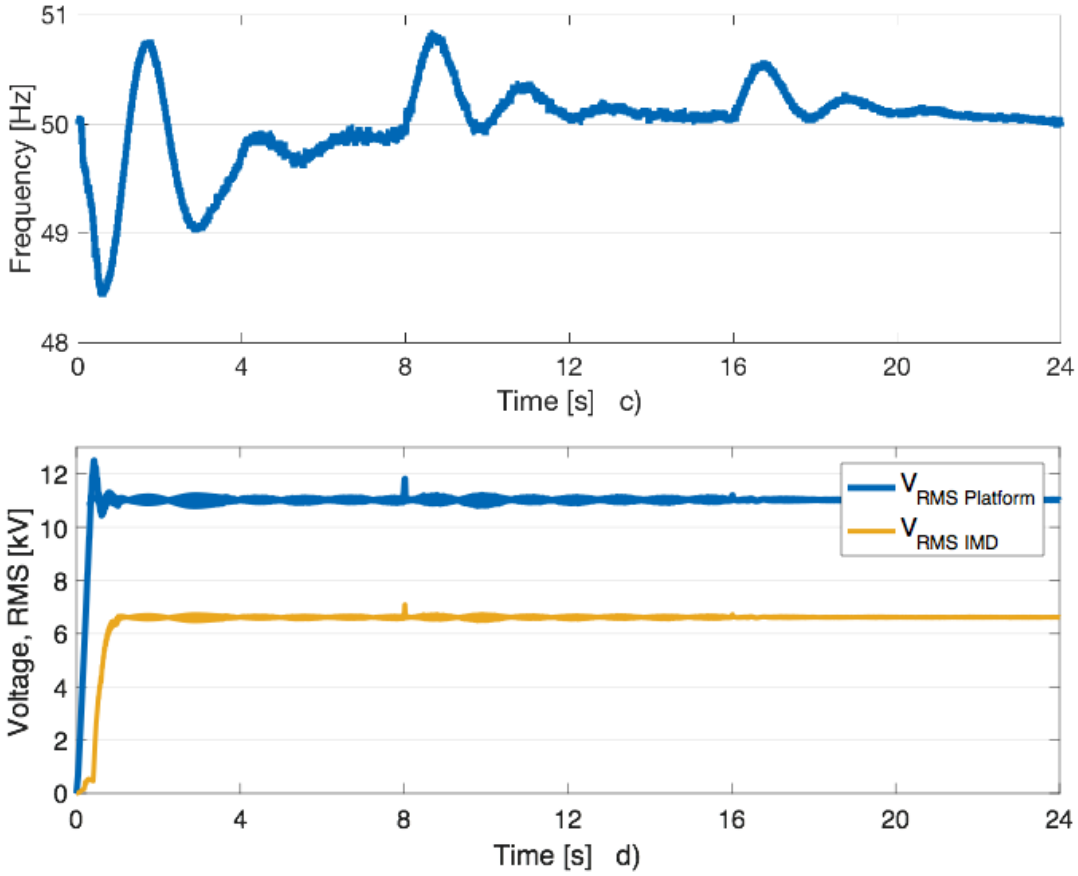

Figure 5.7. Simulation of Loss of Load for Oil & Gas Offshore Installation; Platform Response

Figure 5.8 shows some additional plots of the response to loss of load for specific units. In a) the stator current of the generation unit is seen to adjust for the change in load. As the voltage remain steady at rated value, the current is seen to control the power output. Similarly, the induction motor drive current is shown in b). After an initial spike at start-up, the current stabilizes before the motor is disconnected. This is seen as the amplitude drastically falls. Also, the frequency is seen to drop, suggesting the motor is deaccelerating as no power is delivered to the motor.

From c) it is seen how the loss of one motor reduces the oscillations in the electromagnetic torque, as also seen from the active power plots above. The torque of the disconnected motor goes to zero as the machine decelerates. The DC-link voltage of the induction motors is seen to remain below the limited value of $1pu$, and drop gradually for the disconnected machine as the motor stops.

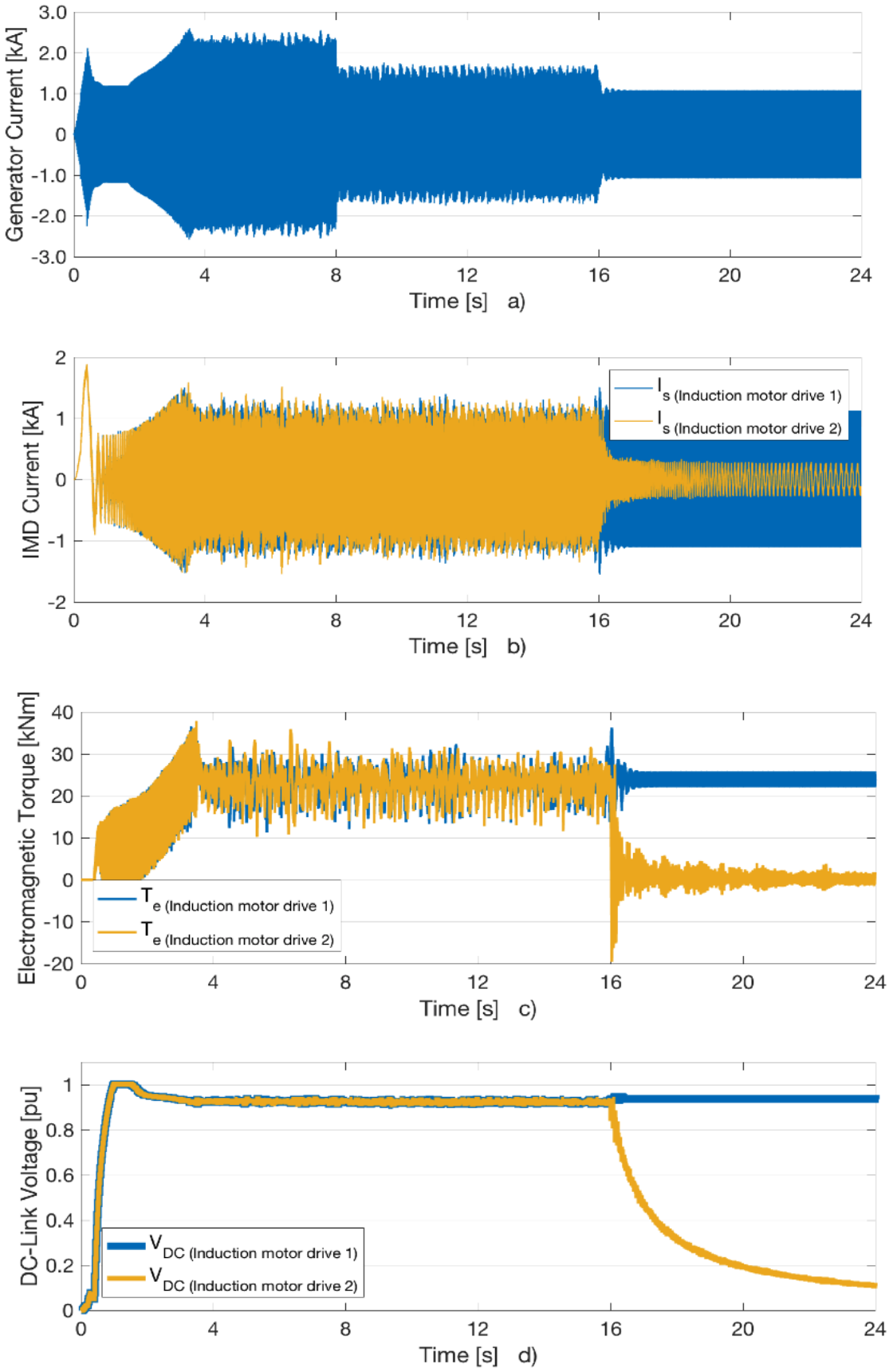

Figure 5.8. Simulation of Loss of Load for Oil & Gas Offshore Installation; Generator and Induction Motor Drive Response

5.7. DISCUSSION

An oil & gas electric platform microgrid has been implemented in Matlab/Simulink and simulated for two test case scenarios. In addition, both the gas turbine subsystem and the induction motor drive subsystem have been tested separately. The models include advanced control systems for speed control of the gas turbine and torque and flux control for the motor drive. The scenarios have been designed to test the correct behavior of the systems for different operating conditions and contingency events. This section will look more into the results obtained from the simulations in sections 5.4, 5.5 and 5.6. Extra focus will be on challenges encountered in the simulations and possible improvements of the model.

The first simulation case tests the gas turbine coupled with the synchronous generator. A speed controller is implemented to control the rotational speed and frequency of the system. A challenge with the speed control implementation is the reference being higher than the desired rotational speed. As the speed setting is controlled by the loading of the machine, more load gives a higher reference. A PI-controller is found difficult to implement because of this, as it relies on the error between the signal and reference to ideally be zero. The solution was to implement a rule-based stepwise controller instead. Different controller speed settings based on the error amplitude has proven to work good. However, some trouble stabilizing at the exact output are seen for slow oscillations where the controller moves faster than the speed. Further work should focus on improving the speed controller further. The test cases of adding and removing load prove the system works both fast and accurate to adapt to the new load. Substantial overshoots in voltage are seen at both start-up and for losing load, but the voltage is still well within the NORSOK transient limits. Similar for the frequency, which also holds within the NORSOK limits for drops and gains in load and at start-up. Important to notice is how the system always stabilizes, and maintains both rated voltage and frequency at steady state operation.

The second simulation case tests the induction motor drive with implemented direct torque control. High starting currents are an unwanted effect of starting an induction motor. The direct torque control does not directly limit these currents, as it controls torque directly and not indirectly through the currents. A combination of a soft starter and DTC is therefore needed. Due to the limited time of this thesis, this is not prioritized for this thesis, but a simple varying resistor is added to limit the starting current. This is by no means an ideal solution, but it is found to work adequately for this thesis by reducing starting currents to one third of the currents without the resistor. For further work, a more sophisticated soft starter device should be implemented. The test cases for the induction motor drive are chosen to demonstrate the different operating modes and performance of the direct torque control. Although operation as a generator would be unlikely, it demonstrates the agility of the control method. The method is also seen to give excellent performance for low speeds and zero speed crossings, where other control methods yield poorer results. Important to notice is the fast response the torque control gives, which is many times faster than indirect current control. The speed

controller is seen to give a fast response with little deviations for changing torques. As full load torque is applied, the electric torque is seen to be forced to rise to maintain machine acceleration. This is given by equation (41). The electric torque is limited to avoid to large currents. Overshoots in the DC-voltage is observed for when the load torque and speed reference are inverted. This is unwanted, but of importance is that both these events are unlikely to happen during actual operation. The voltage is seen limited for both acceleration, loading and steady state operation. The braking resistor is also seen to burn the excess power shortly after.

The third simulation test case implements the complete oil & gas electric system, with the gas turbine model, the induction motor drives and the passive load. Two test cases are performed on the system.

The first case tests the response to the starting of an induction motor drive. Again, the biggest deviations in voltage and frequency are found at system start-up. The voltage remained steady for the introduction of the motor drive. This is because of the gradual acceleration of the drive adding the load torque gradually. This is one advantage of using motor drives with speed control. The specific motor drive plots point to the drive working good, with the system following the speed reference. The electric torque is again higher than the load torque during acceleration, and has substantially larger oscillations. This is partly caused by the fast speed of the rotor, and partly from a higher than ideal sampling time as discussed further below. The DC-voltage is seen to stabilize below the rated DC-value for the simulations after being limited to rated value as the machine accelerates. The brake only limits voltages above this value, and does not control the voltage for lower values. Important to notice is how the voltage is seen to stabilize for steady state operation.

The second case tests the response of the system to losing passive load, and then one induction motor drive. The passive load loss is 25% bigger than the induction motor drive loss, but has a substantial bigger effect on platform voltage at the time of loss. The main reason for this has to do with the reactive power consumption of the motor drive. At the loss of the motor drive, the reactive power consumption decreases and leads to a drop in platform voltage. This is the opposite effect of losing load, which causes voltage overshoots. The effect of losing a motor drive is therefore countered by the decrease in reactive power consumption. As the passive load is modelled purely resistive, this effect is not seen there, and the voltage overshoots are found to be bigger. The motor drive oscillations are seen to drastically increase for two machines, suggesting a reinforcing effect. As too high oscillations are unwanted, this effect should be investigated further. The machine losing connection to the grid is seen to gradually slow down without any big current spikes or similar. This suggests the event would do little damage on machine and the platform system.

The frequency and voltage deviations never exceeded the NORSOK transient limits for any of the test cases of this chapter. Some tests exceeded the steady state limits, but as start-up, and adding and losing load must be considered transient events the conclusion is that the system kept within the required boundaries. Tests with bigger losses or additions of load could

yield different results, and is therefore suggested investigated further. The fast response of the gas turbine model is also questioned whether to be realistic behavior for real life operation. The fact that the required speed reference adjustments are small ($< 2\%$) suggests small adjustments can handle big transients. Other models might behave differently, which would affect the results obtained in this thesis. This is suggested to be investigated further.

The simulations were found to be really time consuming, using near 30 minutes per simulated second. Given the amount of simulations in the thesis and the limited time frame of the thesis, the sampling time was therefore put at a higher level than ideal. This is seen in the outputs of active and reactive power throughout the simulations. The outputs are seen to have large oscillations, not ideal for simulation purposes. Further work should seek to redo some of the simulations at a lower sample time to verify the results of this thesis.

6. System 3: Wind Integrated Oil & Gas Offshore Installation Simulations

The following chapter will focus on simulations of a wind integrated oil & gas installation microgrid, referred to as system 3. This is the complete system, and the system complying with the problem description of this thesis. The goal of the chapter is to test the system at normal operation, and test for a number of contingency events. The results will be compared to the NORSOK limits given in section 5.2, to check whether the wind integrated system operates safely within the legal requirements. Figure 6.2 shows a schematic of the complete simulated system.

No offshore oil & gas installation is today powered directly by offshore wind energy. However, several studies have been conducted on the matter, and ongoing testing of offshore wind power points to it being possible in near future. For a more detailed description of the state of the art within offshore oil & gas platform wind power integration, see [8].

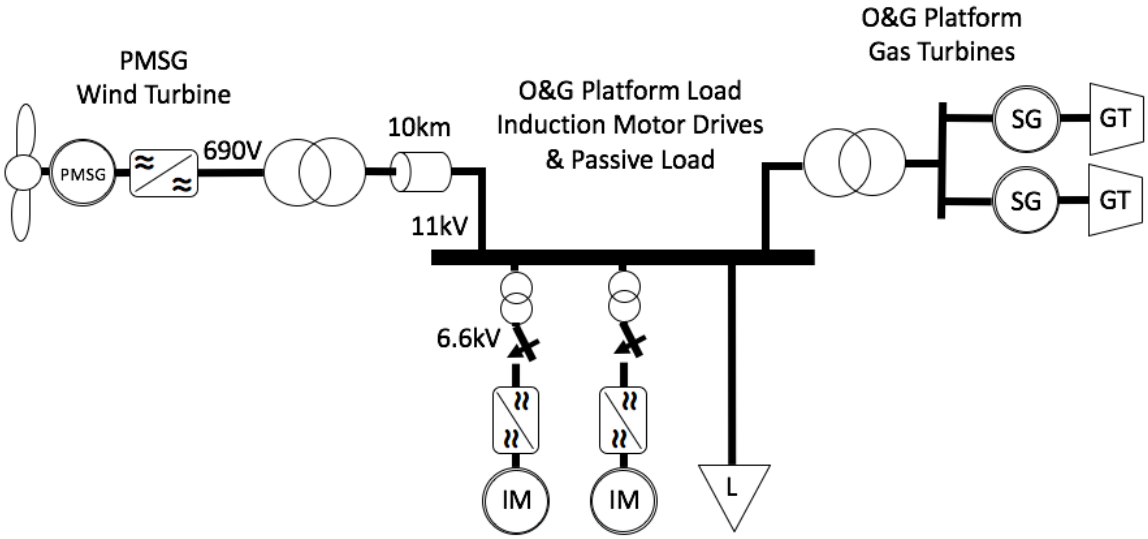

Figure 6.1. Wind Integrated Oil & Gas Platform Microgrid

The chapter is organized in six subsections. Section 6.1 gives a summary of the results obtained by simulation in this thesis. Section 6.2 presents the theoretical basis of the AC transmission line used to connect the wind energy system to the oil and gas platform. The section also includes the line parameters. Section 6.3 describes the model implementation in Matlab/Simulink. The first test case is found in section 6.4, and gives the system response to the wind power integration for a varying wind speed wind profile. Section 6.5 presents the main simulations of the thesis, with a number of contingency effects tested on the system. Finally, section 0 discusses the results of the simulations.

6.1. SUMMARY OF SIMULATION RESULTS

The results of the simulations of this chapter is summarized in table 6.1. For convenience, table 5.5 is a reprint of the NORSOK requirements found in section 5.2. For a closer look at the simulations with plots and comments, see sections 6.4 and 6.5. As seen from the table, the platform voltage and frequency are seen to remain within the NORSOK limits for all tested contingency events.

(Table 5.5. NORSOK Limits for Offshore AC Distribution Systems)

	Voltage (pu)	**Frequency (pu)**
Stationary Limits	0.90 – 1.06	0.95 – 1.05
Transient Limits	0.80 – 1.20	0.90 – 1.10

Table 6.1. Summary of Simulated Contingency Effects on a Wind Integrated Oil & Gas Offshore Installation

	Voltage (pu)	**Frequency (pu)**
6.4 Normal Operation	*0.94 – 1.15*	*0.96 – 1.025*
6.5.1 System start	*0.97 – 1.13*	*0.985 – 1.014*
6.5.1 Start of IMD	*~1.0*	*0.994 – 1.004*
6.5.2 Loss of motor load	*1.0 – 1.036*	*0.995 – 1.012*
6.5.3 Loss of Passive Load	*1.0 – 1.09*	*0.99 – 1.014*
6.5.3 Loss of Wind Power	*0.99 – 1.0*	*0.995 – 1.005*
6.5.4 Loss of Gas Turbine	*~1.0*	*0.975 – 1.025*

6.2. AC TRANSMISSION LINE

Offshore oil & gas installations have limited platform space, usually already utilized by existing equipment. The integration of offshore wind power production to the platform grid will require space for integrating related equipment. Big transformer units would probably not fit on existing platforms and might require an additional platform construction. In addition, wind turbines would need to be placed some distance from the platforms to avoid disturbances as the wind passes the platform. This suggests the need for power transmission lines modelled for this thesis.

For transmission of power less than $80km$, and at voltages less than $69kV$, the short line model is the popular choice for representing transmission line behavior [55, 56]. The power transmission between the oil platform and the wind energy system of this thesis is within these boundaries, and the short line model is therefore used.

The short line model represents the transmission line as a series impedance branch. Since the line is short, the capacitance can be neglected without much error. The resulting line is modelled as a resistance in series with an inductance. The resulting impedance Z_{line} is given as:

$$Z_{line} = (r + j\omega L)l \tag{50}$$

where r is the resistance given in ohms per kilometer, ω is the electric frequency in radians per second, L is the inductance given in henrys per kilometer, and l is the line's length in kilometers.

The active and reactive losses of the line is given by the square of the phase current i as:

$$P_{line} = (r * i^2)l \tag{51}$$

$$Q_{line} = (\omega L * i^2)l \tag{52}$$

A high transmission voltage is therefore advantageous as it lowers the current and thereby the losses of the line.

Table 6.2 gives the parameters of the transmission line based on [55].

Table 6.2. AC Transmission Line Parameters

Parameter	*Value*
Resistance *(r)*	0.15Ω/km
Inductance *(L)*	1.3263H/km
Length *(l)*	10km

6.3. Model Implementation of Wind Integrated Oil & Gas Offshore Installation

The wind integrated oil & gas platform microgrid is modelled and implemented in Matlab/Simulink. For specifics on the wind energy system model implementation, see section 3.3, and for specifics on the oil & gas platform implementation, see section 5.3. The complete integrated microgrid also includes a power line connecting the PMSG wind system to the oil & gas platform. The line is modelled as a built-in series RL-branch, based on the relations and parameters given in section 6.1. The line has a transformer on each side, modeled by the built-in three-phase transformer block with two windings. The transformer is implemented as ideal.

Three adaptions have been made from the simulations on the separate subsystems in chapters 3 and 5. The first is the inertia value of the PMSG wind system. A direct-driven large generator with slow rotational speed needs a huge inertia, typically in the range of several hundred thousand to millions, to achieve the same inertia constant as a fast rotating generator. This caused problems when integrating the wind turbine with the oil & gas platform, as the wind system became unstable and would not settle because of the inertia. The wind system inertia is therefore reduced to $5341 kgm^2$ for the simulations of this chapter, giving good results.

The second adaption is the use of a higher sampling time and shorter duration simulations. The complete model has many different subsystems working together, each being complex and demanding on a computational level. A reason for this is the use of switching devices in the PMSG and motor drive systems combined with a high sampling time. A lower sampling time reduces the oscillations, but also increases the simulation time. The resulting sampling time has therefore been set weighing the two considerations to be able to complete the planned simulations.

The last adaption was setting the switching frequency to $5kHz$. This was done to speed up the simulations, and is expected to increase the system oscillations.

6.4. System Response to Normal Wind Operation

The wind integrated oil & gas installation microgrid is simulated at normal wind speed operation to verify the integrated system is working. Figure 6.1 depicts he full microgrid, which consists of an aggregated gas turbine rated at $46MVA$, a wind turbine rated at $6MW$, a passive load of $16MW$, and two induction motor drives rated at $8MVA$ each. Both production and passive load are connected at the platform voltage rated at $11kV$, while the induction motor drives are transformed up from $6.6kV$. The PMSG wind turbine is rated at $0.69kV$, where the power is transferred by transmission line at $33kV$ to the platform and transformed down again to rated platform voltage. The duration of the simulation is set to 20 seconds, and all units are started at time $t = 0$, with the wind speed being the only varying parameter.

The wind profile of section 3.1 is reused for the simulation. A shorter time interval is found adequate for testing, as operation at wind speeds above rated speed should have little effect on the system as the pitch angle controller limits power output. This is proven to work correctly in section 3.4. This will also be verified as the simulations end above rated speed. The period from $10s < t < 30s$ of the earlier wind profile is therefore chosen. Figure 6.2 demonstrates the applied wind profile. The simulations are seen to start at wind speed $8.2m/s$, and fast increase to rated speed of $12m/s$. The system operates at rated speed for some time before experiencing a gust in form of a sudden drop in wind speed, and then increasing again to end slightly above rated speed.

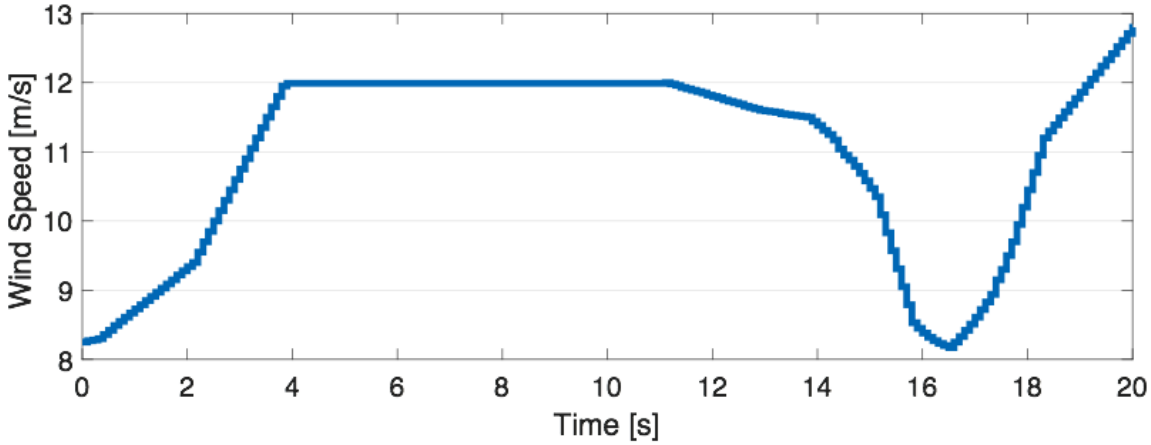

Figure 6.2. Wind Speed Profile for Full Wind Integrated Oil & Gas Microgrid Simulations

Figure 6.3 demonstrates the platform response to the integration of a wind energy system at varying wind speeds. At start-up, the gas turbine active power in a) is seen to experience a power spike to $40MW$ due to inertia as it starts at a high load. This is however well below the generator rating of $46MW$. The gas turbine active power proceeds to increase in accordance with the acceleration of the motor drives, seen to adapt to the increasing wind power production. The wind power output increases with wind speed as expected, and stabilizes at rated speed with the rest of the system at time $t = 4s$. At $t = 12s$, the wind speed starts to drop, and the gas turbine is seen to adapt to the wind active power output. No effect is observed for the load, which remains steady.

The system reactive power is seen in b) and is near zero at start-up. As the motor drive accelerates, its reactive power consumption also increases. The gas turbine reactive power production is seen to be slightly higher than the motor drive consumption. This is due to the small reactive power consumption of the wind system's transmission cable. As the wind speed drops, the gas turbine increases production again to match the consumption. The active and reactive power outputs are seen to have large oscillations, which is discussed more in section 6.3.

The platform frequency is seen in c). The frequency is seen to experience some oscillations at start-up due to the gas turbine inertia, but stabilizes near $50Hz$ after $\sim 5s$. As the wind turbine increases its power output, the gas turbine must decrease correspondingly. This is seen as the frequency drops, interpreted the same as adding additional load on the gas turbine. The biggest frequency drop is measured to 4%, well within the NORSOK limits given in section 5.2. The rms voltages in d) is seen to quickly stabilize at their respective rated values. A short voltage spike is observed in the platform voltage at start-up, measured to 15%, which is within the NORSOK transient limits. Start-up at full load is also a rare event, meaning the platform response is considered good. The oscillations in the rms voltage are also seen to be larger for fast changes in wind speed.

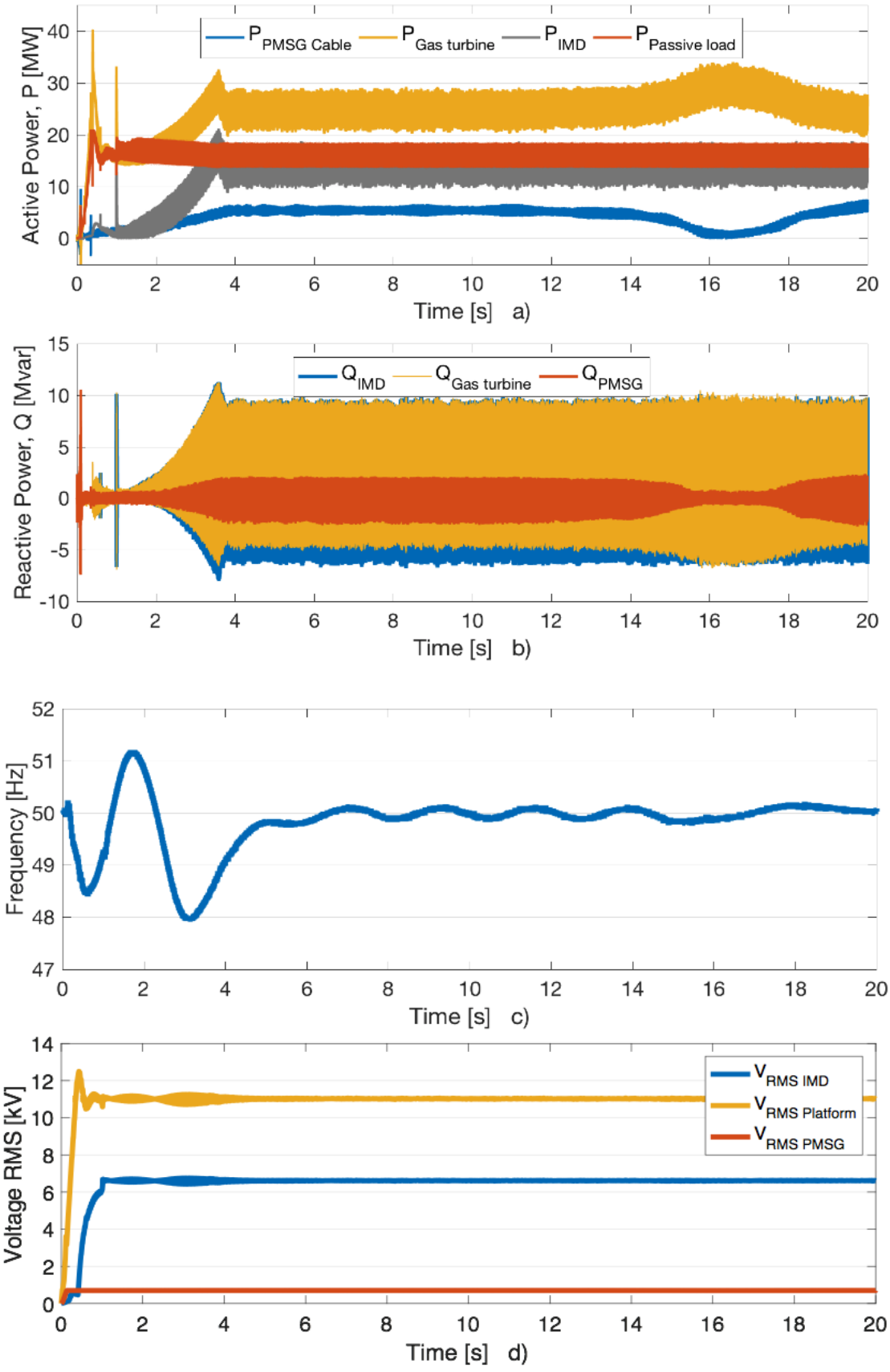

Figure 6.3. Simulation of Full Wind Integrated Oil & Gas Platform Microgrid; Platform Response

Figure 6.4 demonstrates the wind system response to integration to an isolated oil & gas microgrid for varying wind speeds. At start-up, the system sees initial spikes due to starting above the cut-in speed. The DC-voltage in a) is seen to immediately stabilize at $1pu$, as correctly dictated by the control system. The rotational speed is also seen to follow the reference correctly and fast. The speed is observed to be limited to $1pu$, even as the wind speed goes above rated value at time $t = 19s$.

The controlled dq-currents on the generator and system sides are seen in plot c) and d) respectively. All currents are seen to follow their references both correct and fast. Compared to the simulations on system 1 alone, as seen in section 3.4, the results are very similar. The fully integrated system has somewhat larger oscillations, but the general response of the system is recognizable. This proves the system largely works as supposed.

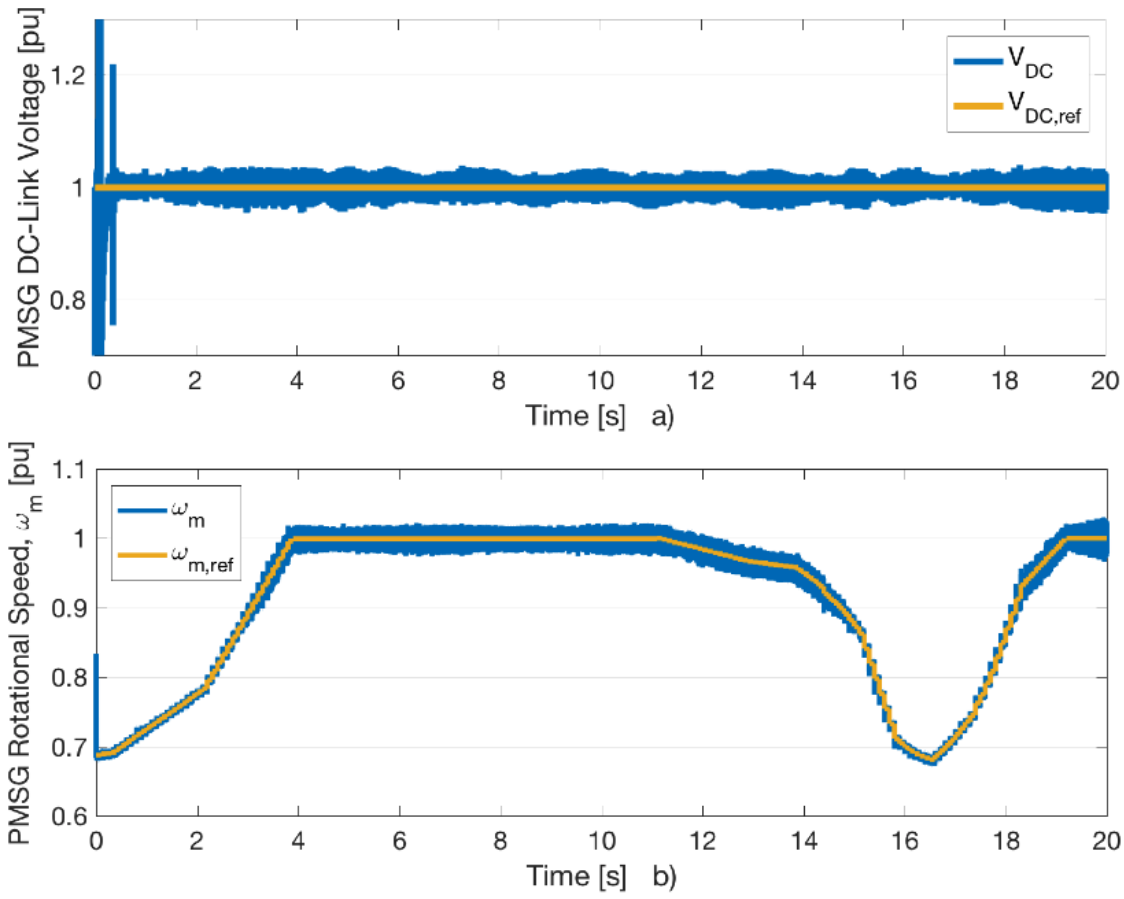

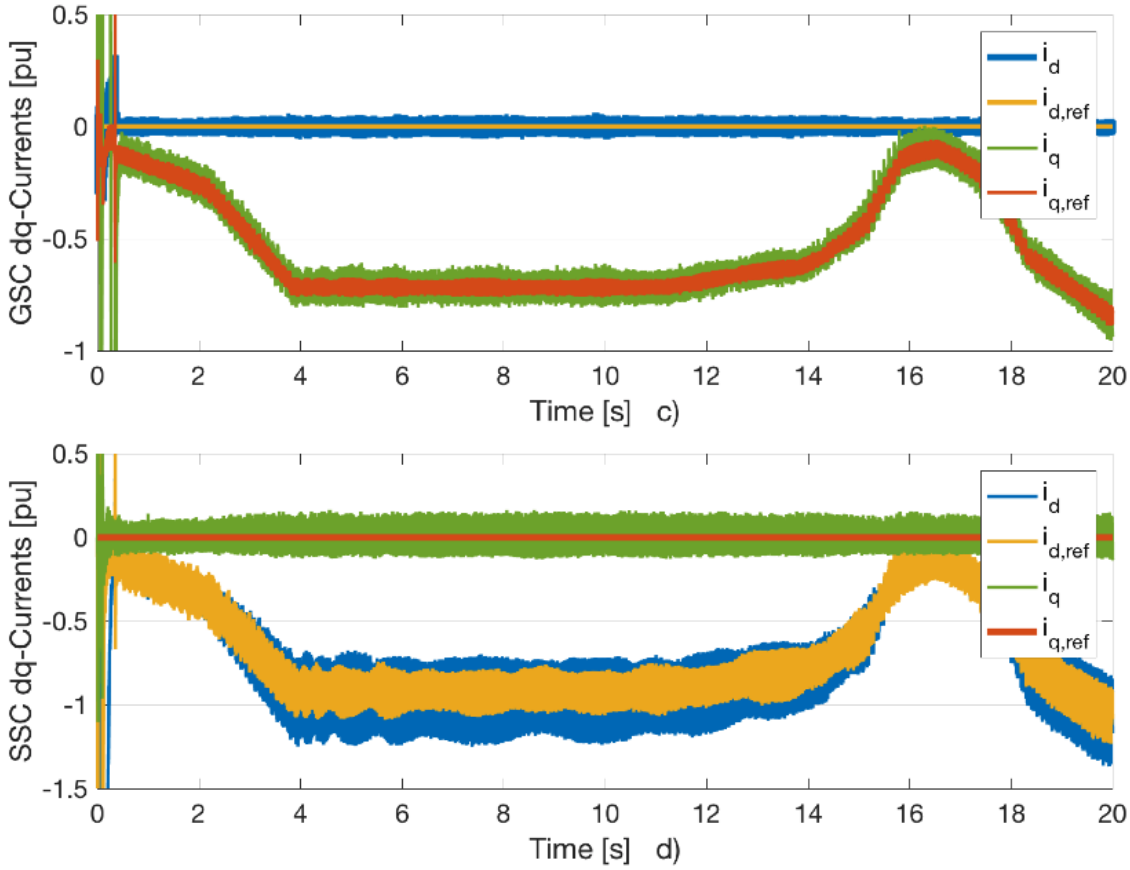

Figure 6.4. Simulation of Full Wind Integrated Oil & Gas Platform Microgrid; Wind System Response

6.5. CONTINGENCY EFFECTS

Figure 6.1 depicts the complete offshore wind integrated oil & gas installation microgrid applied in the simulations. This section will simulate the system, and observe the response of a number of contingency events. The parameters are specified in sections 3.2, 5.1 and 6.1. As mentioned in section 6.3, the PMSG inertia is set significantly lower than rated value, now at $5341kgm^2$. Other deviations will be specified in the specific test cases below.

The wind integrated microgrid is simulated for four test cases, and compared against the requirements presented in the NORSOK E-001 standard for offshore AC-distribution systems found in section 5.2. The first case tests the response of a black start of the system and the starting of an induction motor drive. Although this may not be a contingency event, considered a normal part of operation, it is included to ensure the system still operates within the required boundaries. The second and third case tests the response of losing load, first motor load in form of an induction motor drive, and then passive load. The fourth and fifth case tests the response to losing all wind power, and losing one gas turbine.

6.5.1. System Start with Passive Load & Start of Induction Motor Drive

The start of the integrated system with passive load is simulated, before adding additional load of starting an induction motor drive (IMD). The simulations are aimed at testing the response of the wind integrated microgrid to a large addition of motor load. The production units are an aggregated gas turbine rated at $46MVA$ and a wind turbine rated at $6MW$. Both are initially connected to a passive load of $16MW$. One induction motor drive is started, rated at $8MVA$. Both production and passive load are connected at platform voltage of $11kV$, while the induction motor drive is transformed up from $6.6kV$. The wind system is rated at $690V$. The wind system is connected to the platform through a power line rated at $33kV$.

The duration of the simulation is set to 15 seconds. The system is initialized with all production units and passive load going online at $t = 0$. The induction motor drive is introduced after $8s$. The start of the induction motor drive is simulated by a breaker closing at the introduction time, adding the motor drive to the grid. The addition corresponds to a 50% increase in load. An $8MVA$ motor is considered the upper end of available motor sizes, and will give a good picture on the platform's ability to handle motor starts also for smaller machines.

Figure 6.5 shows the effect of adding load to the platform system. At time $t = 0$, the gas turbine generator, the wind turbine generator and the passive load goes online. The gas turbine and wind turbine are both initialized at rated speed. The active power response is shown in a). As the PMSG immediately increases towards rated value, the gas turbine inertia absorbs the excess power in what is seen as a small power dip. As the passive load starts to draw power, a power spike is observed, however still within the generator's rating. The gas turbine is seen to always adapt to maintain power balance, allowing the wind system to produce at maximum capacity. The active power is seen to stabilize after $\sim 0.75s$. The induction motor drive is connected to the microgrid at $t = 8s$. Some power spikes are observed during the first second, caused by high currents as the induction motor is excited as voltages and currents are applied to the stator windings. A variable resistor is connected in series at start-up to limit the currents, being step-wise reduced before switching out after 1s. Again, the gas turbine power output is seen to adjust to handle the increasing load. No noticeable effect is seen on the PMSG power output, which continues at full capacity. The oscillations are seen to increase at the introduction of the motor drive, discussed more in section 6.3. As the motor drive stabilizes at rated speed after the acceleration, the system power output is seen to stabilize as well.

The system reactive power is shown in b). The gas turbine is seen to immediately weigh up for the reactive power consumption of the PMSG transmission line. This includes the spike at initialization. The resistive load has no reactive power consumption, and is not included in the plot. The acceleration of the induction motor drive is seen to increase the reactive power consumption of the system. The gas turbine is seen to handle the increased consumption effortlessly.

The platform frequency and rms voltage is seen in c) and d) respectively. The initialization of the system with passive load is seen to cause a dip in frequency as consumption is increasing before the production follows. The gas turbine speed controller is seen to adjust as the turbine inertial response subsides, steadying the frequency at $50Hz$. The frequency never deviates more than 1.5% from rated value, well within the NORSOK limits. The start of the induction motor drive is seen to cause another frequency dip. This is smaller as the induction motor drive is rated only half of the passive load, and well within the NORSOK limits. The platform voltage is seen to experience a spike at start-up. The deviation is seen to be $\sim 13\%$, which is within the NORSOK transient limits. At motor drive start-up, no major change is observed as the motor drive speed control introduces the load more gradually than a full torque start.

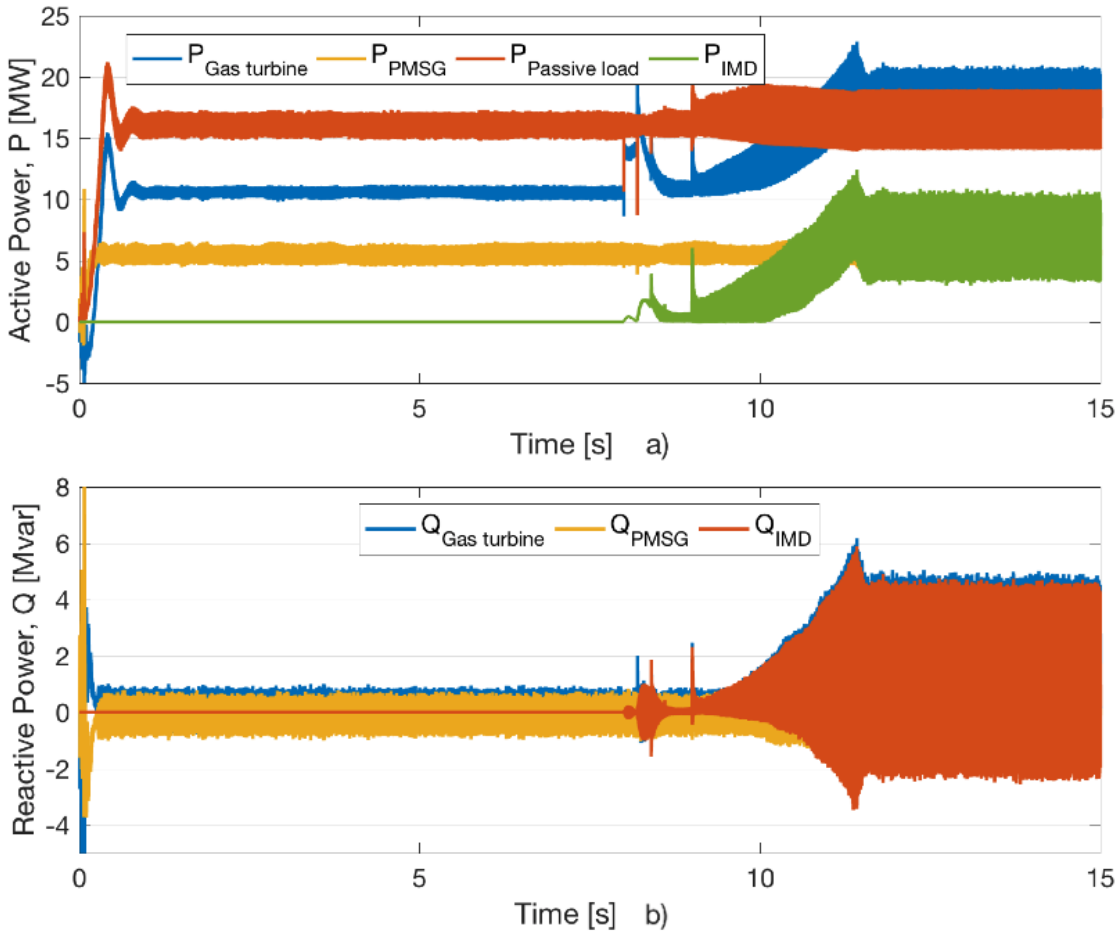

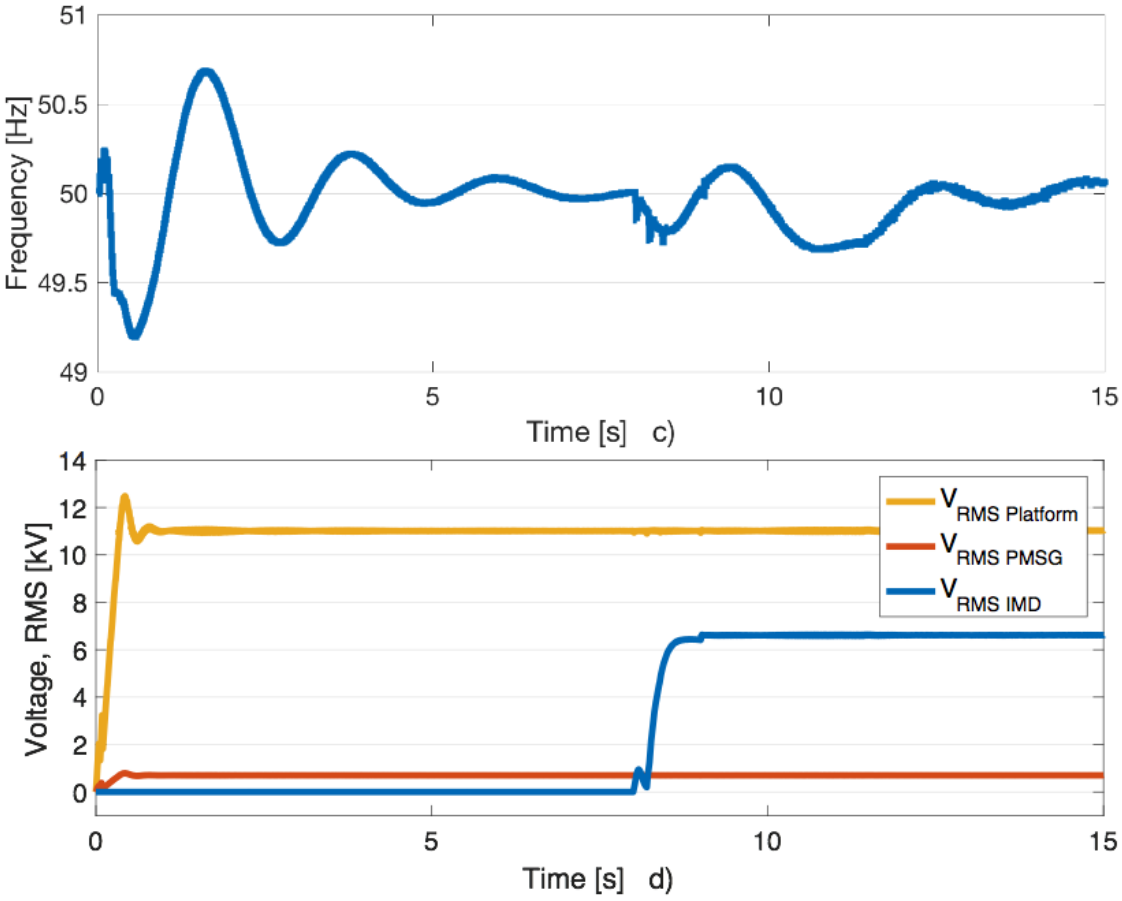

Figure 6.5. Contingency Effects on Full Wind Integrated Oil & Gas Platform Microgrid; Start of Induction Motor Drive

6.5.2. Loss of Motor Load

The sudden loss of a motor load is simulated, with the aim of verifying that operation is maintained within the NORSOK limits. The production unit is an aggregated gas turbine rated at $46MVA$ connected to a passive load of $16MW$. The wind system is rated at $6MW$, and the induction motor drive is rated at $8MVA$. Both production and passive load are connected at the platform voltage of $11kV$, while the induction motor drive (IMD) is transformed up from $6.6kV$, and the wind system is rated at $0.69kV$. The wind system is connected to the platform through a power line rated at $33kV$.

The duration of the simulation is set to 14 seconds, and the induction motor drive is lost at $t = 4s$. The system is initialized at rated output at $t = 0$. The loss is simulated by a breaker opening at the loss time, disconnecting the motor drive from the platform. The loss corresponds to 17.4% of the rated gas turbine power. An $8MVA$ motor is considered the upper end of available motor sizes, and will give a good picture on the platform's ability to handle motor losses also for smaller machines.

Figure 6.6 shows the effect of a sudden loss of motor load on the platform electric system. The active power can be seen in a). The active power of the induction motor drive drops immediately to zero as the load is lost. The gas turbine power drops correspondingly, while the wind system power remains unaffected at rated output. The oscillations are also seen to drastically decrease, as discussed more in section 6.3. Similarly, the reactive power seen in b) drops, and only the wind power transmission line consumes any reactive power.

The frequency and rms voltages can be seen in c) and d) respectively. The loss of load causes a sudden spike in frequency as the production is suddenly higher than the consumption. The deviation is however never more than 1.2%, well within the NORSOK limits, and stabilizes after $\sim 6s$. A small voltage spike of $\sim 3.6\%$ is observed in the platform voltage, also well within the NORSOK limits.

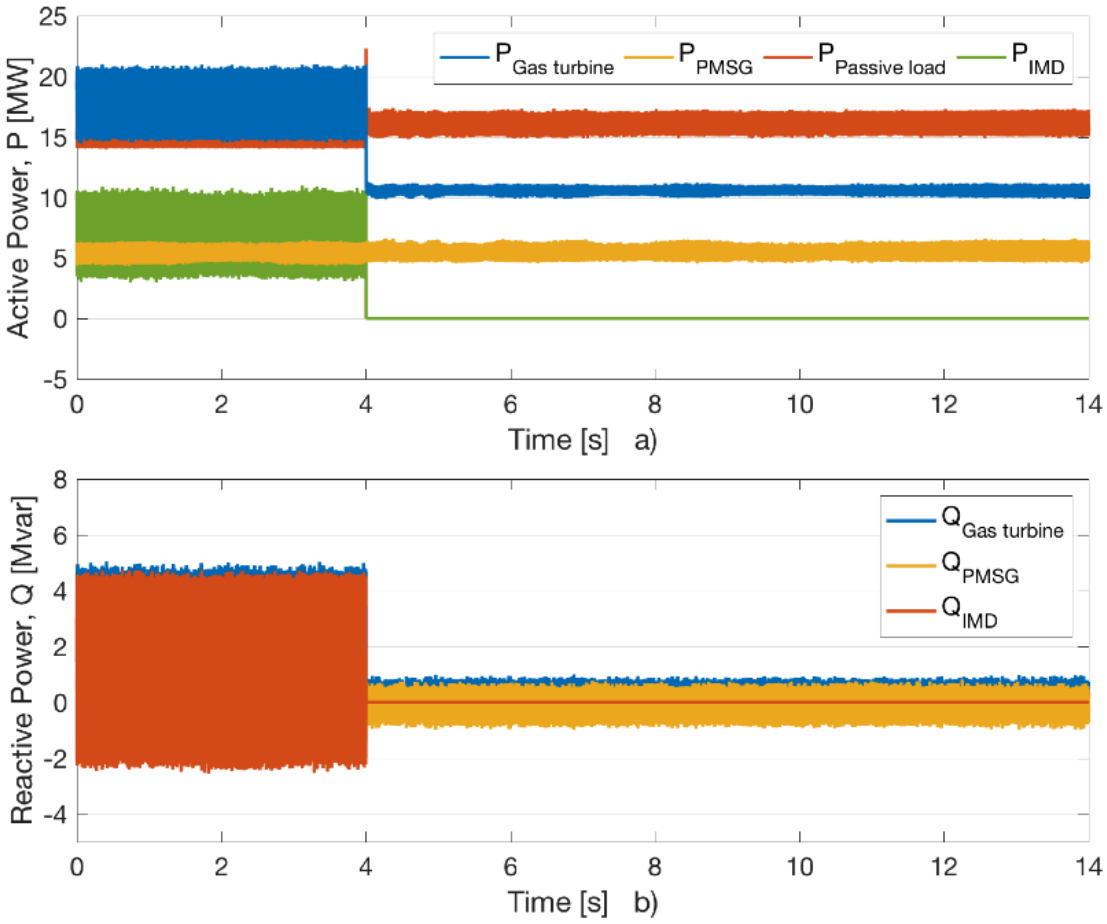

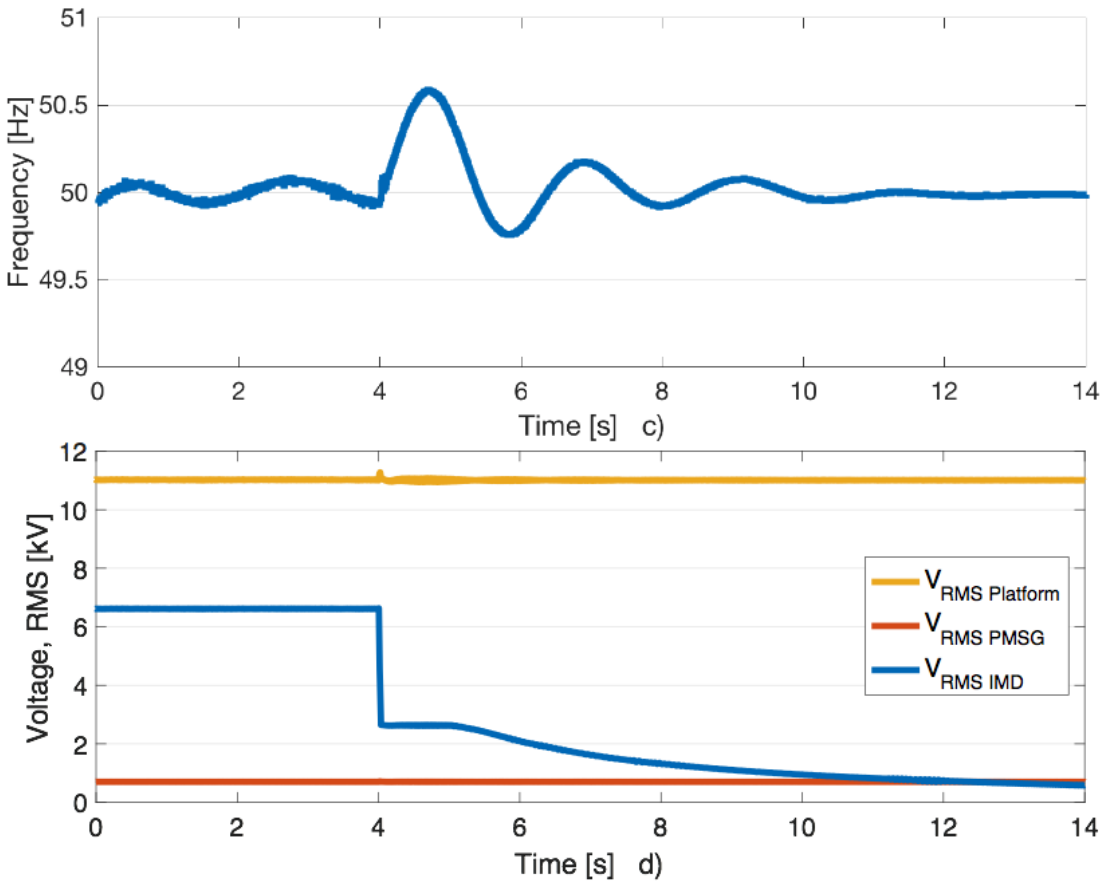

Figure 6.6. Contingency Effects on Full Wind Integrated Oil & Gas Platform Microgrid; Loss of Motor Load

6.5.3. Loss of Passive Load

The sudden loss of passive load is simulated with the aim of verifying that operation is maintained within the NORSOK limits. The production unit is an aggregated gas turbine rated at $46MVA$ connected to a passive load of $16MW$. The wind system is rated at $6MW$, and the induction motor drive is rated at $8MVA$. Both production and passive load are connected at the platform voltage of $11kV$, while the induction motor drive (IMD) is transformed up from $6.6kV$, and the wind system is rated at $0.69kV$. The wind system is connected to the platform through a transmission line rated at $33kV$.

The duration of the simulation is set to 12 seconds, and the $8MW$ of passive load is lost at $t = 4s$. The system is initialized at rated output at $t = 0$. The loss is simulated by a breaker opening at the loss time, disconnecting half the passive load from the platform. The loss corresponds to 17.4% of the rated gas turbine power, similar as for the motor case of 6.5.2. $8MW$ load corresponds to a huge loss, and will give a good picture on the platform's ability to handle passive losses.

Figure 6.7 shows the effect of a sudden loss of passive load on the platform electric system. The active power can be seen in a). The active power of the passive load seen from the platform drops immediately to half of its original value as the load is lost. The gas turbine power drops correspondingly, while the wind system power remains unaffected at rated output. From the reactive power plot seen in b), the loss of the resistive passive load has no effect on the reactive power in the system.

The frequency and rms voltages can be seen in c) and d) respectively. The loss of load causes a sudden spike in frequency as the production is suddenly higher than the consumption. The deviation is however less than 1.5%, well within the NORSOK limits, and stabilizes after $\sim 6s$. A voltage spike of $\sim 9\%$ is observed in the platform voltage, also within the transient NORSOK limits.

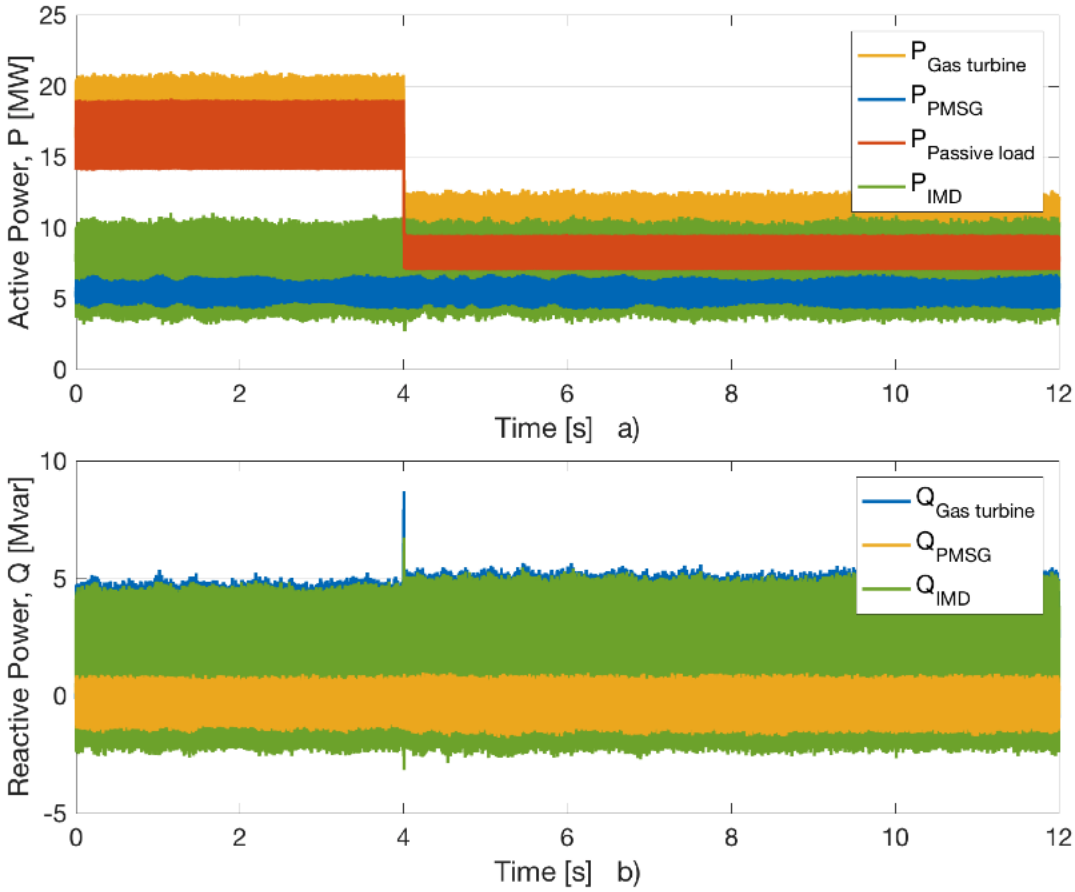

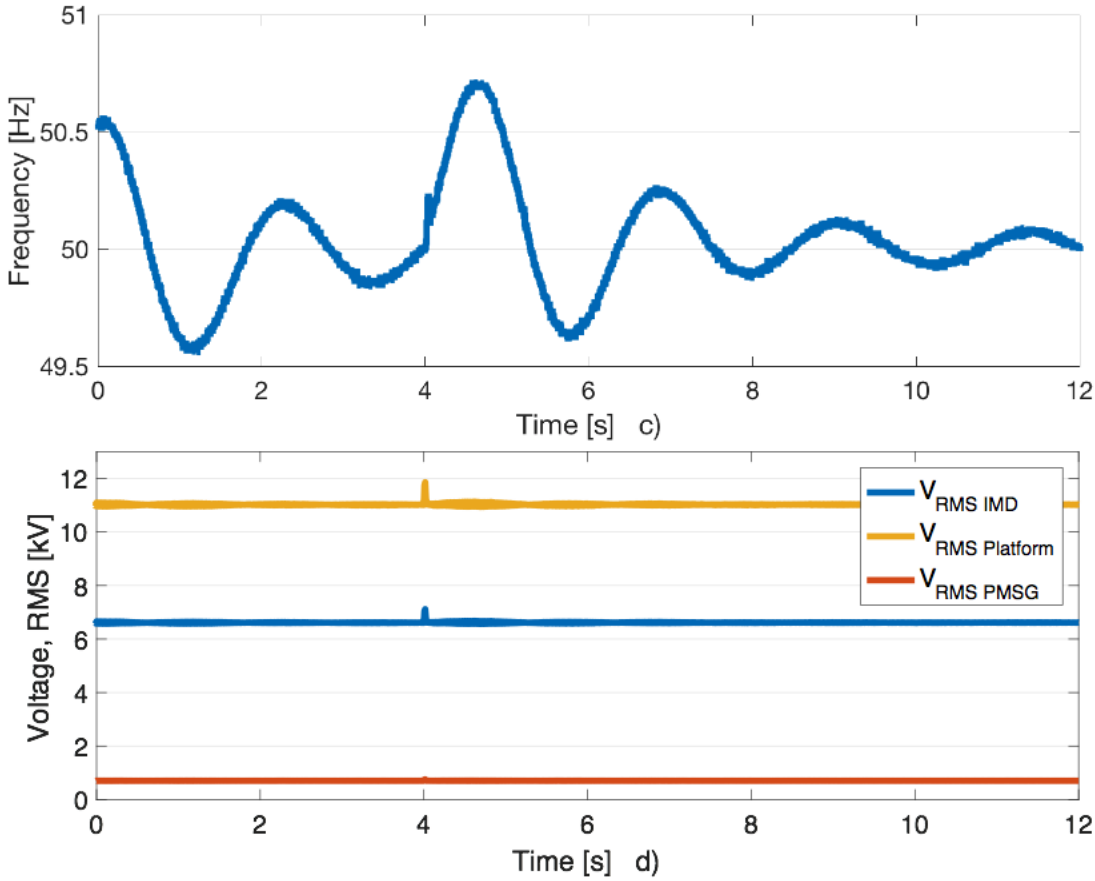

Figure 6.7. Contingency Effects on Full Wind Integrated Oil & Gas Platform Microgrid; Loss of Passive Load

6.5.4. Loss of Wind Power

The sudden loss of wind power production is simulated with the aim of verifying that platform operation is maintained within the NORSOK limits. The production unit is an aggregated gas turbine rated at $46MVA$ connected to a passive load of $10MW$. The wind system is rated at $6MW$, and the induction motor drive is rated at $8MVA$. Both production and passive load are connected at the platform voltage of $11kV$, while the induction motor drive (IMD) is transformed up from $6.6kV$, and the wind system is rated at $690V$. The wind system is connected to the platform through a transmission line rated at $33kV$.

The duration of the simulation is set to 15 seconds, and the $6MW$ wind power production is lost at $t = 8s$. The loss of wind power is modelled as a sudden drop in wind speed from rated speed to zero. Figure 6.8 shows the controller response to the sudden loss of wind. From the initial rated power output, the control references immediately drop to zero as the wind speed lowers. The actual dq-currents are seen to follow swiftly.

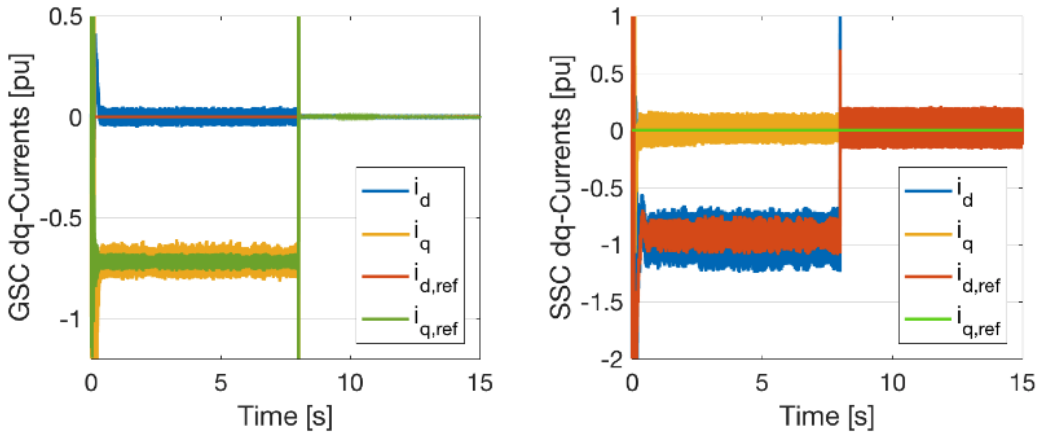

Figure 6.8. Contingency Effects on Full Wind Integrated Oil & Gas Platform Microgrid; Drop in Wind Speed

Figure 6.9 shows the platform response to losing the wind power production. The active power outputs can be seen in a). After the system start-up, the active power is seen to stabilize. At time $t = 8s$, the wind power production suddenly goes to zero, swiftly followed by an increased gas turbine power output. The induction motor drive and the passive load are seen to remain unaffected, with only a small spike at the time of loss. The reactive power of the transmission line is seen to reduce to near zero, as no power is transferred on the line.

The frequency and rms voltages can be seen in c) and d) respectively. The frequency is seen to oscillate after the system start-up due to the inertia of the gas turbine. As it works to stabilize, the wind power is suddenly lost with a small drop observed in the frequency as the gas turbine production catches up to the load. This actually stabilizes the frequency further, as it works opposite of the inertial effect. The biggest frequency deviation caused by the loss of wind power is $\sim 0.5\%$, well within the NORSOK requirements. The platform rms voltage is seen to remain stable at $11kV$ the whole simulation, with a slight dip at the time of the wind power loss. The drop is however $\sim 1\%$, and well within the NORSOK requirements. As the platform's total production and consumption are the same throughout the simulations, this would give the lower effect on frequency and voltage as observed.

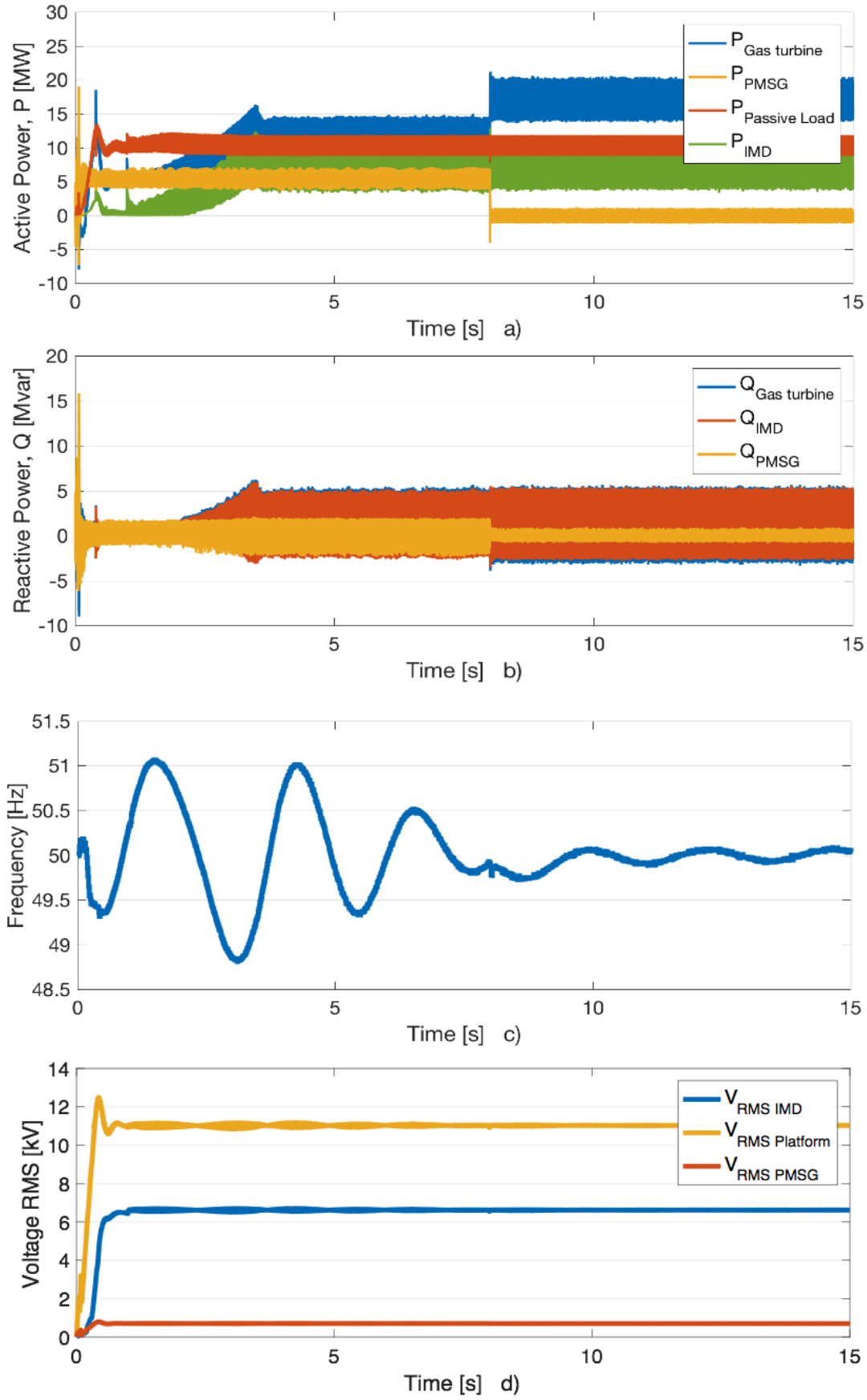

Figure 6.9. Contingency Effects on Full Wind Integrated Oil & Gas Platform Microgrid; Loss of Wind Power

6.5.5. Loss of Gas Turbine

The sudden loss of a gas turbine is simulated with the aim of verifying that platform operation is maintained within the NORSOK limits. The production unit is modeled as two gas turbine units rated at $23MVA$ each. The passive load is rated at $16MW$, the wind system at $6MW$, and the induction motor drive at $8MVA$. Both production and passive load are connected at the platform voltage of $11kV$, while the induction motor drive (IMD) is transformed up from $6.6kV$, and the wind system is rated at $690V$. The wind system is connected to the platform through a transmission line rated at $33kV$.

The duration of the simulation is set to 15 seconds, and one of the $23MW$ gas turbines is lost at $t = 5s$. The loss of the gas turbine is modelled as a sudden drop of turbine torque to zero in the torque applied to the synchronous generator. Figure 6.10 shows the two gas turbine generators' power outputs. The two turbines initially share the load equally between them. As the applied torque on generator 2 goes to zero, the power output also drops to zero. The inertia of the generator is seen to cause some oscillations around zero. Generator 1 at the same time is seen to step up production to account for the loss of the other unit.

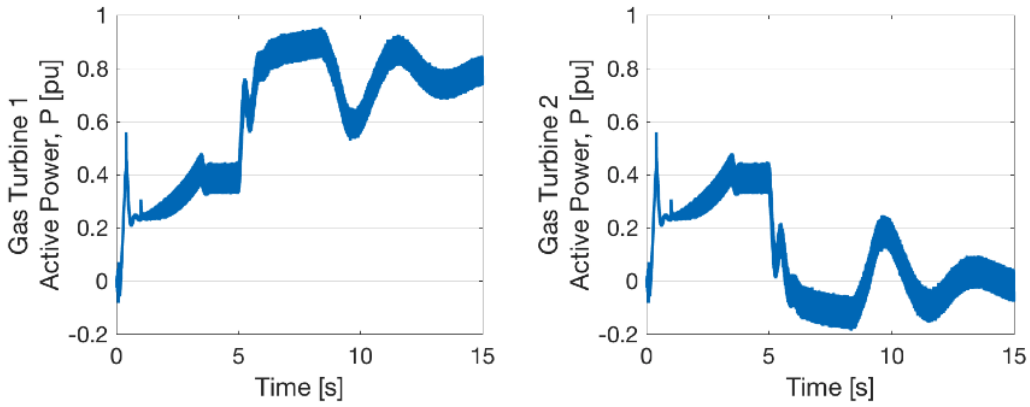

Figure 6.10. Contingency Effects on Full Wind Integrated Oil & Gas Platform Microgrid; Gas Turbine Power

Figure 6.11 shows the effect the loss of a gas turbine has on the platform electric system. The active power can be seen in a). After the system has stabilized after start-up, the system is seen to remain stable for the duration of the simulation. No apparent effect is seen in the active power output at the loss of a gas turbine. Gas turbine 1 was found big enough to handle the extra power production, and the fast response means no apparent effect is observed. At higher loads, the necessity of starting another generator or apply load-shedding could have yielded a more visible result. The reactive power outputs can be seen in b). Again, no apparent effects can be seen for the loss of one of the gas turbines. The outputs remain steady throughout the simulations after the initial start-up period, discussed more in detail in 6.5.1.

The system frequency and rms voltages can be seen in plots c) and d) respectively. The frequency is seen to experience an initial drop at the time of the loss, with following huge

oscillations for the next $10s$ at the inertial response of the two gas turbines. After this, the frequency is seen to stabilize again. The maximum deviations in frequency are $\sim 2.5\%$, and well within the NORSOK limits. The platform voltage is seen to remain steady at $11kV$, with no apparent voltage drop. However, the oscillations in the voltage is seen to increase and decline in rate with the oscillations in frequency. The system is found to be well within the NORSOK limits.

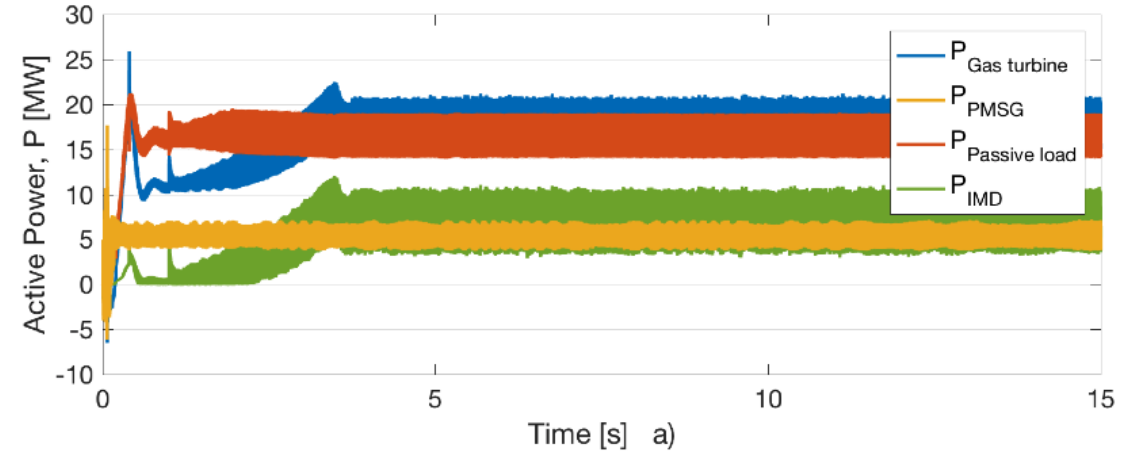

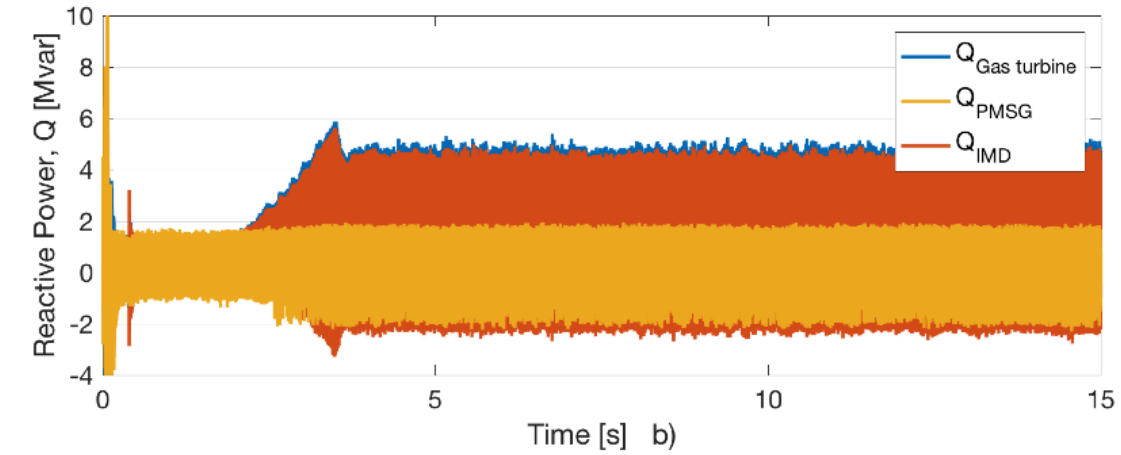

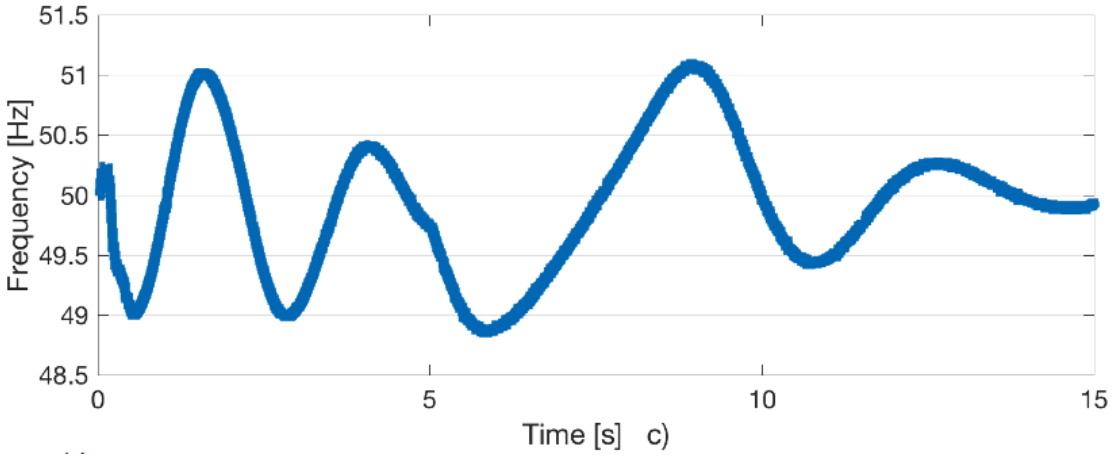

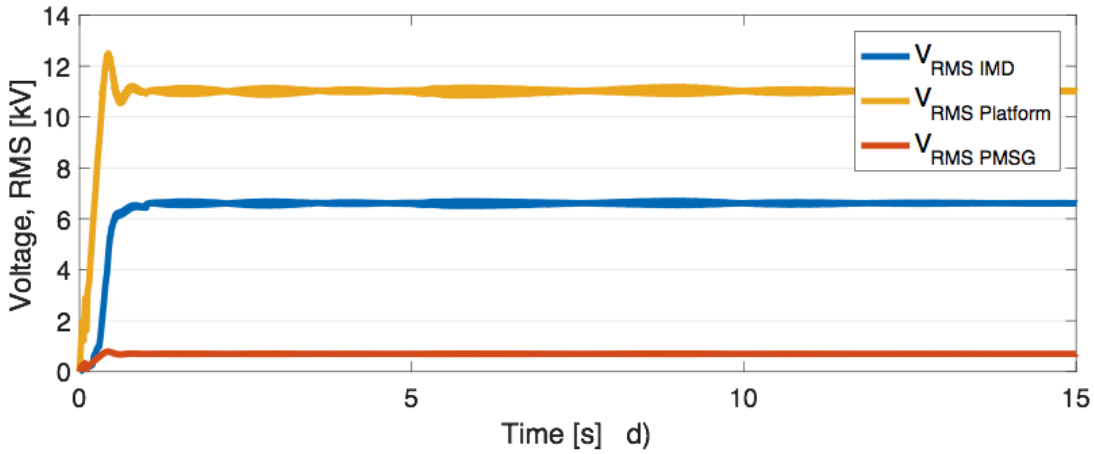

Figure 6.11. Contingency Effects on Full Wind Integrated Oil & Gas Platform Microgrid; Loss of Gas Turbine

6.6. DISCUSSION

A wind integrated oil & gas electric platform microgrid has been implemented in Matlab/Simulink and simulated for multiple test case scenarios. The models have all been tested separately in chapters 3 and 5. The test scenarios are designed to test the integrated system at normal operating conditions and for several of contingency events. This section will look more into the results obtained from the simulations in sections 6.4 and 6.5. A table summarizing the results of the simulations is given in section 6.1. Extra focus will be on challenges encountered in the simulations and possible improvements of the model.

The table summarizing the results of the simulations of this chapter shows that the system stays within the NORSOK limits for all simulation test cases. As the wind power production is small compared to the gas turbine, this is as expected. The wind power integration of one wind turbine has therefore been validated for the simulations of this thesis. Only one wind turbine has been used for all simulations in this thesis. This is not an unlikely scenario, as full scale implementation would start with one initial turbine to test the live response of the system. Also, the turbine ratings are fast increasing, meaning the number of wind turbines required to power the platform decreases every year. Some trials at increasing the turbine rating or adding extra wind turbines to the system were unsuccessful as it destabilized the system. However, given the time span of the thesis, this was not a high priority. Investigating the system response to multiple and/or bigger wind turbines is suggested as a point for further work.

The first simulation case tests the complete oil & gas offshore installation's response to including a PMSG wind energy system. The applied wind profile is a shorter variant of the one used in chapter 3. The introduction of wind power to the platform seems to work fine. The wind turbine is at all times allowed to produce at its optimal power output as the wind speed varies. The gas turbine works as the system balancer, and adjusts its own production to adapt to the wind power. Some minor oscillations are seen in the frequency even at steady state operation, probably a result of the speed controller being faster than the oscillations. The variations in wind speed are seen to affect both voltage and frequency, which experience greater oscillations than for steady state. For real life application, the variations in wind speed would be considered extremely fast. One second of the wind speed profile applied in the simulations corresponds to one hundred minutes of real wind speed data. The rapid wind changes would therefore be rare for actual operation. As mentioned earlier in the chapter, the inertia of the wind power generator had to be reduced in the integrated system. The inertial value used successfully in chapter 3 was seen to cause instability when applied in the complete system. The oscillations were seen to grow rather than decline. A higher inertia would have caused a more oscillating system and possibly bigger deviations in voltage and frequency. The fast-changing wind speed could also have affected the system negatively, adding to the effect of a high inertia. For further work, this should be looked more into. The modelled transmission line is seen to have some losses, although small as the line voltage is high. The line is also seen to consume some reactive power as expected. The wind power system controllers are seen to work well. The oscillations are seen to be slightly larger than for simulation of the wind turbine alone in chapter 3. This is probably caused by the switching frequency being halved to speed up the simulations.

The second simulation case is part of the tests investigating the system response to selected contingency events. The system response at start-up and for starting one induction motor drive is tested. The start-up of the system is seen to be a considerable transient event, with a large inertial response. In comparison, the start of an induction motor drive yields only a small response. This is because the motor is loaded and accelerated gradually, being an advantage of implementing a variable speed drive. Compared to the platform system without any wind power in subsection 5.6.1, the deviations are seen to be slightly lower. The reason for this is that the total production capacity with wind power is higher, and some of the load previously handled by the gas turbine is handled by the wind power production instead.

The third simulation case tests the system response to losing load. This is tested for both passive load and motor load. As in chapter 5, the loss of passive load is seen to affect the system more negatively than losing a motor drive with higher overshoots in voltage. The reason for this is related to the reactive power consumption of the motor drive. As the motor drive is lost, the reactive power production on the platform decreases and only the transmission line connecting the wind farm consumes any reactive power. A decreasing reactive power will cause the voltage to fall and works opposite to the effect that losing load has on the platform voltage. The purely resistive passive load does not have this effect, giving

the observed higher voltage overshoot. It could also be possible the high system oscillations caused by the motor drive have some effect. The oscillations reduce drastically when the motor drive is lost and could affect the amplitude of the voltage and frequency overshoots on the platform. However, this is much more uncertain and would need to be investigated further to prove. Importantly, both platform voltage and frequency are seen to stabilize after the load losses, and stay within the NORSOK required limits.

The fourth simulation case tests the system response to losing all wind power production. The effects are found to be small, with a small voltage and frequency drop. The relative small size of the wind energy system compared to the platform production and load should also suggest a small response. Another factor is how the total production and consumption on the platform remains unchanged for the simulation. The system only experiences a change in the type of production unit. This suggests the effect on platform voltage and frequency should be small as long as the response of the balancing production unit is fast. This is seen to be the case for the gas turbine. Both a higher inertia in the wind energy system and increasing the size of the wind power production should be investigated further as discussed earlier.

The final simulation case tests the system response to losing one of the two gas turbine production units. This would usually lead to the start of a back-up generator, but only the immediate effect of the loss has been considered. The effect of losing one gas turbine is seen mostly on the platform frequency. Even as the remaining gas turbine adapts quickly, the loss is substantial as nearly half the production capacity is lost. The gas turbines are also the frequency balancing units, and the inertia of the generators give a big inertial response. The effect in voltage is almost not seen, except having higher oscillations as the frequency oscillates from the nominal. Again, this could be as the total production and consumption on the platform remains the same throughout the simulations. The fast response of the gas turbine model is also questioned whether to be realistic behavior for real life operation. The fact that the required speed reference adjustments are small ($< 2\%$) suggests small adjustments can handle big transients. Other turbine models might behave differently, which would affect the results obtained in this thesis. This is suggested to be investigated further.

The resulting model ended as a big and complicated system. This meant the simulations became really time consuming, using near 30 minutes per simulated second. Given the amount of simulations in the thesis and the limited time frame of the thesis, the sampling time was therefore put at a higher level than ideal. This is seen in the outputs of active and reactive power throughout the simulations. The outputs are seen to have large oscillations, not ideal for simulation purposes. Further work should seek to redo some of the simulations at a lower sample time to verify the results of this thesis.

CONCLUSIONS

A wind integrated oil & gas offshore installation has been modelled and simulated in order to evaluate the performance under transient contingency conditions. The simulations have been performed by use of the simulation software Matlab/Simulink. The model has been divided into two subsystems; A PMSG wind energy system and an oil & gas platform microgrid. Separate testing has been performed on both subsystems to verify the correct build and working of all components. The complete wind integrated oil & gas offshore installation has then been tested thoroughly in accordance with the problem description of this thesis. This chapter presents the most important conclusions obtained from this thesis.

System 1 has been the PMSG wind energy system. It is concluded that the implemented control system works well for varying wind speed operations. The wind system is able to optimize power output at all wind speeds, which is important from a cost perspective. The advantage of having the back-to-back DC-link converter is demonstrated when testing for the operational grid requirements for European offshore wind power production. The frequency and voltage on the generator side is seen to remain unaffected by transients on the grid side. This is thought to be especially advantageous for integration in smaller grids, where transient events could have big effects on system frequency and voltage. The wind turbine of choice is therefore concluded to be a good alternative for offshore integration.

System 2 has been the oil & gas installation microgrid. The gas turbine model is shown to have a fast response with high ability to maintain the nominal frequency during transients. The induction motor drive is based on direct torque control which yields a fast response with excellent speed and torque control for all speeds. The high oscillations for steady state operation were however not ideal, but were not thought to affect the conclusions in a negative way. The platform microgrid proved to work as intended, with adequate response for the tested transients. The system was seen to operate at rated conditions for steady state, and within the NORSOK transient limits for all tested transients.

System 3 has been the wind integrated oil & gas offshore installation. The biggest voltage and frequency deviations were seen at system start-up at full load with a voltage overshoot of $\sim 15\%$, and a frequency drop of $\sim 4\%$. The biggest contingency effect was a voltage overshoot for losing passive load at $\sim 9\%$, and a frequency deviation of $\pm 2.5\%$ at losing one gas turbine. It is concluded that the integration of one large wind turbine is feasible within the set standards of NORSOK/IEC. The gas turbines are seen to balance the system, allowing the wind power unit to optimize its production for varying wind speeds. The gas turbines are seen to respond fast, limiting the transient effects on the simulated system. The fast response is questioned whether to be realistic for real life turbines, and slower units could negatively affect the results seen in this thesis.

The conclusion of this thesis is that integration of one wind turbine with an oil & gas offshore installation is feasible within the NORSOK/IEC standards for all scenarios and contingencies tested in this thesis. Offshore microgrids are considered more susceptible to

negative effects of transients given their small size, so the DC-link setup of the wind turbine is considered a good choice for integration with oil & gas installations. It should be noted that the simulations are dependent on the chosen parameters, components and modelling techniques applied for this thesis. Further work should seek to increase realism further by applying even more components, and get parameters closer to those found on actual oil & gas installations.

FURTHER WORK

This thesis should only be considered a preliminary study in establishing the performance of a wind integrated oil & gas offshore installation. Throughout the discussions of this thesis a number of possible improvements are suggested. This chapter will present the most important suggestions for further work.

Several improvements to the models of the thesis are suggested. The inertia of the wind energy generator was lowered in the integrated system. The effect of a higher and more realistic inertia should be investigated. A better soft start device for the induction motor drive is also suggested to lower the transients the system experiences at motor start-up. The simulations also experience high oscillations from the motor drive, and these should be sought reduced.

All simulations have been done with one wind turbine implemented in the system. For a preliminary implementation for testing purposes this could be realistic. It is, however, reasonable to think that both bigger sized turbines and whole wind farms could be integrated in the near future. Further work should therefore investigate adding bigger, or more, wind turbines to uncover any difficulties this may cause. Other simulation scenarios with different components and variations in contingency events could also be looked into. Also, more realistic data, based directly on the units found at actual oil & gas installations, should be sought. These are however difficult to get, as they are considered industry secrets. A sensitivity analysis could uncover the effects of varying parameters in the system, and is suggested as an alternative to better data gathering.

REFERENCES

[1] Norsk Petroleum, "Statens Inntekter". 2017; [cited: 01.06.2017]. Available from: http://www.norskpetroleum.no/okonomi/statens-inntekter/.

[2] SSB, "Økonomiske Analyser - Økonomisk utsyn over året 2016." 2017. [cited: 04.06.2017] Available from: http://ssb.no/nasjonalregnskap-og-konjunkturer/oa/_attachment/299128?_ts=15aaf154478

[3] United Nations Framework Convention on Climate Change, "Paris Agreement." 2015. [cited: 04.06.2017] Available from: http://unfccc.int/files/essential_background/convention/application/pdf/english_paris_agreement.pdf

[4] SSB, "Production and Consumption of Energy, Energy Account, 2014-2015." 2016. [cited: 04.06.2017] Available from: http://www.ssb.no/en/energi-og-industri/statistikker/energiregnskap

[5] Norwegian Environment Agency, Norwegian Petroleum Directorate, NVE and Petroleum Safety Authority, "Klimakur 2020." 2010. [cited: 04.06.2017] Available from: http://miljodirektoratet.no/no/Publikasjoner/Publikasjoner/2010/Mars/Klimakur_2020__Tiltak_og_virkemidler_for_a_na_norske_klimamal_mot_2020/

[6] ABB, "Electrification of petroleum installations." 2016. [cited: 01.06.2017] Available from: http://new.abb.com/docs/librariesprovider50/om-oss---barekraftig-utvikling/electrification-of-petroleum-installations-highresolution.pdf?sfvrsn=2

[7] Statoil, "Hywind Scotland Pilot Park." 2016. [cited: 20.05.2017] Available from: http://www.statoil.com/en/TechnologyInnovation/NewEnergy/RenewablePowerProduction/Offshore/HywindScotland/Downloads/Public Event - Hywind Scotland Pilot Park 20jan2016.pdf

[8] J. F. Opedal, "Specialization Project - Feasibility of Wind Power Integration With Oil & Gas Offshore Installations": NTNU; 2016.

[9] Siemens, "Wind Turbine SWT-6.0-154 - Technical specifications". 2016. Available from: https://www.siemens.com/global/en/home/markets/wind/turbines-and-services/swt-6-0-154.html.

[10] Statoil, "Hywind Scotland Pilot Park". 2016. Available from: http://www.statoil.com/en/TechnologyInnovation/NewEnergy/RenewablePowerProduction/Offshore/HywindScotland/Downloads/Public Event - Hywind Scotland Pilot Park 20jan2016.pdf.

[11] J. Machowski, J. Bialek, J. Bumby, "Power System Dynamics: Stability and Control": Wiley; 2011.

[12] Mathworks, "Wind Turbine - Implement model of variable pitch wind turbine". 2006; [cited: 18.05.2017]. Available from: https://se.mathworks.com/help/physmod/sps/powersys/ref/windturbine.html;jsessionid=a7eb5c8f9ebdd074e3eb01206d60.

[13] T. Burton, N. Jenkins, D. Sharpe, E. Bossanyi, "Wind Energy Handbook". Chichester, UK: Chichester, UK: John Wiley & Sons, Ltd; 2011.

[14] Z. Jianzhong, C. Ming, C. Zhe, F. Xiaofan, "Pitch angle control for variable speed wind turbines". 2008 Third International Conference on Electric Utility Deregulation and Restructuring and Power Technologies; 2008 6-9 April 2008.

[15] A. Hwas, R. Katebi, “Wind turbine control using PI pitch angle controller”. IFAC Proceedings Volumes. 2012;45(3):241-6.

[16] N. Mohan, “Advanced Electric Drives: Analysis, Control, and Modeling Using MATLAB / Simulink”: Wiley; 2014.

[17] M. Yin, G. Li, M. Zhou, C. Zhao, “Modeling of the Wind Turbine with a Permanent Magnet Synchronous Generator for Integration”. 2007 IEEE Power Engineering Society General Meeting; 2007 24-28 June 2007.

[18] N. Mohan, T. M. Undeland, W. P. Robbins, “Power electronics : converters, applications, and design”. 3rd ed. ed. Hoboken, N.J: Wiley; 2003.

[19] P. C. Krause, O. Wasynczuk, S. D. Sudhoff, I. P. E. Society, “Analysis of electric machinery and drive systems”. 2nd ed. ed: Wiley - IEEE Press; 2002.

[20] V. Blasko, V. Kaura, “A new mathematical model and control of a three-phase AC-DC voltage source converter”. IEEE Transactions on Power Electronics. 1997;12(1):116-23.

[21] Y. Zhu, X. Shi, Y. Dan, “Deduction of coordinate transform for instantaneous reactive power theory and analysis on relationship between α — β and dq0 transformation”. 2009 9th International Conference on Electronic Measurement & Instruments; 2009 16-19 Aug. 2009.

[22] J. A. Suul, M. Molinas, L. Norum, T. Undeland, “Tuning of control loops for grid connected voltage source converters”. 2008 IEEE 2nd International Power and Energy Conference; 2008 1-3 Dec.

[23] N. K. Jena, K. B. Mohanty, H. Pradhan, S. K. Sanyal, “A decoupled control strategy for a grid connected direct-drive PMSG based variable speed wind turbine system”. 2015 International Conference on Energy, Power and Environment: Towards Sustainable Growth (ICEPE); 2015 12-13 June 2015.

[24] Y. Errami, M. Ouassaid, M. Maaroufi, “Control of a PMSG based Wind Energy Generation System for Power Maximization and Grid Fault Conditions”. Energy Procedia. 2013;42(Complete):220-9.

[25] M. Meyer, T. Grote, J. Bocker, “Direct torque control for interior permanent magnet synchronous motors with respect to optimal efficiency”. 2007 European Conference on Power Electronics and Applications; 2007 2-5 Sept. 2007.

[26] Statoil. Wind 2015 - Observation Data from Gullfaks C. 2016.

[27] J. F. Manwell, J. G. McGowan, A. L. Rogers. Wind Energy Explained. Chicester: John Wiley & Sons; 2009.

[28] J. Jonkman, S. Butterfield, W. Musial, G. Scott, “Definition of a 5-MW reference wind turbine for offshore system development”. National Renewable Energy Laboratory, Golden, CO, Technical Report No NREL/TP-500-38060. 2009.

[29] A. Garces Ruiz, M. Molinas, F. F. I. M. O. E. I. F. E. Norges Teknisk-Naturvitenskapelige Universitet. Design, Operation and Control of Series-connected Power Converters for Offshore Wind Parks. NTNU; 2012.

[30] C. Bajracharya, M. Molinas, J. A. Suul, T. M. Undeland, “Understanding of tuning techniques of converter controllers for VSC-HVDC”2008: Helsinki University of Technology.

[31] M. Santos-Mugica, E. Robles, A. G. Endegnanew, E. Tedeschi, et al., “Grid integration and power quality testing of Marine Energy Converters: Research activities in the MaRINET Project”. 2014 Ninth International Conference on Ecological Vehicles and Renewable Energies (EVER); 2014 25-27 March 2014.

[32] Statnett, “Funksjonskrav i kraftsystemet (FIKS 2012).” 2012. [cited: 04.06.2017] Available from: www.statnett.no/Global/Dokumenter/Kraftsystemet/Systemansvar/FIKS 2012.pdf

[33] A. L. Sheldrake, “Handbook of electrical engineering : for practitioners in the oil, gas and petrochemical industry”. Chichester: Wiley; 2003.

[34] B. K. Bose, “Modern power electronics and AC drives”. Upper Saddle River, N.J: Prentice Hall PTR; 2002.

[35] W. He, G. Jacobsen, T. Anderson, F. Olsen, et al., “The Potential of Integrating Wind Power with Offshore Oil and Gas Platforms”. Wind Engineering. 2010;34(2):125-37.

[36] H. G. Svendsen, M. Hadiya, E. V. Øyslebø, K. Uhlen, “Integration of offshore wind farm with multiple oil and gas platforms”. 2011 IEEE Trondheim PowerTech; 2011 19-23 June 2011.

[37] A. R. Årdal, T. Undeland, K. Sharifabadi, “Voltage and frequency control in offshore wind turbines connected to isolated oil platform power systems”. Energy Procedia. 2012;24:229-36.

[38] A. R. Årdal, K. Sharifabadi, B. Ø, V. Berge, “Challenges with integration and operation of offshore oil & gas platforms connected to an offshore wind power plant”. 2014 Petroleum and Chemical Industry Conference Europe; 2014 3-5 June 2014.

[39] S. K. Yee, J. V. Milanovic, F. M. Hughes, “Overview and Comparative Analysis of Gas Turbine Models for System Stability Studies”. IEEE Transactions on Power Systems. 2008;23(1):108-18.

[40] W. I. Rowen, “Simplified Mathematical Representations of Heavy-Duty Gas Turbines”. Journal of Engineering for Power. 1983;105(4):865-9.

[41] Mathworks, “Synchronous Machine - Model the dynamics of three-phase round-rotor or salient-pole synchronous machine”. 2006; [cited: 20.05.2017]. Available from: https://se.mathworks.com/help/physmod/sps/powersys/ref/synchronousmachine.html;jsessionid=cf6906e7ce25d2c474a2f79fe64c.

[42] V. Orlandini, L. Pierobon, S. Schløer, A. De Pascale, et al., “Dynamic performance of a novel offshore power system integrated with a wind farm”. Energy. 2016;109:236-47.

[43] M. L. Kolstad, K. Sharifabadi, A. R. Årdal, T. M. Undeland, “Grid integration of offshore wind power and multiple oil and gas platforms”. 2013 MTS/IEEE OCEANS - Bergen; 2013 10-14 June 2013.

[44] A. R. Ardal, S. D'Arco, R. E. Torres-Olguin, T. Undeland, et al., “Parametric sensitivity of transients in an islanded system with an offshore wind farm connected to an oil platform”. Power Electronics and Applications (EPE 2011), Proceedings of the 2011-14th European Conference on; 2011: IEEE.

[45] Mathworks, “Simulate Variable Speed Motor Control”. 2006; [cited: 29.05.2017]. Available from: https://se.mathworks.com/help/physmod/sps/powersys/ug/simulating-variable-speed-motor-control.html.

[46] S. J. Chapman, “Electric Machinery Fundamentals”: McGraw-Hill; 2012.

[47] Mathworks, “Asynchronous Machine - Model the dynamics of three-phase asynchronous machine”. 2006; [cited: 20.05.2017]. Available from: https://se.mathworks.com/help/physmod/sps/powersys/ref/asynchronousmachine.html.

[48] R. C. Dugan, M. F. McGranaghan, H. W. Beaty, “Electrical power systems quality”. New York, NY: McGraw-Hill,| c1996. 1996.

[49] ABB, “DTC: A motor control technique for all seasons”. 2017. Available from: http://new.abb.com/drives/dtc.

[50] H. Abu-Rub, A. Iqbal, J. Guzinski, “High Performance Control of AC Drives with Matlab / Simulink Models”. Hoboken: Wiley; 2012.

[51] Z. Alnasir, A. Almarhoon, “Design of direct torque controller of induction motor (DTC)”. International Journal of Engineering and Technology (IJET). 2012;4(2).

[52] L. Shue, F. Chao, “Design and Simulation of Three-phase AC Motor Soft-start”. 2013 Third International Conference on Intelligent System Design and Engineering Applications; 2013 16-18 Jan. 2013.

[53] Mathworks, “Retune the Drive Parameters”. 2006; [cited: 20.05.2017]. Available from: https://se.mathworks.com/help/physmod/sps/powersys/ug/advanced-users-retune-the-drive-parameters.html - f0-29408.

[54] NORSOK E-001, Electrical systems. Rev. 5, July 5, (2007).

[55] H. Saadat, “Power system analysis”: WCB/McGraw-Hill; 1999.

[56] A. Nysveen, “Maritime and Offshore Power Systems - (Compendium NTNU-course TET 4200)”: NTNU; 2016.

[57] J. G. Balchen, T. Andresen, B. A. Foss, “Reguleringsteknikk”: Institutt for teknisk kybernetikk, NTNU; 2004.

[58] E. Tedeschi, “VSC Modeling and Control Lecture notes 2A”. NTNU Course: ELK-23 Power Electronics in Future Power Systems; 2016 Aug.-Dec.

[59] N. Djagarov, J. Djagarova, Z. Grozdev, M. Bonev, et al., “PI vector control study for wind PMSG”. 2016 IEEE 16th International Conference on Environment and Electrical Engineering (EEEIC); 2016 7-10 June 2016.

APPENDIX

A. PI-CONTROLLER TUNING PRINCIPLES

The vector control of the PMSG converters of chapters 2.5 and 2.6 requires accurate tuning of the PI-controllers to function properly. Different criteria apply depending on whether the PI-controller is part of the inner or outer control loop. In general, the required response speed increases towards the inner loop, so while the outer control loop is designed for optimal regulation and stability, the inner control loop is designed to achieve a fast response. This is achieved by tuning the inner controller to the *modulus optimum* criteria, and the outer controller to the *symmetrical optimum* criteria [30].

The PI-controller tuning of both inner and outer control loop is based on the transfer function of the ideal PI-controller, given as [57]:

$$H_c = K_p \frac{1 + T_i s}{T_i s} \tag{53}$$

where K_p is the proportional gain, and $T_i = K_p/K_i$ where T_i is the integral time, and K_i is the integral gain. Both tuning methods seek to optimize the values of K_p and T_i, to match their respective design goals. The different criteria are described in more detail below.

A.1. INNER CURRENT CONTROLLER

Figure A.1 demonstrates the block diagram of the inner current control scheme. $K_{p,pu}$ and T_i are the PI-controller parameters, as seen in equation (53). T_a is the time constant of the PWM converter, while τ_{pu} is the system time constant of the line. The open loop transfer function of the control scheme is given as:

$$G_{C,OL} = R(s) * Y(s) * G(s) = K_{p,pu}\left(\frac{1 + T_i s}{T_i s}\right) * \frac{1}{1 + T_a s} * \frac{1}{R_{pu}} \frac{1}{1 + \tau_{pu} s} \tag{54}$$

The goal is to tune the PI-controller variables so they cancel the largest time constant, while keeping the closed loop gain large for as high a frequency as possible.

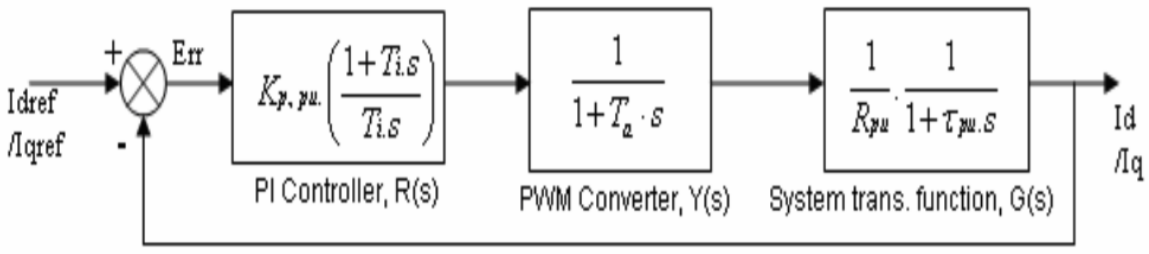

Figure A.1.Block Diagram of Inner Current Control Scheme [30]

The time constant T_a should be adjusted to account for the computation time of the control algorithm [58]. This is approximated to one switching period and comes in addition to the average delay T_a of updating the modulation ratio of the PWM converter. The new time constant $T_e = T_a + T_{sw} = 1.5T_{sw}$ is therefore used for the PWM time constant in the rest of the thesis.

The modulus optimum method is applicable for low order systems, such as the current controller, with only one integrator in the transfer function. For systems with one dominant time constant, τ_{pu}, the modulus optimum method works to cancel this. This is achieved by setting the modulus optimum criteria as:

$$T_i = \tau_{pu} \tag{55}$$

$$K_{p,pu} = \frac{\tau_{pu} R_{pu}}{2T_e} \tag{56}$$

The resulting open and closed loop transfer functions become:

$$G_{C,OL} = \frac{1}{2T_e} * \frac{1}{s(1 + T_e s)} \tag{57}$$

$$G_{C,CL} = \frac{1}{2{T_e}^2 s^2 + 2T_e s + 1} \tag{58}$$

A.2. Outer DC-Voltage Controller

Figure A.2 demonstrates the block diagram of the outer control scheme. $K_{pv,pu}$ and T_{iv} are the PI-controller parameters, as seen in (53). T_{eq} is the approximated time constant of the inner current controller, and is added as the errors of two transfer functions equal to $2T_e$. The feed-forward term is added to compensate for a slower dynamic response of the outer loop.

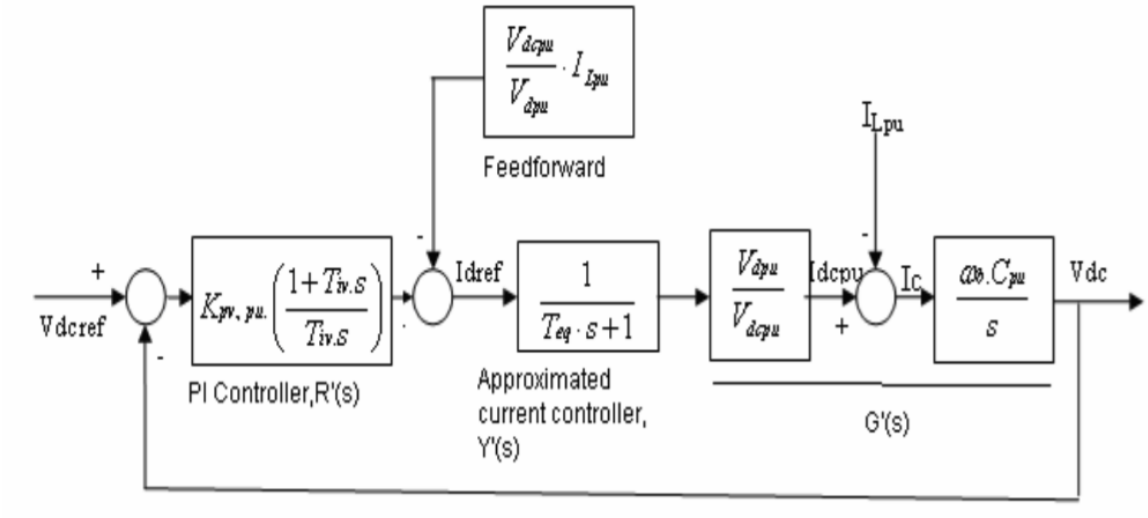

Figure A.2. Block Diagram of Outer DC-voltage Control Scheme [30]

The open loop transfer function of the control scheme is given as:

$$G_{v,OL} = R'(s) * Y'(s) * G'(s) = K_{pv,pu}\left(\frac{1+T_{iv}s}{T_{iv}s}\right) * \frac{1}{1+T_{eq}s} * \left(\frac{V_{d,pu}}{V_{DC,pu}}\frac{\omega_b C_{pu}}{s}\right) \quad (59)$$

For systems where a pole is either near or in the origin, as for the outer control loop, the modulus optimum method is not applicable. Pole cancelation would give two poles in the origin, giving an unstable system. The symmetrical optimum method is therefore applied instead. The method works to force the frequency response of the system towards low frequencies as it maximizes the phase margin. This makes the system more stable and more robust against disturbances. The maximum phase margin occurs for the crossover frequency $\omega_d = 1/\sqrt{T_{iv}T_{eq}}$, and is centered between $1/T_{iv}$ and $1/T_{eq}$. The resulting parameters for the PI-controller by the symmetrical optimum criterion becomes:

$$T_{iv} = a^2 T_{eq} \quad (60)$$

$$K_{pv,pu} = \frac{V_{DC,pu}}{V_{d,pu}}\frac{1}{\omega_b C_{pu} a T_{eq}} \quad (61)$$

with a being the symmetrical distance between the crossover frequency ω_d and $1/T_{iv}$. The resulting open and closed loop transfer functions become:

$$G_{v,OL} = \frac{1}{a^3 {T_{eq}}^2 s^2} * \left(\frac{1+a^2 T_{eq}s}{1+T_{eq}s}\right) \quad (62)$$

$$G_{v,CL} = \frac{1+a^2 T_{eq}s}{a^3 {T_{eq}}^3 s^3 + a^3 {T_{eq}}^2 s^2 + a^2 T_{eq}s + 1} \quad (63)$$

B. System Controllers Tuning

B.1. Inner Current Controller Tuning (PMSG Wind System)

The tuning of the inner current controllers is based on the modulus optimum method as described in section A.1. The control parameters are given by the tuning criteria as:

$$T_i = \frac{L_{pu}}{\omega_b R_{pu}} \tag{64}$$

$$K_{p,pu} = \frac{L_{pu}}{2\omega_b T_e} \tag{65}$$

R_{pu} and L_{pu} are the resistance and the inductance of the generator or filter, depending on which controller the parameters are used to control. T_e is the time constant of the pulse width modulation.

Two inner current controllers are used for the control of the PMSG in this thesis, the generator side converter and the system side converter. Applying the numerical values on the generator side of the converter gives the control parameters of the i_d current as:

$$T_{id} = \frac{0.8}{(2\pi * 50) * 0.1} = 0.0255 \tag{66}$$

$$K_{pd,pu} = \frac{0.8 * (1.5 * 10000)}{2(2\pi * 50)} = 8.4883 \tag{67}$$

And for the i_q current as:

$$T_{iq} = \frac{0.7}{(2\pi * 50) * 0.1} = 0.0223 \tag{68}$$

$$K_{pq,pu} = \frac{0.7 * (1.5 * 10000)}{2(2\pi * 50)} = 7.4278 \tag{69}$$

For the system side of the converter the control parameters of both the i_d and i_q current become:

$$T_{idq} = \frac{0.15}{(2\pi * 50) * 0.01} = 0.0477 \tag{70}$$

$$K_{pdq,pu} = \frac{0.15 * (1.5 * 10000)}{2(2\pi * 50)} = 33.33 \tag{71}$$

Figure B.1 gives the Bode plots of the open and closed loop transfer functions of the generator and system side inner current controllers. The open loop function is marked in blue and gives the phase margin and the gain margin of the system. The generator side converter has phase margin $PM = 65.53°$, and the system side converter has $PM = 51.83°$. Both

systems have an infinite gain margin $GM = \infty$. This shows the system has a stable response, pointing to adequate tuning parameters.

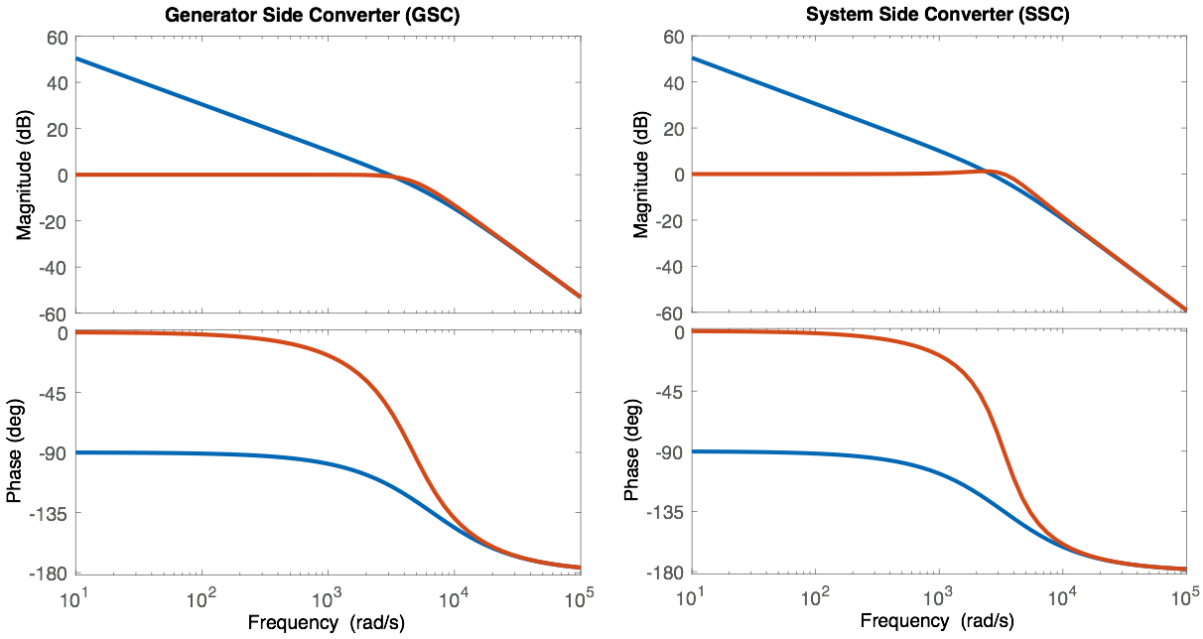

Figure B.1. Bode Plot of PMSG Inner Current Controller

Figure B.2 demonstrates the inner current controller response, and the ability to follow the references. The yellow and orange lines are currents i_d and i_q, while the blue and green lines give references $i_{d,ref}$ and $i_{q,ref}$. The simulations demonstrate the controller step response for a sudden large change in machine output. The oscillations seen in the current signals are caused by machine inertia. All currents respond quickly to the step change, with a low settling time of around 50ms. This seen together with the bode plot suggests the system is tuned well.

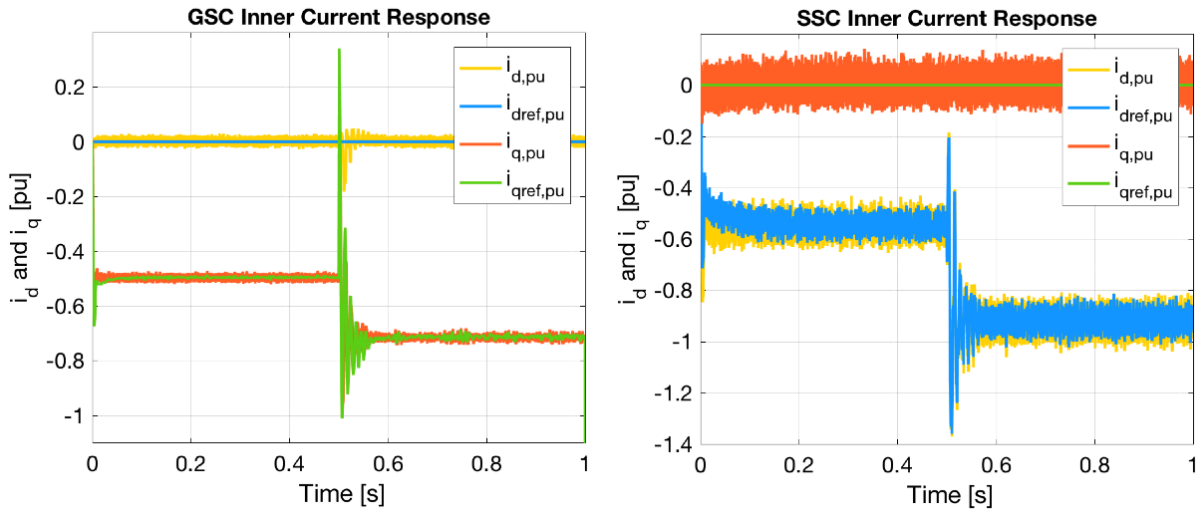

Figure B.2. Inner Current Controller Response

B.2. DC-VOLTAGE CONTROL TUNING (PMSG WIND SYSTEM)

The tuning of the DC-link voltage controller is based on the symmetrical optimum method as described in section A.2. The control parameters are given by the tuning criteria as:

$$T_{iv} = a^2 T_{eq} \tag{72}$$

$$K_{pv,pu} = \frac{V_{DC,pu}}{V_{d,pu}} \frac{1}{\omega_b C_{pu} a^2 T_{eq}} \tag{73}$$

The value of $\frac{V_{DC,pu}}{V_{d,pu}}$ is equal to 1pu for normal operation. Parameter T_{eq} is the equivalent time constant of the inner control loop, a is the degree of freedom in the controller equal to 3 and C_{pu} is the DC-link capacitor.

Applying the numerical values of the converter gives the control parameters of the DC-voltage controller as:

$$T_{iv} = 9 * 3 * 10^{-4} = 0.0027 \tag{74}$$

$$K_{pv,pu} = \frac{1}{(2\pi * 50) * 0.88 * \sqrt{6} * 3 * 10^{-4}} = 4.0191 \tag{75}$$

Figure B.3 gives the Bode plot of the open and closed loop transfer function of the outer DC-voltage controller. The open loop function is marked in blue and gives the phase and gain margins of the system. The controller has phase margin $PM = 53.13°$ and gain margin $GM = \infty$. This shows the system has a stable response, pointing to adequate tuning parameters.

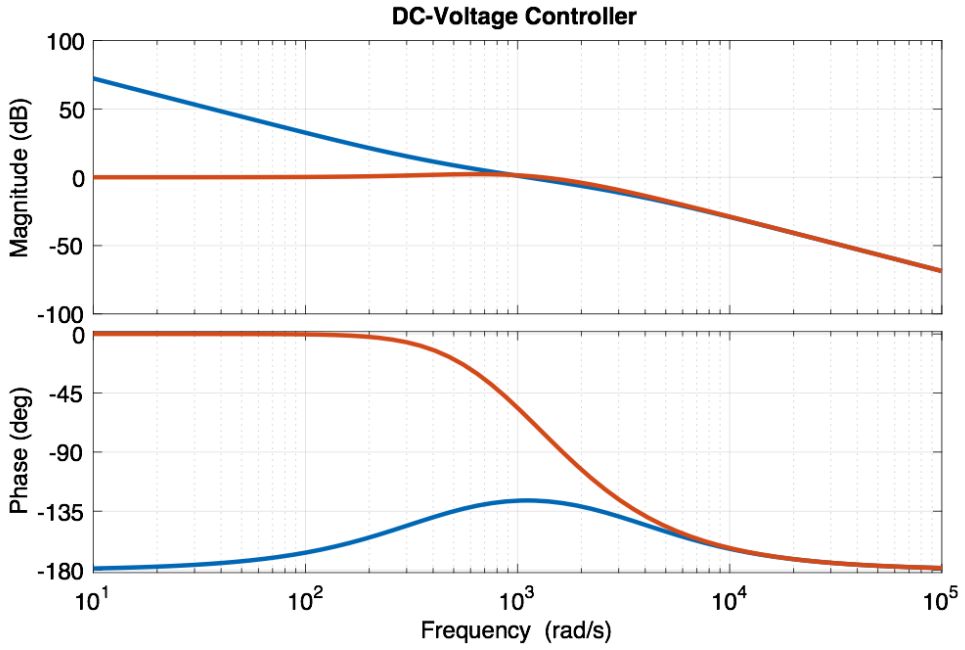

Figure B.3. Bode Plot of DC-Voltage Controller

Figure B.4 demonstrates the outer DC-voltage controller response, and the ability to follow the reference. The blue line is the voltage v_{DC}, while the yellow line gives reference $v_{DC,ref}$. The simulation demonstrates the controller step response for the sudden large change in machine output as for the current controller simulation of section B.1. The voltage experiences some oscillations right after the change in machine output, but settles quickly after around 40ms. This seen together with the bode plot suggests the controller is tuned well.

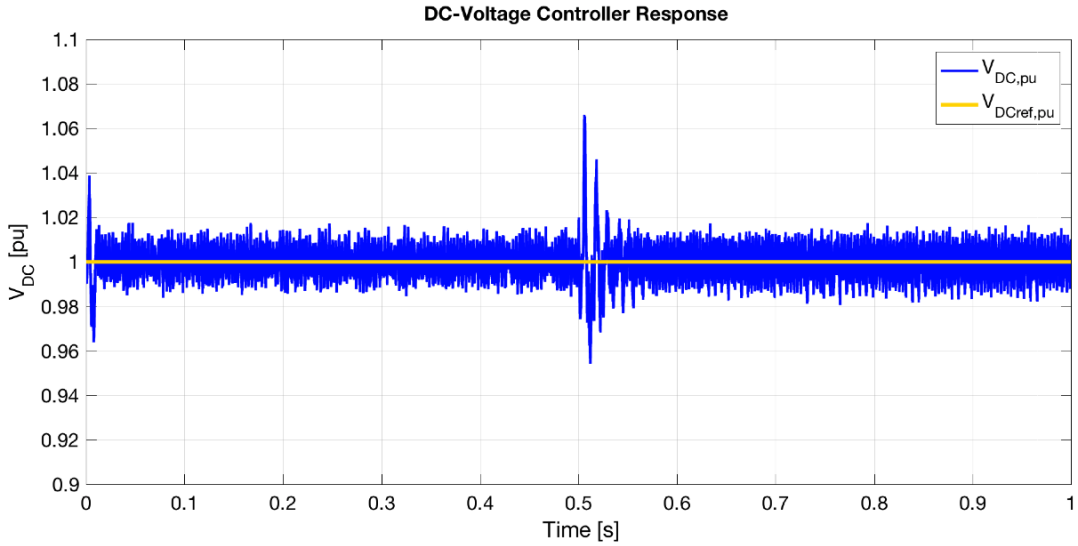

Figure B.4. DC-Voltage Controller Response

B.3. Speed Control (PMSG Wind System)

The tuning of the speed controller is based on the symmetrical optimum method as described in section A.2. The control parameters are given by the tuning criteria as:

$$T_{iw} = a^2 T_{eq} \tag{76}$$

$$K_{pw,pu} = \frac{1}{\omega_b 2 H_{pu} a^2 T_{eq}} \tag{77}$$

Parameter T_{eq} is the equivalent time constant of the inner control loop, a is the degree of freedom in the controller equal to 3 and H_{pu} is the inertia constant of the machine.

Applying the numerical values of the machine and converter give the control parameters of the speed controller as:

$$T_{iw} = 9 * 3 * 10^{-4} = 0.0027 \tag{78}$$

$$K_{pw,pu} = \frac{1}{(2\pi * 50) * 2 * 0.5505 * 9 * 3 * 10^{-4}} = 3.2120 \tag{79}$$

Figure B.5 gives the Bode plot of the open and closed loop transfer function of the outer speed controller. The open loop function is marked in blue and gives the phase and gain margins of the system. The controller has phase margin $PM = 53.13°$ and gain margin $GM = \infty$. This shows the system has a stable response, pointing to adequate tuning parameters.

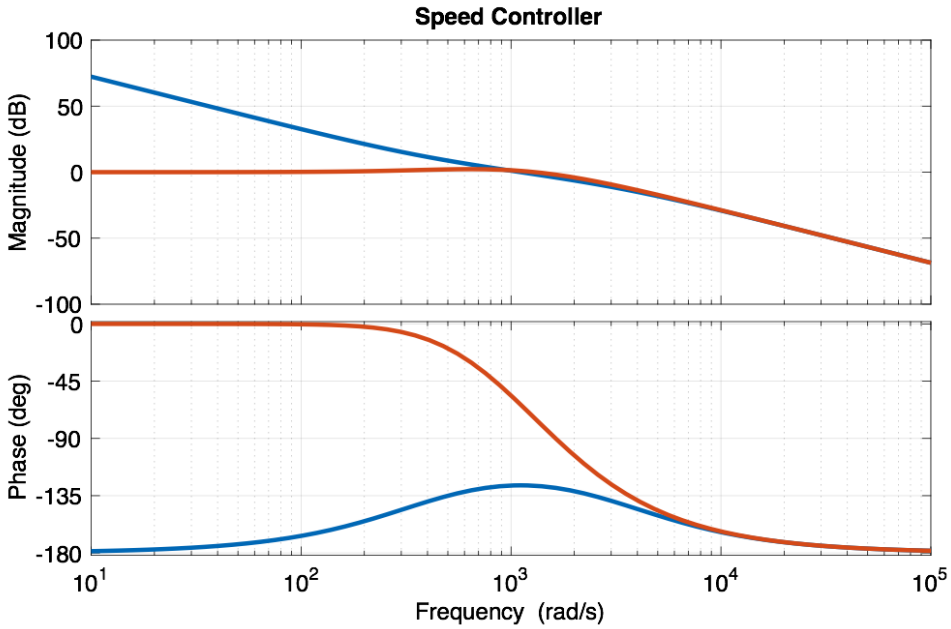

Figure B.5. Bode Plot of Speed Controller

Figure B.6 demonstrates the generator speed controller response, and the ability to follow the reference. The yellow line is the speed ω_m, while the blue line gives reference $\omega_{m,ref}$. The simulation demonstrates the controller step response for the sudden large change in machine output as for the current controller simulation of section B.1. The speed experiences some oscillations right after the change in machine output, but settles quickly after around 60ms. This seen together with the bode plot suggests the controller is tuned well.

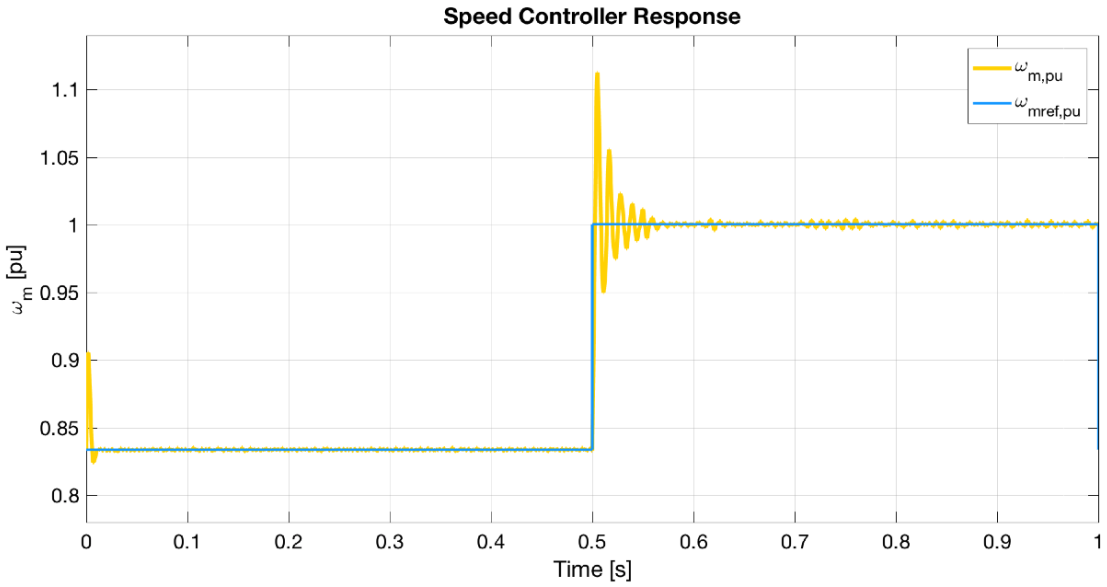

Figure B.6. Speed Controller Response

B.4. Blade Pitch Control (PMSG Wind System)

The tuning of the pitch controller is based on the comparison of multiple runs of the system with different parameter values. The starting point was chosen from [59], as $K_{pb} = 10$ and $T_{ib} = 2$, with both parameters individually varied. The simulation test case was performed as a large step-change in wind speed at time $t = 0.5s$ to evaluate the performance of the controller for different parameters. The results of the runs are summarized in the figures below.

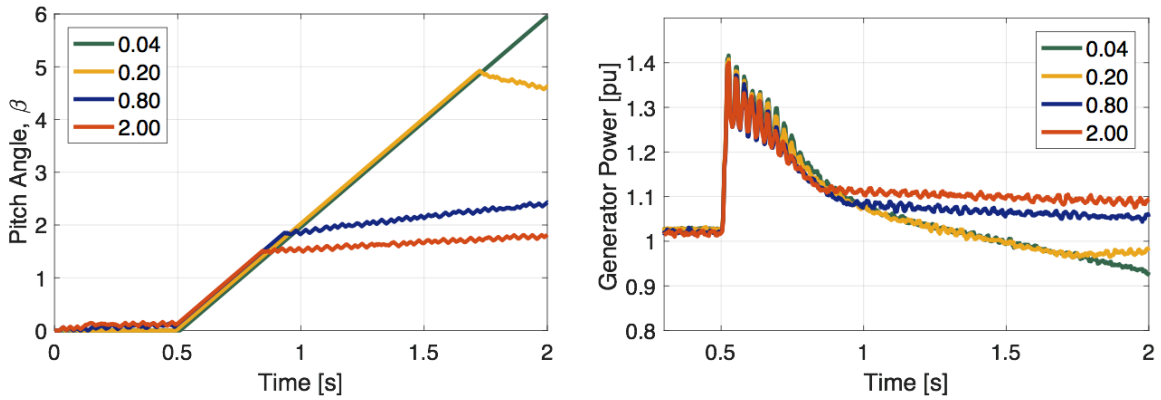

Figure B.7. Varying T_{ib} with K_{pb} = 10

Figure B.7 shows the simulation results for varying T_{ib} while keeping K_{pb} constant. A high time constant value seems to lower the sensitivity of the controller and yields a large offset in

power output. Similarly, a too small time constant seems overly sensitive and yields a large negative offset. The optimal value of time constant T_{ib} is therefore chosen as 0.2.

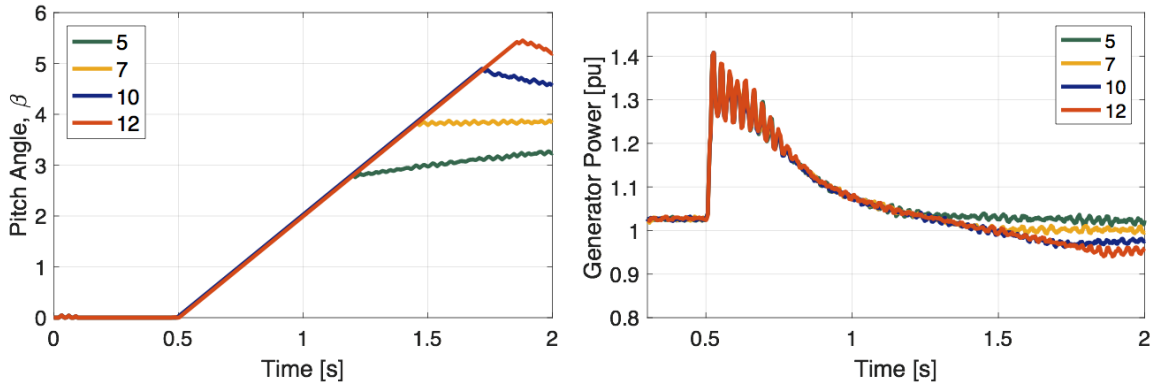

Figure B.8. Varying K_{pb} with T_{ib} = 0.2

Figure B.8 shows the simulation results for varying K_{pb} while keeping T_{ib} constant at optimal value, 0.2, found above. A high proportional gain seems to make the system overly sensitive, yielding a negative offset in power output. Similarly, a too low proportional gain seems not sensitive enough, yielding a positive offset in power output. The optimal value of proportional gain K_{pb} is therefore chosen as 7.

The final pitch angle controller parameters are therefore set as:

$$T_{ib} = 0.2 \tag{80}$$

$$K_{pb} = 7 \tag{81}$$

B.5. Speed Control (Induction Motor Drive)

The tuning of the induction motor drive speed controller is based on the pre-defined values found for the Simulink built-in direct torque control block [53]. The control parameters were slightly adjusted to better match the system parameters. The resulting values are given as:

$$K_{pwm,pu} = \frac{H_{im}}{a^2 T_{eq}} = 105.8 \tag{82}$$

$$T_{iw} = \frac{K_{pwm,pu}}{2000} = 0.0529 \tag{83}$$

Error! Reference source not found. demonstrates the fast response of the implemented speed controller. The controller is tested for various speed references, and is seen to work well also for zero crossings and negative speeds.

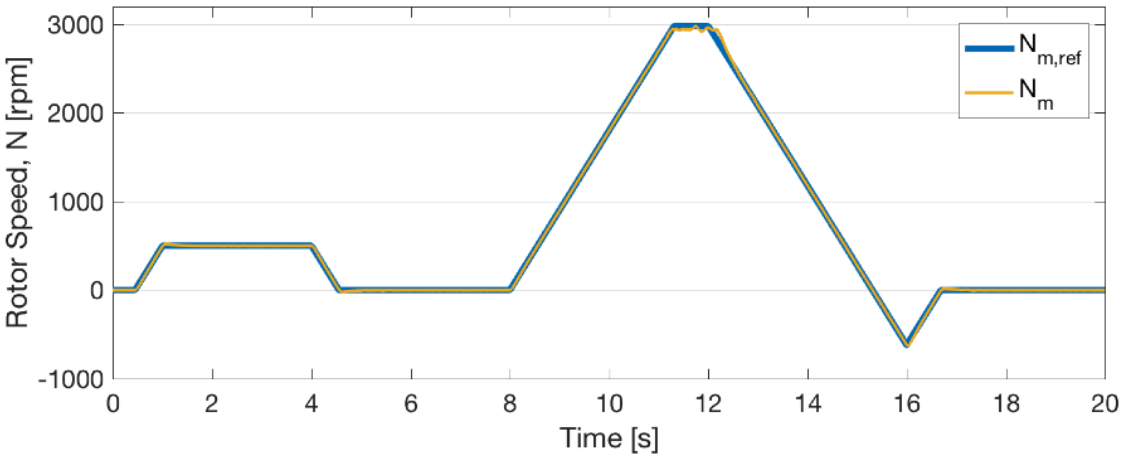

Figure B.9. Induction Motor Drive Speed Controller Response

C. MATLAB/SIMULINK MODEL

This appendix gives the simulation model implemented in Matlab/Simulink. The following figures are included to show the model:

- Figure C.1. Simulink Model of Complete Wind Integrated Oil & Gas Offshore Installation
- Figure C.2. Simulink Model of PMSG Wind Energy System
- Figure C.3. Simulink Model of Wind Turbine
- Figure C.4. Simulink Model of GSC
- Figure C.5. Simulink Model of SSC
- Figure C.6. Simulink Model of Gas Turbine Coupled with Synchronous Generator
- Figure C.7. Simulink Model of Gas Turbine
- Figure C.8. Simulink Model of Induction Motor Drive
- Figure C.9. Simulink Model of DTC
- Figure C.10. Simulink Model of Flux and Torque Estimator
- Figure C.11. Simulink Model of Power Line Model

C.1. COMPLETE WIND INTEGRATED OIL & GAS OFFSHORE INSTALLATION

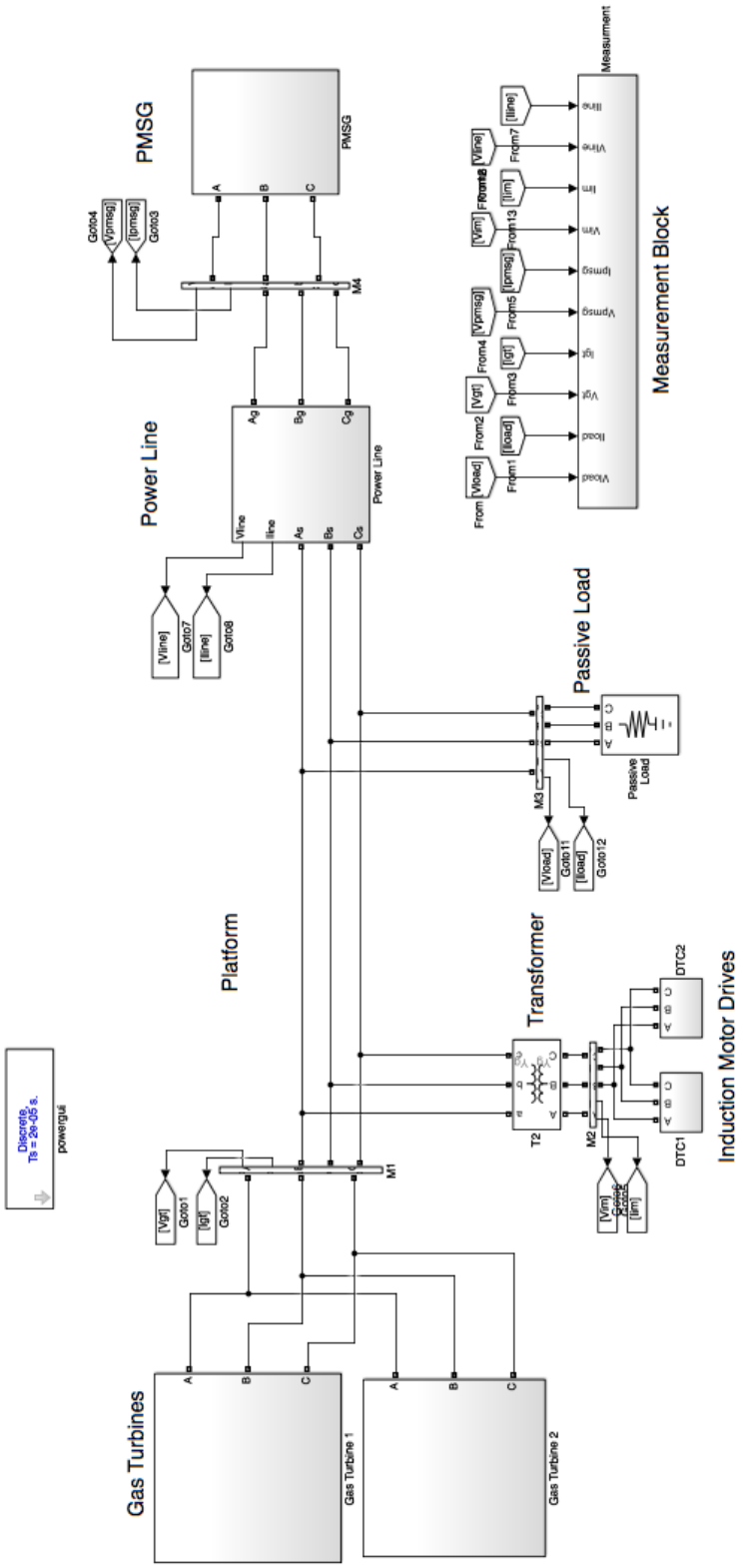

Figure C.1. Simulink Model of Complete Wind Integrated Oil & Gas Offshore Installation

C.2. PMSG WIND ENERGY SYSTEM

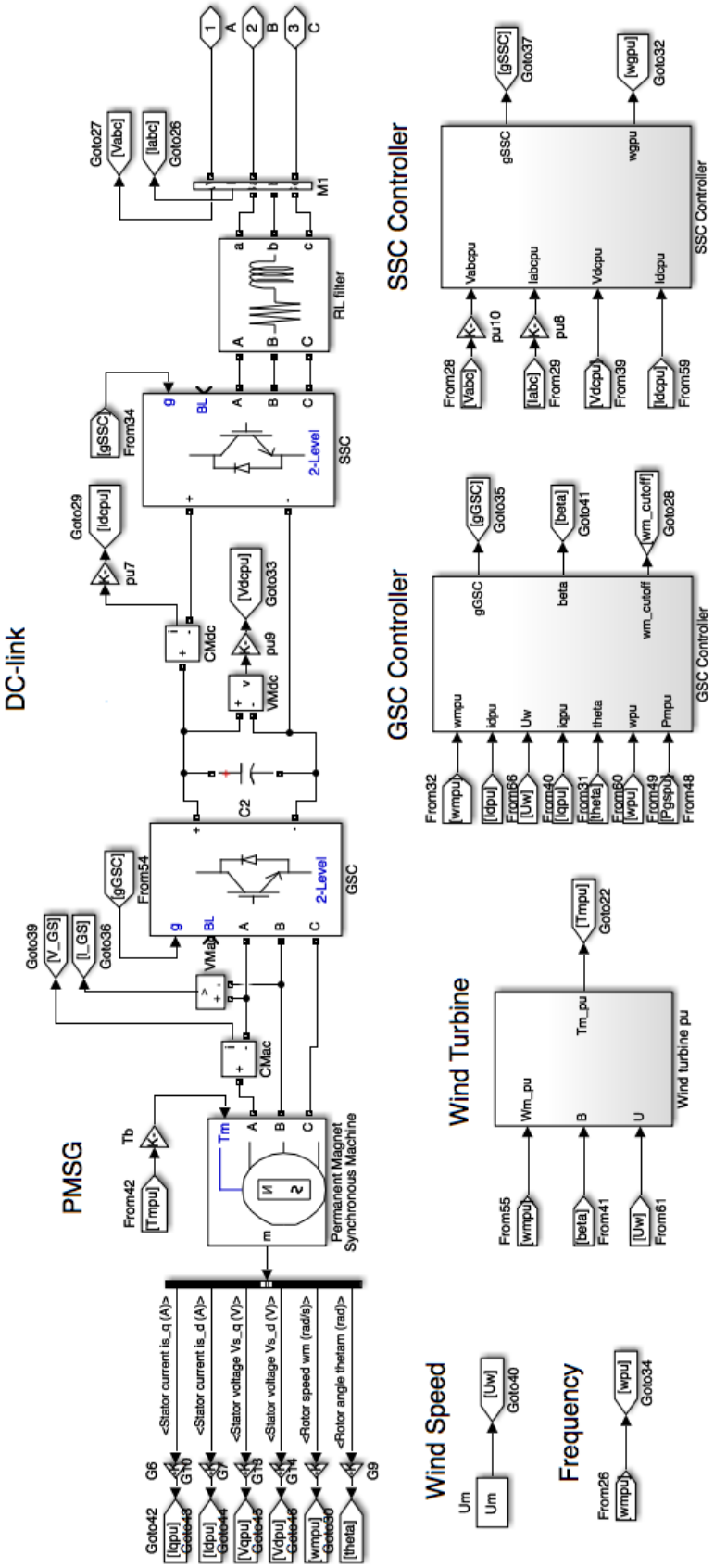

Figure C.2. Simulink Model of PMSG Wind Energy System

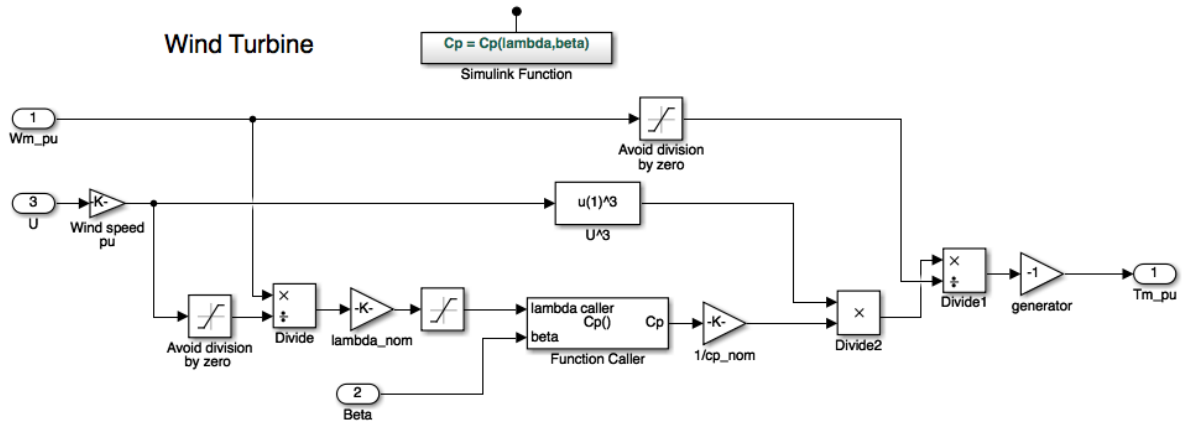

Figure C.3. Simulink Model of Wind Turbine

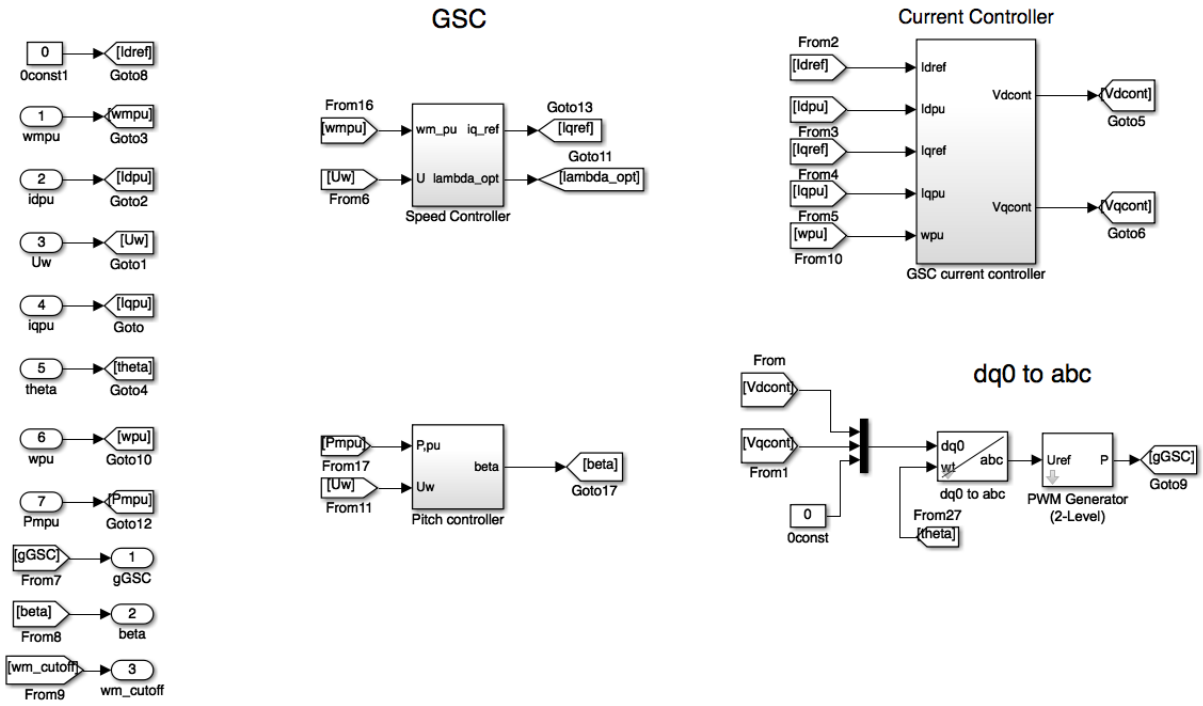

Figure C.4. Simulink Model of GSC

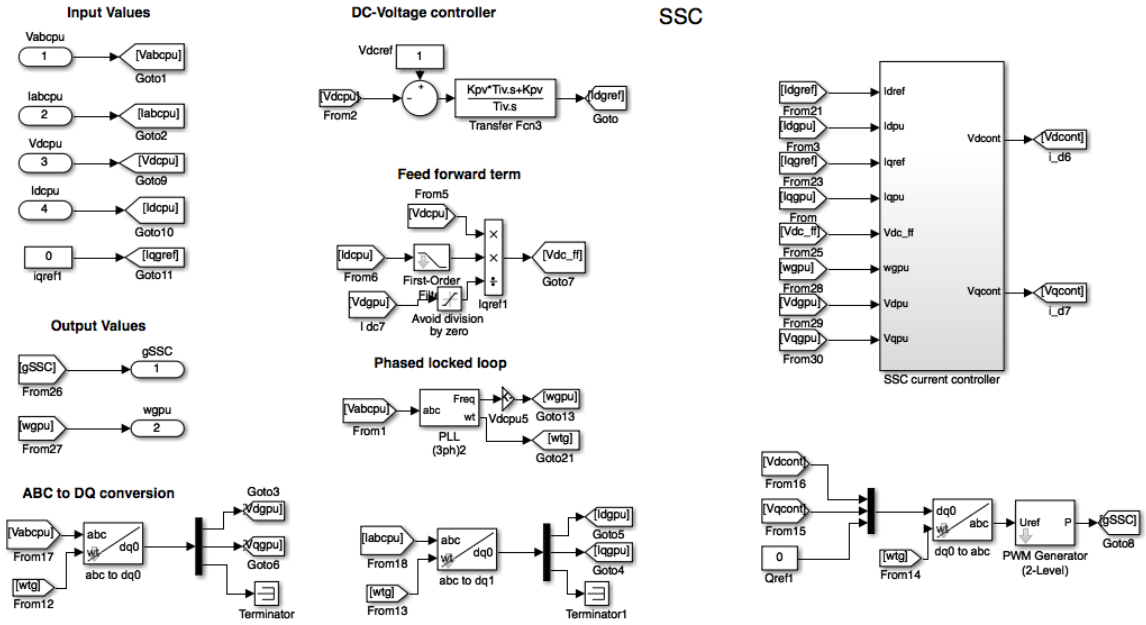

Figure C.5. Simulink Model of SSC

C.3. GAS TURBINE SYSTEM

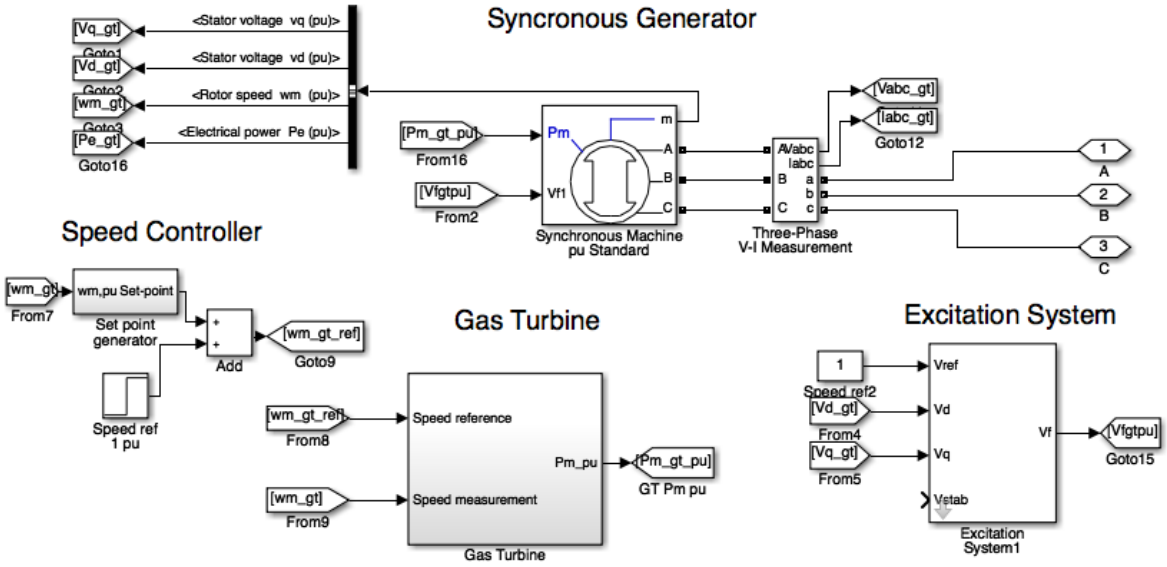

Figure C.6. Simulink Model of Gas Turbine Coupled with Synchronous Generator

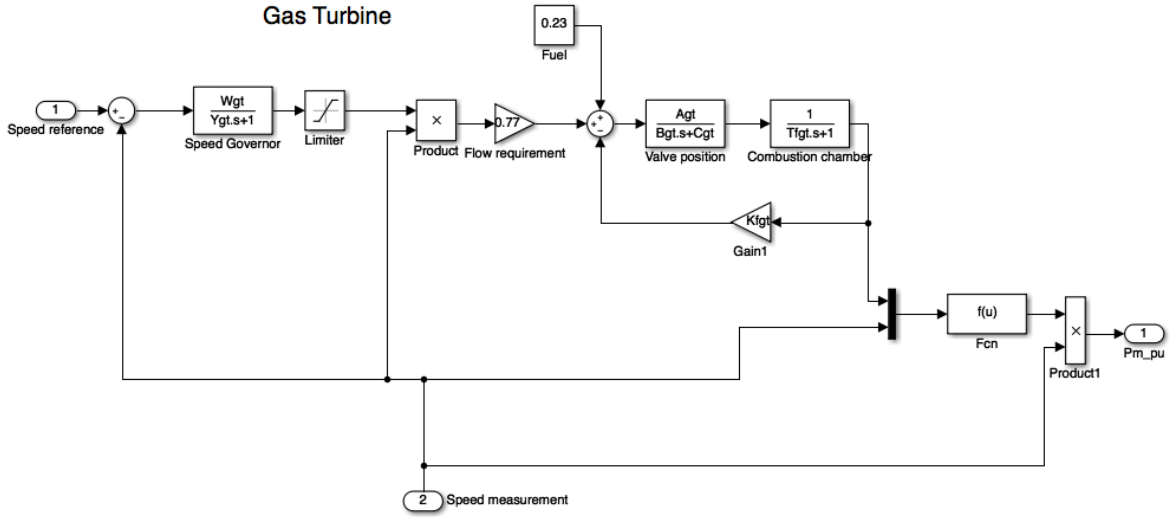

Figure C.7. Simulink Model of Gas Turbine

C.4. INDUCTION MOTOR DRIVE SYSTEM

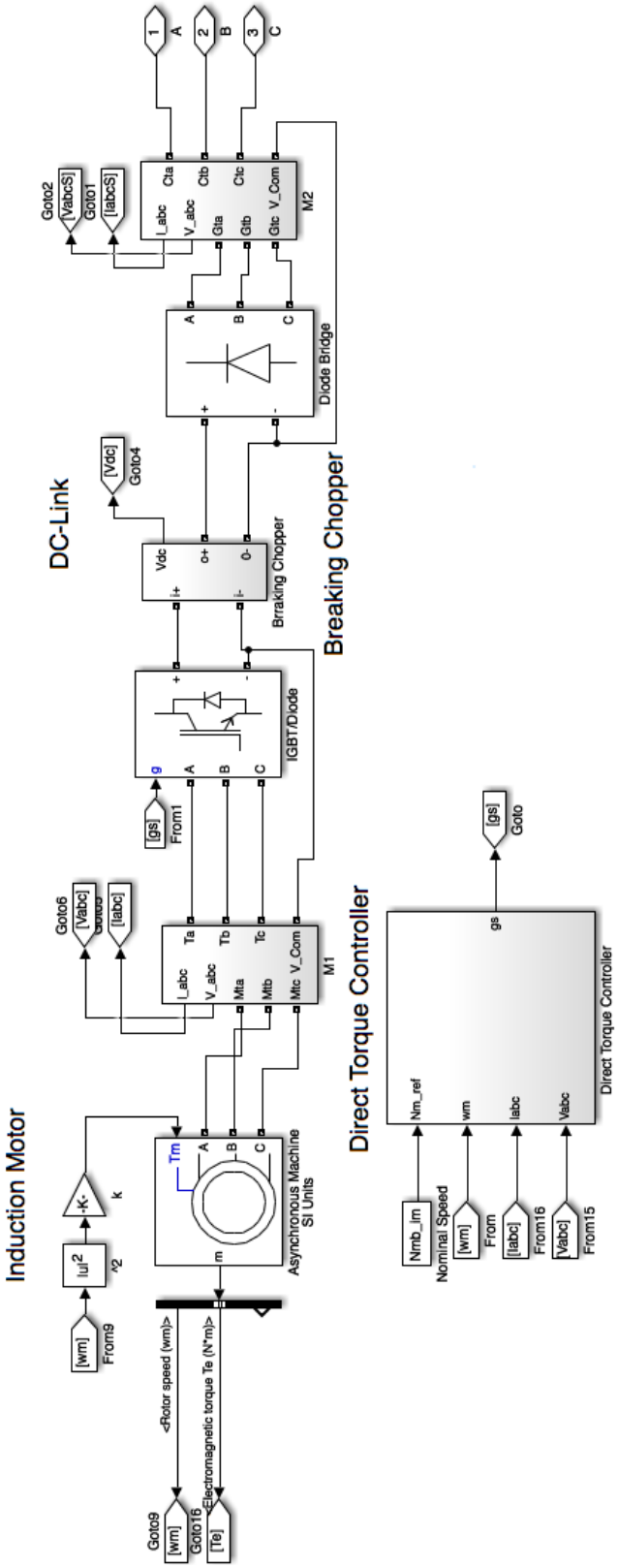

Figure C.8. Simulink Model of Induction Motor Drive

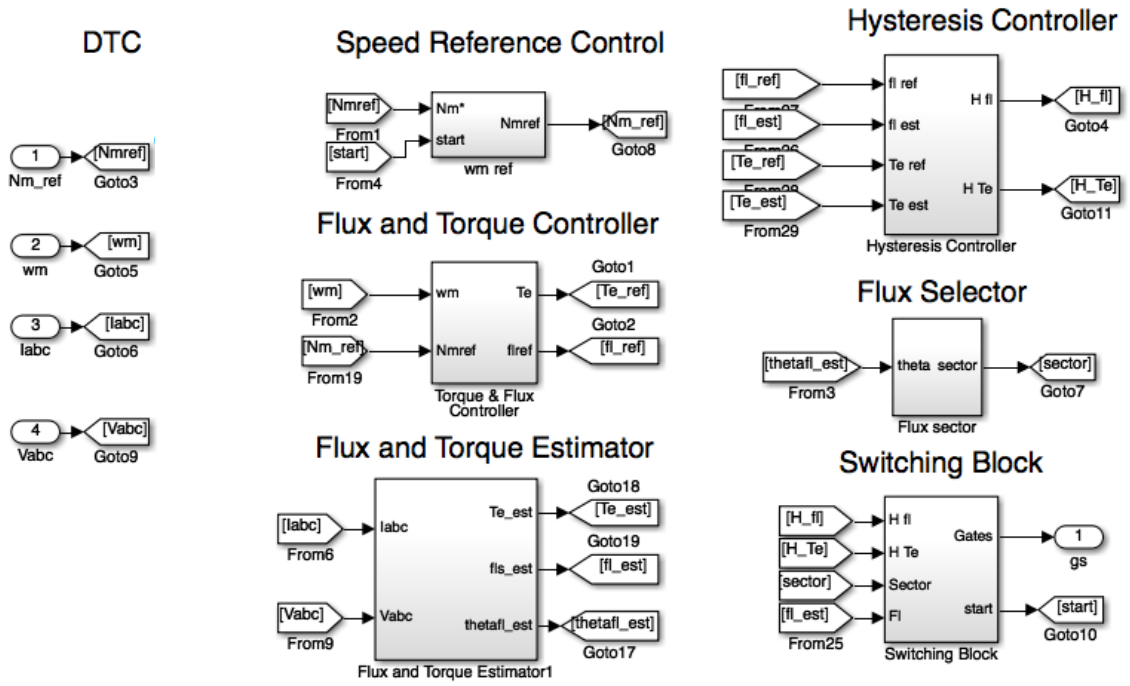

Figure C.9. Simulink Model of DTC

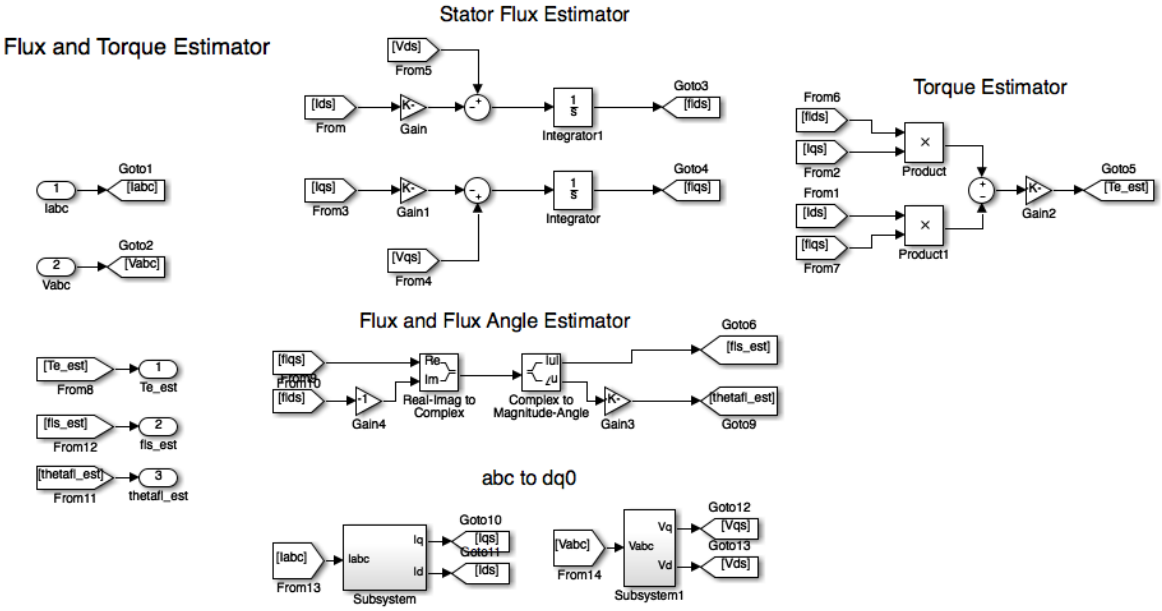

Figure C.10. Simulink Model of Flux and Torque Estimator

C.5. POWER LINE MODEL

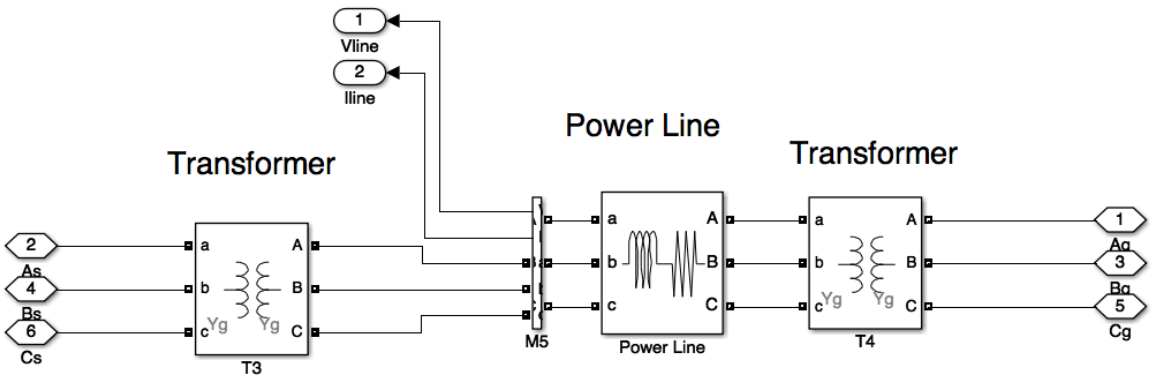

Figure C.11. Simulink Model of Power Line Model